Politecnico di Torino
Dipartimento Scienza Applicata e Tecnologia (DISAT)

Politecnico di Torino

DISAT (Department of Applied Science and Technology)

February 2015

PhD Thesis
in Material Science

Si-SiC based materials obtained by infiltration of silicon: study and applications

D’Amico Giuseppe Claudio

Mentors: Claudio Badini (Full Professor), Fino Paolo (Full Professor) and Biamino Sara (Associate Professor)

<u>Department of Applied Science and Technology</u>
Corso Duca degli Abruzzi 24, 10129 Torino, Italy

Dedications

At the end of my thesis work I want to thank my tutors for helping and supporting me during my research: Fino Paolo, Biamino Sara and Badini Claudio. I also want to thank the following professors for their availability: Pavese Matteo, Deorsola Fabio, Milanese Daniel and Ortona Alberto.

Thanks also goes to all the technicians who assisted me during these years: Fuso Laura, Leo Maurizio, Raimondo Mauro, Favero Antonio, Aghem Giuseppe and everyone I have forgotten.

Furthermore I would to thanks my former office-colleagues: Silvia, Monica, Cristina, Clara, Ehsan, Tiziana, Ratna and Marco.

In this experience I have worked alongside many group-colleagues, that I can list here like old colleagues (many of whom no longer work at the Polytechnic): Simona, Paolo E., Andrea A., Silvia, Emiliano, Dreidy, Wenshu, Xiang, Ramzan, Rao, Azhar, Simone, Lorenzo, Veronica, Mathieu, Andrea C. (the Master), Andrea R. and Eleonora; and new ones: Giorgio, Giulio, Alberta, Karol, Luca, Giovanna, Federico, Abdollah, Oxana and Andrea C. All of them, who more (the majority) who less, left me something.

A special thought goes to Elisa, my actual office-colleague and mate of this Ph.D.

Last, but not least, I wish to say a big thank you to my parents and to all my friends: each one of them knows why.

Table of contents

Preface

Many efforts and investments have been made in the last decades in order to obtain materials able to withstand extreme conditions in several technological fields such as future military, industrial and space based projects. The present PhD thesis addresses this problem dealing Ultra High Temperature Ceramics (UHTCs) and in particular focusing on Si-SiC-ZrB_2 composites obtained with a technique named silicon reactive infiltration (SRI).

Each major chapter of the present thesis relates to an article either published or in press on the journals indicated at the end in the seventh chapter (List of author's publications). The sequence of these chapters is obviously not random, but trying to follow the streamline that leads from the physico-chemical and technological properties of the material to its applications, in my case this is meant its use in industrial burners within an european project: CEREXPRO, that was financially supported by the European Commission in the FP7 (7th Framework Programme).

The reader is introduced to the current state of the art of UHTC (Chapter 1) having a historical review of UHTC research carried out thus far. Since the most comprehensive research has been focused on compositions containing HfB_2 or ZrB_2, they are the primary materials discussed. The chapter concludes by illustrating a particular type of UHTC: the siliconized silicon carbide (Si-SiC) and the infiltration method used to obtain it.

In the second chapter a methodology to produce Si-SiC-ZrB_2 bulk ceramics, taking advantage of the reactive infiltration technique, is proposed. Preforms with different contents of SiC and ZrB_2 were compacted with phenolic resin, pyrolysed and finally infiltrated with molten silicon at temperature above its melting point.

A detailed study of the mutual interactions between the Si-SiC-ZrB_2 constituent materials during their processing and of their chemical activity with oxygen at high temperatures in the prospect of using this material as a matrix of a continuous fiber reinforced composite is addressed in Chapter 3. The study of the early stage of oxidation is the first part of this chapter, while the second part is focused on the long-term oxidation of some selected samples at a high temperature.

The aim of chapter four is to give an overview of the processing routes currently available for the preparation of macro-porous ceramics, with particular emphasis on the processing–microstructure–property relations inherent to each process. At the end, the chapter presents several high temperature applications in which Si-SiC foams are currently applied because of their superior thermo-mechanical properties. The Chapter 5, in fact, aims to track the changes of Si-SiC foam properties during the first part of a long time aging condition, typical of industrial burner applications.

The project “CEREXPRO” (CERamic heat EXchangers with enhanced materials PROperties), discussed in the Chapter 6, was aimed to develop a new generation of ceramic heat exchangers for high temperature heat recovery with the target of significantly reducing the size and weight as well as also the price of such components by simplifying the manufacturing process and allowing a higher flexibility in the heat exchanger geometry. The use of precursors/template materials taken from the textile industries and a subsequent ceramic conversion, via liquid silicon infiltration, is proposed as the main technological path for reaching the above objectives. The main role of the Polytechnic within this project was the characterization process of materials.

I hope you will enjoy reading this work. Please contact me for any inquiry at giuseppe.damico@polito.it.

Torino, November 2014.

Giuseppe Claudio D’Amico

D'Amico Giuseppe Claudio

1. UHTCs (Ultra High Temperature Ceramics)

1.1 Introduction

Refractory compounds such as ceramic carbides, borides and nitrides are characterized by high melting points, high hardness and good chemical inertness and oxidation resistance [1-3]. These refractory compounds have been broadly termed Ultra High Temperature Ceramics (UHTCs). Strong covalent bonding is responsible for the high melting points, moduli and hardness of the UHTC family of materials [4, 5]. High negative free energies of formation also give UHTCs excellent chemical and thermal stability under many conditions [4, 5].

The bibliographical search with the use of the SciFinder (CAS) system based on keywords that characterize this field of research made it possible to obtain a distribution of the frequency of references to different chemical compounds (Fig. 1.1). As can be seen, the most frequently mentioned compounds are ZrB_2 and HfB_2, as well as SiC, which are the basic components of ultra-high-temperature ceramics (UHTCs).

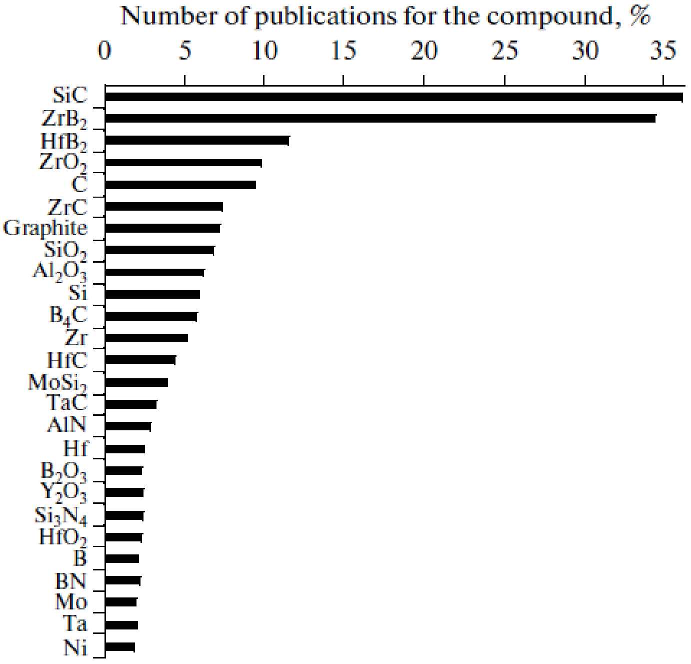

Figure 1.1: Distribution (%) of the publications concerning the ultra-high temperature materials indexed over the compounds indicated (according to the data of SciFinder, CAS) [6].

Development of non-oxide ceramics has lagged behind that of oxides because they are rarely found in nature, need to be processed in controlled reducing atmospheres and tend to oxidize in air even at room temperature, especially when in fine powder form.

While UHTC compounds have been studied for over 100 years [7], historically, this family of ceramic materials was first significant processing-structure-property investigated between the 1950s and 1970s by Russian and U.S. laboratories [2, 8, 9]. At present, most of the structural materials for use in high temperature oxidizing environments are limited to SiC and Si_3N_4 based materials, oxide ceramics and C/C composites with thermal protection. Silicon-based ceramics and protected C/C composites exhibit good oxidation resistance, but only up to ~ 1600°C, and their thermal cycling lifetimes are modest. The development of structural materials for use in oxidizing and rapid heating environments at temperatures above 1600°C is therefore of great importance for engineering.

Some of the earliest and most thorough work was performed in the 1960's by ManLabs under a research program funded by the Air Force Materials Laboratory (AFML) [1, 2]. Work on these materials was initiated to meet the need for high temperature materials that would enable the development of maneuverable hypersonic flight vehicles with sharp leading edges [2]. Around the same time NASA was also investigating high temperature materials to meet its own needs [3].

At present, many groups in the U.S., Japan, China, India and in Europe (especially in Italy) are studying UHTC systems to improve resistance to oxidation [10-13].

The need for high temperature materials that can operate with no or limited oxidation or ablation at temperatures greater than 3000K has driven the development of UHTC materials. The potential applications for UHTCs span a wide number of needs arising from future military, industrial and space based projects. Potential industrial applications for UHTCs include use in foundry or refractory processing of materials. Their chemical inertness makes them ideal for molten metal crucibles, thermo-well tubes for steel refining, cutting tools, furnace elements and as parts for electrical devices such as heaters and igniters [14-20].

The military and aerospace applications for UHTCs range from rocket nozzle inserts and air augmented propulsion system components to leading edges and nose caps for future hypersonic reentry vehicles [14, 21-23]. Early space vehicle designs, such as the space shuttle, were designed with a large radius, blunt body design to reduce aero thermodynamic heating to maintain moderate temperature limits on all parts of the vehicle. However, the larger the leading edge radii, higher the vehicles drag, which reduces maneuverability and cross range during reentry. Increased maneuverability requires laminar flow across the control surfaces, which, in turn, necessitates the use of sharp leading edges; therefore, to improve performance, hypervelocity vehicle concepts have proposed using slender aerodynamic shapes with sharp leading edges [24, 25]. Development of sharp body vehicles increases the lift-to-drag ratio thereby improving the vehicles' reentry cross range. A higher lift to drag ratio also has the potential to improve the overall vehicle system safety in a number of ways. However, the temperature of the leading edge is inversely proportional to the square root of the leading edge radius, i.e. as the leading edge radius decreases the temperature increases [25]. Therefore the successful design of a sharp hypersonic vehicle requires the development of new materials with higher temperature capabilities than the current state-of-the-art materials can provide. Ultra High Temperature Ceramics are a family of materials that are promising candidates for meeting such requirements [24, 25].

In comparison to carbides and nitrides, the diborides tend to have higher thermal conductivity, which gives them good thermal shock resistance and makes them ideal for many high temperature thermal applications [5, 26]. The relatively good oxidation resistance of refractory diboride compounds, compared to other refractory intermetallic compounds (i.e. carbides, nitrides and silicides), has focused many research efforts into detailed investigations of transition metal diborides of groups IV and V (Ti, Zr, Hf, Nb, Ta). Of the transition metal diborides, hafnium diboride (HfB_2) and zirconium diboride (ZrB_2) were identified as the most promising candidates for high temperature applications.

In particular, ZrB_2 has the lowest theoretical density among the ultra-high temperature ceramics, which makes it an attractive material for aerospace applications [21, 27, 28]. However, the use of the single-phase material for high-temperature structural applications is limited by its poor oxidation and ablation resistance, as well as its poor damage tolerance.

The composite approach has been successfully adopted in order to improve the densification, mechanical properties, physical properties, as well as the oxidation and ablation resistance of the ZrB_2 ceramics [29-40]. Obviously, the mechanical and physical properties of the ZrB_2-based composites are closely linked with the densification process, compositions, starting powder, microstructure and intergranular second phase.

Of large importance is also the fact that upon the oxidation of ZrB_2 and HfB_2 there arise, apart from products that are liquid at temperatures higher than 800÷1200°C (forming borosilicate glass, which impedes rapid diffusion of oxygen into the bulk of the material), also refractory oxides (T_m ~ 2700°C for ZrO_2 [6], 2800÷2850°C for HfO_2 [6]) possessing a low vapor pressure (MO (g) at T = 2160°C is ~ $2.88*10^{-7}$ atm for ZrO_2; ~ $1.15*10^{-7}$ atm for HfO_2 [6]) and a sufficiently high (for the expected operating conditions) mechanical strength; this must ensure a maximally possible retention of the geometry of an article, which influences its aerodynamic characteristics.

In the field of designing UHT materials, two directions, which are substantially different in, first of all, the priority purposes, can be distinguished. The first of these is connected with the modification of classical UHT materials (C_f/C and C_f/SiC composites) by refractory compounds, such as ceramic matrices and/or protective (antioxidant) coatings, with the purpose to significantly increase their oxidation resistance without a significant loss of the excellent thermo-mechanical characteristics of the base materials [6]. An alternative direction is the creation of purely ceramic almost poreless materials (possibly, with a certain their strengthening by the introduction of nanostructured components [6] or of short fibers [6]) on the basis of substances with a high thermal conductivity. This will allow an efficient heat removal from the regions adjacent to the points or lines of the total flow stagnation, which will work as separate segments of a complex composite detail (Fig. 1.2) [6], whose different parts will bear different types of load-thermal, oxidation, shock, shear, etc. An additional argument in favor of the selection of the design of the thermo-loaded parts of the flight vehicles in the form of an assembly of several segments is that the UHTCs are brittle ceramic materials (the probability of their destruction can be described in terms of the Weibull statistics); therefore, from the viewpoint of repairability, and also to make the manufacturing easier, structures that have a limited size or volume of components (like tiles or segments rather than a one-piece continuous edge) are preferable and, thus, have a reduced probability of the appearance of defects, which can decrease the strength.

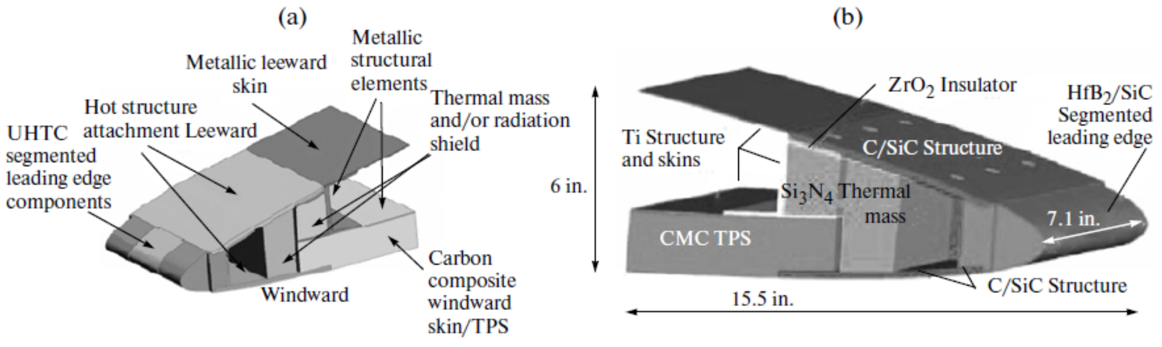

Figure 1.2: Construction of the leading edge of a wing prepared from a UHTC [6].

As a matter of fact, the best way to use monolithic UHTC materials for manufacturing sharp components seems to be to combine these materials with others (CMC notably). Thus, the UHTC part would be placed as an insert in front of the structural component in order to use only UHTC pieces of limited size. This allows for optimization of the element involved (performance, weight and cost in particular). However, it is important to note that the attachment design needs to be properly addressed to minimize thermal stresses. For example, it would be possible to avoid the contact of the UHTC element with cooler sub-components in the structure in order to reduce bearing stresses at the attachment location.

Clearly, the potential applications for UHTCs span a wider number of needs arising from future military, industrial and space based projects. While continued work has provided valuable insight on the performance of UHTCs consistent ongoing research efforts are required if future applications are to be realized.

Realization of the full potential of UHTCs as future high temperature materials requires a thorough knowledge of their properties and behavior under diverse conditions of temperature, environment and stress states [5]. The primary purpose of this chapter is to provide a historical review of UHTC research carried out thus far and, where available, to provide engineering data on UHTCs. Since the most comprehensive research has been focused on compositions containing HfB_2 or ZrB_2, they will be the primary materials discussed. Results from materials containing HfB_2 or ZrB_2 as the principal component with selected additives designed to enhance one or more of the following: oxidation resistance, mechanical properties and thermal stress resistance will also be presented. When available, data on other UHTC compositions will also be discussed. The chapter concludes by illustrating a particular type of UHTC: the siliconized silicon carbide (Si-SiC) and the infiltration method used to obtain it.

1.2 Bonding and structure of UHTCs

Ceramic borides, carbides and nitrides all have very strong chemical bonds that give them high temperature structural stability [5, 41-43]. As a result of the extremely strong bond between carbon atoms, carbides follow the classical definition of a brittle ceramic. They come in three general classes: ionic, covalent and interstitial. None of the ionic carbides have engineering uses because of their extreme brittleness [41]. The two covalent carbides of major importance, SiC and B_4C, both are valuable for their extreme hardness as well as excellent thermal and chemical stability. The largest class of carbides, those of the interstitial type, includes carbides of the metals Hf, Zr, Ti and Ta. These materials benefit from strong carbon networks and have some of the highest melting points of known materials. They are also known to have high strengths at elevated temperatures [41, 42]. From this standpoint, carbides offer a tremendous benefit in many engineering applications. Unfortunately, these materials are hard to fabricate because of their refractoriness, and little has been achieved beyond the laboratory scale [41, 42].

Ceramic nitrides have many of the same properties as carbides and nitrides are also difficult to fabricate, especially in the pure form, due to strong covalent bonding. Silicon nitride and boron nitride are the primary materials in the family of nitrides to be developed for engineering applications [43].

Then there are the ceramic borides, such as HfB_2 and ZrB_2. These materials also benefit from very strong bonding between boron atoms, although their bonding is not typically as strong as seen in the carbides thus these materials often have melting points below that of the carbides [5, 41]. A unique feature of the electronic nature of the boron bonding in these materials results in the borides having high thermal and electrical conductivities, higher than typically found in carbides and nitrides, as well as low coefficients of thermal expansion which combined gives the borides relatively good thermal shock resistance, for ceramics [5].

Table 1.I lists a number of metallic elements that form binary diboride compounds, with the AlB_2-type structure, shown in figure 1.3 [44, 45]. The AlB_2 structure contains graphite-like layers of boron separated by hexagonal close-packed (h.c.p.) layers of metal atoms. The diborides are comprised of rigid covalent boron lattices, such that the boron atoms have a trigonal prismatic metal environment with three close boron neighbors. The metal atoms coordinate twelve boron atoms, six metallic atoms in the same layer and two metal atoms in the two adjacent layers (top and bottom) [44, 45]. The boron nets have very strong covalent bonds that hinder an increase in the a_o direction, though no such hindrance occurs in the c_o direction, giving borides the ability to accommodate a wide variety of metals [44].

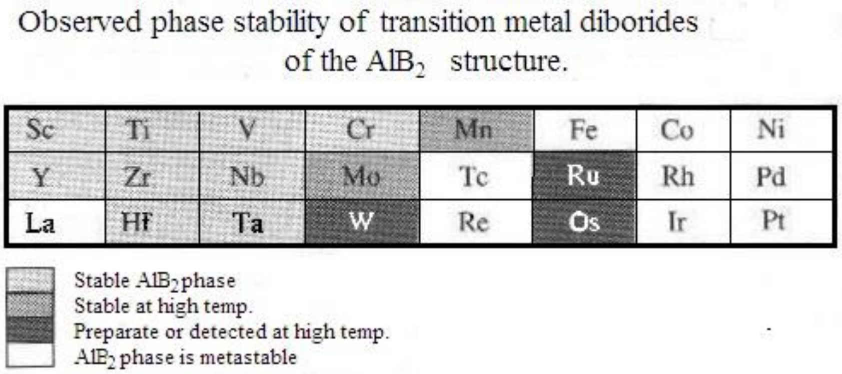

Observed phase stability of transition metal diborides
of the AlB_2 structure.

Sc	Ti	V	Cr	Mn	Fe	Co	Ni
Y	Zr	Nb	Mo	Tc	Ru	Rh	Pd
La	Hf	Ta	W	Re	Os	Ir	Pt

Stable AlB_2 phase
Stable at high temp.
Preparate or detected at high temp.
AlB_2 phase is metastable

Table 1.I: UHTCs metallic elements [46].

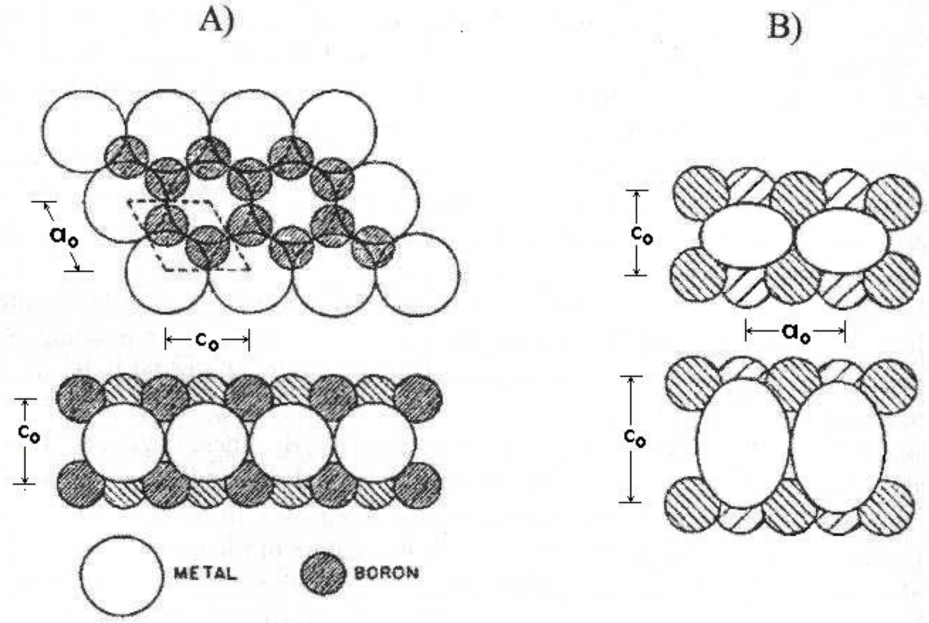

Figure 1.3: A) Atomic projections of the AlB_2-type structure showing top down and side view. B) An illustration of metal atom deformation within the AlB_2-type structure [44].

Spear calculated three chemical bonding parameters for borides of the AlB_2-type, plotted in figure 1.4 [44]. The parameter in the top graph is the ratio of the two elliptic axes of the metal atom and provides a measure of the amount of metal atom distortion. The middle parameter is a ratio of the volume of the elemental metal atom to the metal atom in the diboride. Ratios less than unity indicate the metal is too small for the space, while ratios greater than one indicate the metal atom is compressed in the structure. Ratios different from unity suggest M-M and possibly M-B bonds will have less than optimum strength. Finally, the parameter on the bottom is a measure of B-B bond strength; it is a ratio of the average minimum free boron radius to that of boron in the diboride. Smaller values are a result of stretched bonds and smaller bond energies [44]. From these calculations, Spear deduced that M-B bonding is likely the leading contributor to the structural integrity of AlB_2 type borides, more so than M-M or B-B bonding. Typically, the less distortion there is to the unit cell the stronger are the bonds that hold it together. As the degree of bonding increases so does the melting point, modulus and hardness, in the diborides as well as for carbide and nitride ceramics [5, 26, 41].

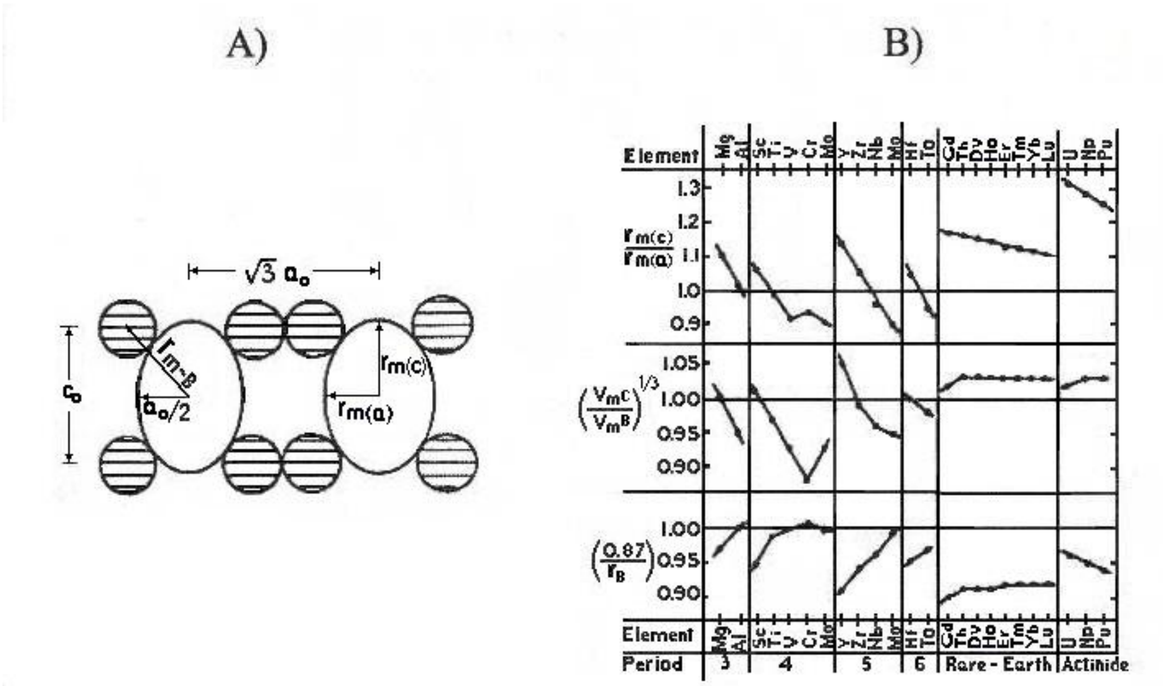

Figure 1.4: A) View of the (110) plane in a diboride structure, illustrating the geometrical crystal parameters as calculated by Spear. B) Table of bonding parameters as calculated from geometrical parameters in A), metals are grouped according to their period in the periodic chart [44].

Enthalpies of formation for several boride systems were reported by Samsonov and Vinitiskii [47]. From those results it is clear that the stability of diborides decrease in the order HfB_2 > TiB_2 > ZrB_2 >> TaB_2 > NbB_2 >VB_2, with VB_2 the least stable of the diborides, having the lowest energy of formation. To understand this trend, Guillermet and Grimvall showed that the cohesive properties of these materials could be described by the filling of electron bands, as shown by a plot of density of electron states (bonding or anti-bonding states), N(E), versus the respective energy of the system, figure 1.5 [48]. Using ZrB_2 as an example, the peaks P_1 and P_2 arise from 2s and 2p electron orbital hybridization with zirconium d orbital electrons. The peaks P_3 and P_4 represent bonding and then anti-bonding states between boron 2p and zirconium 4d electrons [5].

Hybridization thus reduces the strength of B-B bonds but creates strong M-B bonds as predicted by Spear in his analysis. Because the Fermi level, E_F: (energy level of the highest filled band at 0K) for ZrB_2 falls between the bonding and anti-bonding peaks, it can be seen that any increase in electron density would reduce bond strength by further filling of the anti-bonding states; similarly, any reduction in electron density lowers the number of electrons filling the bonding levels, also reducing bond strength. With those results in mind, the trend in boride stability is clearly shown when looking at a plot of standard entropy, E_S, vs. number of electrons per unit cell, n_e, see figure 1.6(left) [48]. A plot of E_S vs. T_f, melting temperature (Fig. 1.6(right)) shows the same trends as those illustrated in the plot of E_S vs. n_e [48]. Those materials, with their standard entropy or cohesive energy at a maximum, show the highest stabilities and melting points. Simply put, the materials with a Fermi energy between P_3 and P_4 have the highest stabilities. Listed in in order of bond strength, those species are materials formed with Ti, Zr and Hf. As the number of electrons, n_e, increases (i.e. V, Nb, Ta) more anti-bonding states are filled which decreases the bond strength and the melting temperature of the compound. Similarly, as n_e decreases (i.e. Sc, Y), fewer electrons are available to fill the bonding levels and compound stability decreases, also demonstrated by a reduction of the melting temperature, as shown in figure 1.6(right) [48].

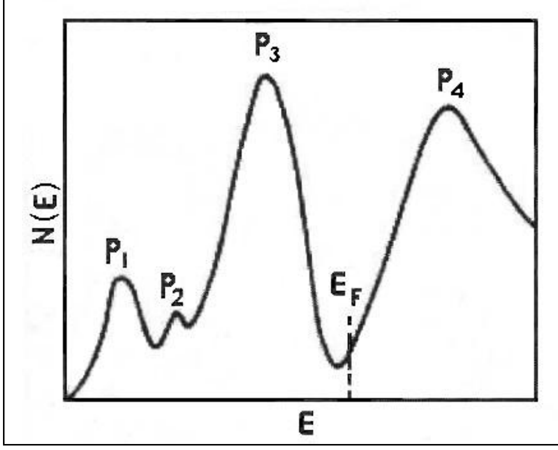

Figure 1.5: Plot of the general features of the electronic density of the states, N(E) number of electrons in that state (bonding or anti-bonding) versus energy of the system, for an AlB_2-type compound [48].

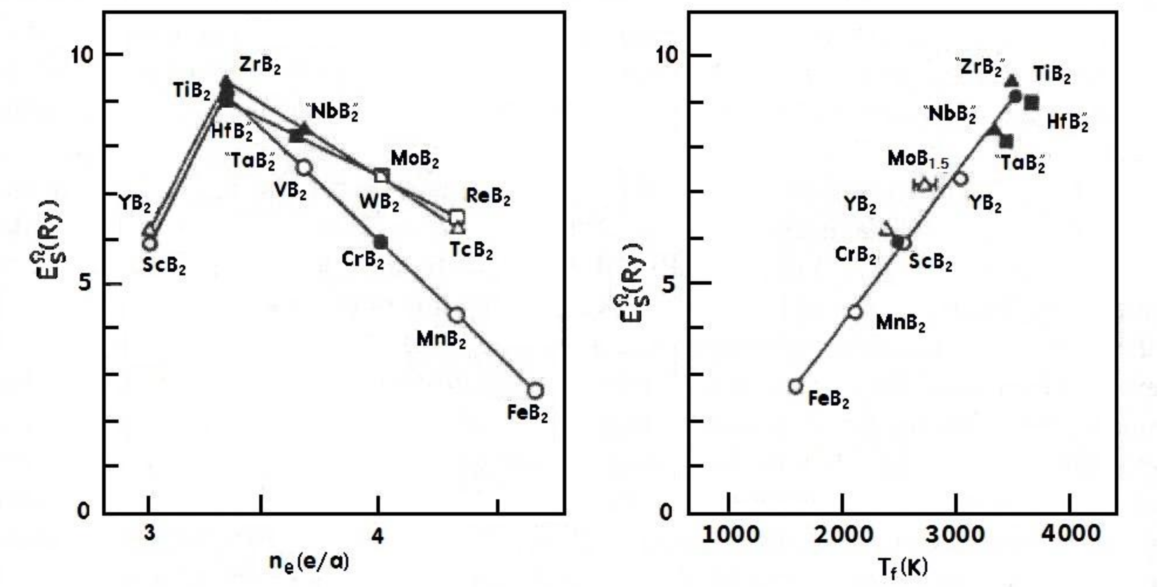

Figure 1.6: Left, plot of characteristic energy, defined from entropy related Debye temperature and plotted vs. the average number of valence electrons. Right, characteristic energy plotted vs. melting temperature [48].

Following the previous description of the atomic structure of boride, carbide and nitride ceramics, table 1.II lists physical crystalline structural differences of a variety of UHTCs along with respective density and melting point [46]. Note that density increases with increasing mass of the metal atom. Note also the differences in melting points between materials whereby the carbides typically have the highest melting points, above borides or nitrides of the same metal constituent.

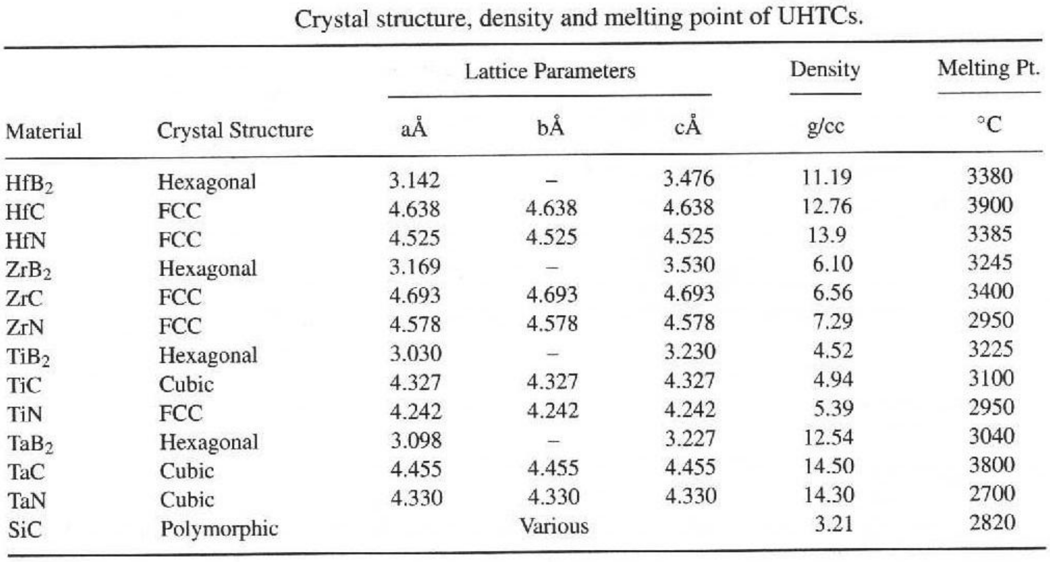

Crystal structure, density and melting point of UHTCs.

		Lattice Parameters			Density	Melting Pt.
Material	Crystal Structure	aÅ	bÅ	cÅ	g/cc	°C
HfB_2	Hexagonal	3.142	–	3.476	11.19	3380
HfC	FCC	4.638	4.638	4.638	12.76	3900
HfN	FCC	4.525	4.525	4.525	13.9	3385
ZrB_2	Hexagonal	3.169	–	3.530	6.10	3245
ZrC	FCC	4.693	4.693	4.693	6.56	3400
ZrN	FCC	4.578	4.578	4.578	7.29	2950
TiB_2	Hexagonal	3.030	–	3.230	4.52	3225
TiC	Cubic	4.327	4.327	4.327	4.94	3100
TiN	FCC	4.242	4.242	4.242	5.39	2950
TaB_2	Hexagonal	3.098	–	3.227	12.54	3040
TaC	Cubic	4.455	4.455	4.455	14.50	3800
TaN	Cubic	4.330	4.330	4.330	14.30	2700
SiC	Polymorphic		Various		3.21	2820

Table 1.II [46].

Some of the thermodynamic properties for a few diborides, including HfB_2 and ZrB_2 are listed in tables 1.III and 1.IV. The data in these tables are from Pankratz et al. who reviewed available data in the early 80's and included only the data they deemed to be reliable [49]. Enthalpies of formation are strongly correlated with Gibbs free energies of formation for borides, because the entropy terms are small. This also means that the free energy is relatively insensitive to temperature [5].

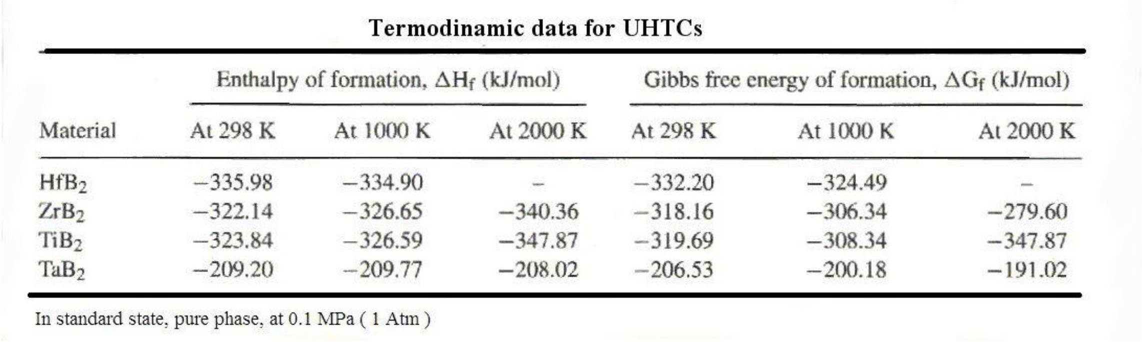

Termodinamic data for UHTCs

	Enthalpy of formation, ΔH_f (kJ/mol)			Gibbs free energy of formation, ΔG_f (kJ/mol)		
Material	At 298 K	At 1000 K	At 2000 K	At 298 K	At 1000 K	At 2000 K
HfB_2	−335.98	−334.90	–	−332.20	−324.49	–
ZrB_2	−322.14	−326.65	−340.36	−318.16	−306.34	−279.60
TiB_2	−323.84	−326.59	−347.87	−319.69	−308.34	−347.87
TaB_2	−209.20	−209.77	−208.02	−206.53	−200.18	−191.02

In standard state, pure phase, at 0.1 MPa (1 Atm)

Table 1.III [49].

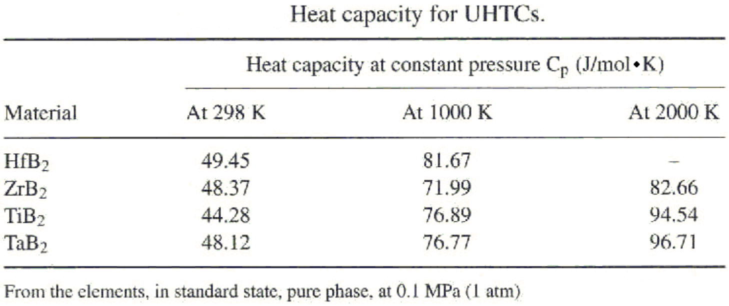

Heat capacity for UHTCs.

	Heat capacity at constant pressure C_p (J/mol•K)		
Material	At 298 K	At 1000 K	At 2000 K
HfB_2	49.45	81.67	–
ZrB_2	48.37	71.99	82.66
TiB_2	44.28	76.89	94.54
TaB_2	48.12	76.77	96.71

From the elements, in standard state, pure phase, at 0.1 MPa (1 atm)

Table 1.IV [49].

1.3 Synthesis and densification methods

The conventional method for densifying UHTCs is hot pressing, performed either with or without sintering additives. Significant research has examined alternative processing routes for UHTCs to reduce processing times and temperatures and, therefore, reduce the cost associated with the techniques. Some of these alternative techniques also improve the oxidation resistance of the material.

The presence of secondary phases in the microstructure has a detrimental effect on the material high temperature capability by introducing grain boundary phases, which can have lower melting temperatures and provide routes for oxygen diffusion into the material. The presence of oxygen impurities can be detrimental to the densification ability of the starting powder or cause rapid grain growth; it also contributes to the formation of secondary phases. Nitrides and reducing additives have been added to the powders to enhance sinterability [50-53], but these additives introduce secondary phases to the material.

The principal source of elemental zirconium metal, in particular, is the zirconium silicate mineral, zircon ($ZrSiO_4$). The mineral baddeleyite, a natural form of zirconia (ZrO_2), is a secondary source of zirconium. Zircon is also the primary source of all elemental hafnium, which is contained in zircon at a ratio of about 1 part hafnium to 50 parts zirconium [54]. During diboride production, the respective metal oxide is used as the metal source while boron carbide, crystalline boron or a combination of boron oxide and carbon acts as the boron source. Due to the limited demand for diboride powders of Zr and Hf, the processes for manufacturing these powders have not been refined to the same degree as for other common ceramics, such as SiC or Si_3N_4.

The main production techniques used for formation of UHTC materials are as follows:

1. Hot pressing (HP)
2. Spark-plasma sintering (SPS)
3. Self-propagating high-temperature synthesis (SHS)
4. Reactive hot pressing (RHP)
5. Pressureless sintering (PS)

Furthermore, methods of polymer impregnation and pyrolysis (PIP) are employed, although on a substantially smaller scale (mainly for creating refractory protective matrices and coatings on C_f/C and C_f/SiC composites), as well as chemical vapor deposition (CVD) and often also combinations of these approaches. For the efficient application of these methods, the development of precursors and starting reagents with given properties is necessary [6].

Due to the hard brittle nature of the UHTC materials, diamond tooling is typically required to machine components. Electron Discharge Machining (EDM) can be used as an alternative to diamond grinding to machine the borides due to the high electrical conductivity of this materials. This is an advantage over some of the carbide, nitride and oxide materials that typically have higher resistances, which does not allow them to be machined using EDM.

1.3.1 Hot pressing (HP)

The densification of ZrB_2 powder generally requires very high temperatures [55], owing to the covalent character of the bonding as well as to its low volume and grain boundary diffusion rates. Typically, HP of ZrB_2 required a temperature of 2100°C or above and moderate pressure (20÷30 MPa) [56-58], or lower temperatures (~ 1800°C) and extremely high pressures (> 800 MPa) [59, 60]. These studies [56-60] showed that densification of ZrB_2 is a diffusion-controlled rate process. Results of HP studies on commercially available ZrB_2 powders are summarized in table 1.V, which includes details of the starting powders, sintering additives, HP conditions, mixing method and final densities. It has been found that HP of coarse ZrB_2 powder ($d \approx 20$ μm) at 2000°C with a pressure of 20 MPa achieved only a relative density of ~ 73% [57], whereas the relative density of ~ 91% was obtained for a finer ZrB_2 powder ($d \approx 2.1$ μm) under the same HP conditions [58]. Furthermore, the attrition-milled ZrB_2 powder, with average particle size of $d \leq 0.5$ μm, required HP at 1900°C and 32 MPa for 45 min to achieve full density [30]. The lower HP temperature was attributed to reduction of starting particle size from microns ($d \approx 2.1$ μm) to submicrons ($d \leq 0.5$ μm) by attrition-milling.

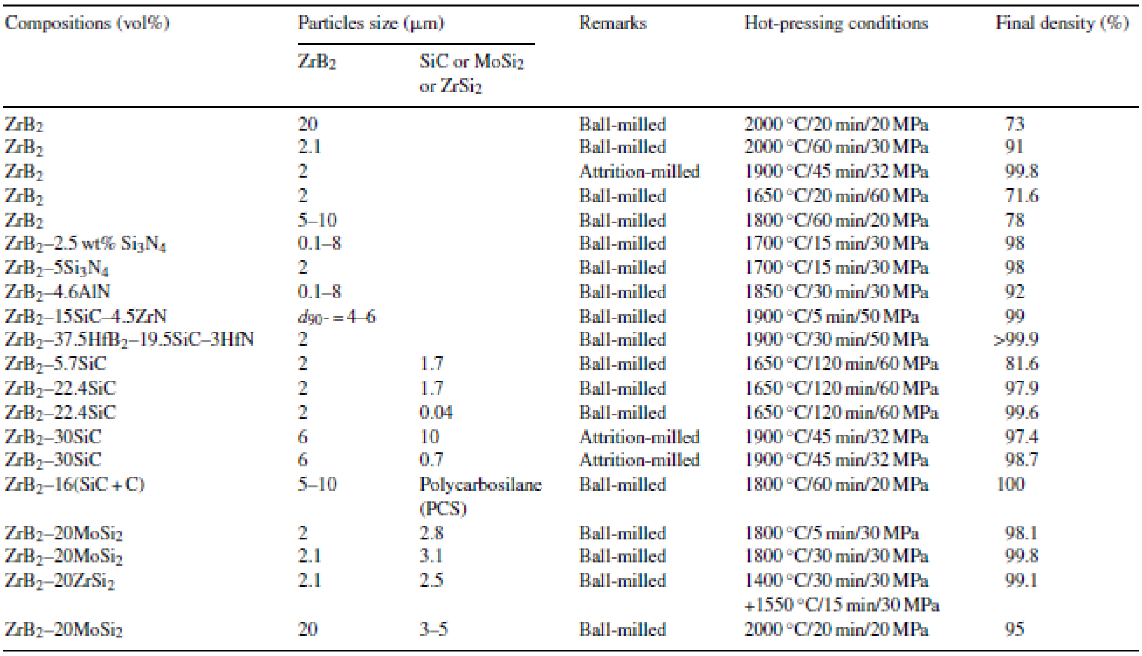

Compositions (vol%)	Particles size (μm)		Remarks	Hot-pressing conditions	Final density (%)
	ZrB_2	SiC or $MoSi_2$ or $ZrSi_2$			
ZrB_2	20		Ball-milled	2000 °C/20 min/20 MPa	73
ZrB_2	2.1		Ball-milled	2000 °C/60 min/30 MPa	91
ZrB_2	2		Attrition-milled	1900 °C/45 min/32 MPa	99.8
ZrB_2	2		Ball-milled	1650 °C/20 min/60 MPa	71.6
ZrB_2	5–10		Ball-milled	1800 °C/60 min/20 MPa	78
ZrB_2–2.5 wt% Si_3N_4	0.1–8		Ball-milled	1700 °C/15 min/30 MPa	98
ZrB_2–5Si_3N_4	2		Ball-milled	1700 °C/15 min/30 MPa	98
ZrB_2–4.6AlN	0.1–8		Ball-milled	1850 °C/30 min/30 MPa	92
ZrB_2–15SiC–4.5ZrN	d_{90}- = 4–6		Ball-milled	1900 °C/5 min/50 MPa	99
ZrB_2–37.5HfB_2–19.5SiC–3HfN	2		Ball-milled	1900 °C/30 min/50 MPa	>99.9
ZrB_2–5.7SiC	2	1.7	Ball-milled	1650 °C/120 min/60 MPa	81.6
ZrB_2–22.4SiC	2	1.7	Ball-milled	1650 °C/120 min/60 MPa	97.9
ZrB_2–22.4SiC	2	0.04	Ball-milled	1650 °C/120 min/60 MPa	99.6
ZrB_2–30SiC	6	10	Attrition-milled	1900 °C/45 min/32 MPa	97.4
ZrB_2–30SiC	6	0.7	Attrition-milled	1900 °C/45 min/32 MPa	98.7
ZrB_2–16(SiC + C)	5–10	Polycarbosilane (PCS)	Ball-milled	1800 °C/60 min/20 MPa	100
ZrB_2–20$MoSi_2$	2	2.8	Ball-milled	1800 °C/5 min/30 MPa	98.1
ZrB_2–20$MoSi_2$	2.1	3.1	Ball-milled	1800 °C/30 min/30 MPa	99.8
ZrB_2–20$ZrSi_2$	2.1	2.5	Ball-milled	1400 °C/30 min/30 MPa +1550 °C/15 min/30 MPa	99.1
ZrB_2–20$MoSi_2$	20	3–5	Ball-milled	2000 °C/20 min/20 MPa	95

Table 1.V: Starting powder size, hot pressing conditions and final densities of the hot-pressed ZrB_2 ceramics and ZrB_2-based composites with various additives [61].

Oxygen impurities (B_2O_3 and ZrO_2) present on the starting powder surfaces have been shown to inhibit densification and to promote grain growth in the non-oxide ceramic systems. Recently, metallic Ni [22, 62], SiC [29-35, 58], Si_3N_4 [52, 63], AlN [51, 64], HfN or ZrN [50, 65] have been added to ZrB_2, producing an intergranular secondary phase and/or reducing oxygen content, both of which assists in the densification of ZrB_2. Silicon carbide is the most common additive for ZrB_2 or HfB_2 ceramics. The addition of SiC improved the sinterability, inhibited grain growth and increased the oxidation and ablation resistance of ZrB_2 and HfB_2 ceramics as well [29-35, 58]. The improvement of densification upon addition of SiC was attributed to the formation of intergranular liquid phases during hot-pressing, assisting in densification at lower temperatures [31, 32]. However, the improvement of densification upon addition of ultra-fine SiC is effective only for a uniformly dispersed SiC-ZrB_2 system [58]. The agglomeration of the ultra-fine SiC particles led to reduced improvement in densification of ZrB_2, even with nano-sized SiC particles [58].

Nitrides are other effective additives for improving sinterability or enhancing densification of ZrB_2. The main reason for incorporating nitrides as additives is the propensity of nitrides to consume the oxygen-bearing species on the diboride powder surfaces. The reduction of oxygen results in higher boron activity, which is one of the conditions favoring lattice diffusion and, therefore, densification [66]. The addition of ≥ 2.5 wt.% Si_3N_4 results in almost fully dense ZrB_2 (relative density (RD): ~ 98%) after compactions at 1700°C and 30 MPa for 15 min [52, 63]. Some grain boundary phases, including BN, ZrO_2, $ZrSi_2$ and borosilicate glassy phase, were confirmed to be present in pockets at multiple-grains junctions for the ZrB_2-based ceramics with Si_3N_4, the result of a reaction of an oxide impurity with Si_3N_4. That reaction results in elimination or decrease in the oxide impurity on the ZrB_2 particles surfaces, thereby promoting densification [52, 63]. Similar to Si_3N_4, the primary effect of an AlN additive is the depletion of the ZrB_2 particles from the outer oxide layer that prevents the formation of highly dense compacts [51]. Compared to AlN and Si_3N_4 additives, the ZrN and HfN showed the unexpected advantage of limiting undesirable secondary phases that eventually become detrimental to high temperature stability. The resulting composites showed a fine and homogenous microstructure with secondary phases such as M(C, N), MO_2 (M = Zr and/or Hf) and BN. The formation of the secondary phases during sintering was traced back to the interactions among ZrN or HfN, carbon, and oxides such as B_2O_3 and ZrO_2 or HfO_2. These interactions accelerated the densification of ZrB_2 or HfB_2 ceramics by reducing the oxygen content on the starting powder surfaces. The resulting intergranular secondary phases possess higher refractoriness than those made with AlN or Si_3N_4 additives.

Transition metal disilicides have been found to be an alternative and effective sintering additive because they improve sinterability and increase oxidation resistance of ZrB_2 ceramics as well. In the early 1970s, Kinoshita et al. [57] systematically investigated densification behavior of ZrB_2-based composites with $MoSi_2$. Recently, it has been reported that HP of the ZrB_2-based ceramics with $MoSi_2$ required only a temperature ≤ 1800°C [36-38]. The higher sintering temperature required in the earlier study resulted from larger ZrB_2 ($d \approx 20$ μm) and $MoSi_2$ ($d \approx 5$ μm) particles. More recently, Guo et al. [40] found that addition of 10÷40 vol.% $ZrSi_2$ could further lower the densification temperature of ZrB_2 to 1550°C or below. Furthermore, fully dense ZrB_2-$ZrSi_2$ composites with a fine and homogeneous microstructure, using a two-step HP process, which consisted of a first stage at 1400°C for 30 min and a second stage at 1550°C for 15 min at a pressure of 30 MPa were obtained. Improvement of densification, resulting from addition of disilicides, is attributed to two major causes. One is formation of an intergranular Si-O-B liquid phase between $MoSi_2$ or $ZrSi_2$ and ZrB_2 particles due to the interaction of SiO_2 and B_2O_3 that occurs on the surfaces of particles [67]. Another is the ductile deformation of $MoSi_2$ or $ZrSi_2$ particles at high temperature (> 800°C) [68, 69]. This deformation could force soft $MoSi_2$ or $ZrSi_2$ particles to fill in the voids left by the ZrB_2 skeleton under pressure during sintering, thus improving densification [38, 40].

1.3.2 Spark plasma sintering (SPS)

SPS, or Field Assisted Sintering Technology (FAST), is one of the most recent advanced processing techniques developed for densifying ceramic materials [70, 71] (Fig. 1.7).

Although SPS is similar to HP, in place of indirect heating, the applied electrical field heats the die and the powder compact. One advantage of using SPS is to enhance densification of poorly sinterable ceramics, by simultaneously applying a uniaxial load and a direct or pulsed electric current to a powder compact. Another advantage is that the grain growth of starting materials is restricted, since a considerable shorter sintering time (within minutes) is needed compared to HP or hot isostatic pressing (HIP), thereby retaining the fine and homogeneous grains. Previous investigations [72-74] of compaction of oxide, nitride and carbide ceramics produced by SPS have shown that the sintering time, heating rate and sintering temperature are the important factors controlling fine-grained microstructure and densification.

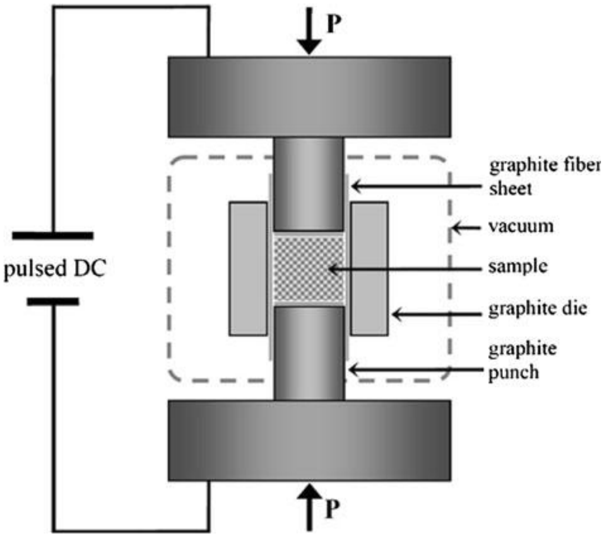

Figure 1.7: Schematic of SPS equipment [75].

SPS has been shown to provide a processing route for these highly refractory materials that does not require sintering aids. The technique has been particularly successful when using starting powders fabricated using an SHS method [76].

Materials produced by SPS have displayed comparable and/or improved mechanical properties and oxidation resistance when compared with hot pressed materials. The reason for the superior oxidation resistance may be the removal of surface oxides during sintering. The storage and processing of ZrB_2 (and HfB_2) in air results in the formation of surface oxides on the powder particles [77]. These surface oxides not only inhibit the sinterability of the diboride, but they also introduce oxides such as B_2O_3 into the bulk material. The presence of these low-melting-point oxides has a detrimental effect on the high-temperature mechanical properties and oxidation resistance. The pulsed electrical current used during SPS is thought to cause thermal or electrical decomposition of insulating surface oxides [78, 79], although the process by which the SPS method achieves this and the rapid sintering rates is not yet fully understood.

Table 1.VI summarizes SPS conditions, final density and grain size of ZrB_2-based ceramics produced by SPS. Medri et al. [80] showed that $60ZrB_2$-30ZrC-10SiC (vol.%) composition could be sintered to a relative density of ~ 96% at 2100°C and 30 MPa for 2 min. Grain size measurement indicated that the grain growth (maximum grain size:

~ 3 μm) was inhibited during SPS. Recently, the various ZrB_2-ZrC-SiC compositions could be sintered to the fully dense compacts with fine and homogenous microstructure at 1950°C and 30 MPa for 2 min, by using the SPS technique [81]. This discrepancy in the sintering temperature is probably associated with starting powder size and SPS conditions. In addition, extending soaking time from 3 min to 5 min can produce fully dense ZrB_2-ZrC-SiC composites at a lower temperature (1900°C) [64]. Furthermore, addition of 5 wt.% AlN results in complete densification at 1850°C and 30 MPa for 5 min, but addition of 5 wt.% Si_3N_4 still required a temperature of 1900°C. The discrepancy in densification temperature due to additions of AlN and Si_3N_4 is likely attributable to a lower onset temperature of densification and a faster shrinking rate for the AlN addition as compared to the Si_3N_4 addition [64]. For the ZrB_2-15 vol.% $MoSi_2$ [37], however, the density and grain size measurements of the compacts consolidated at 1750°C showed that SPS was not superior to HP. Soaking time and total sintering time were noticeably shorter for SPS (7÷24 min) than for HP (20÷140 min).

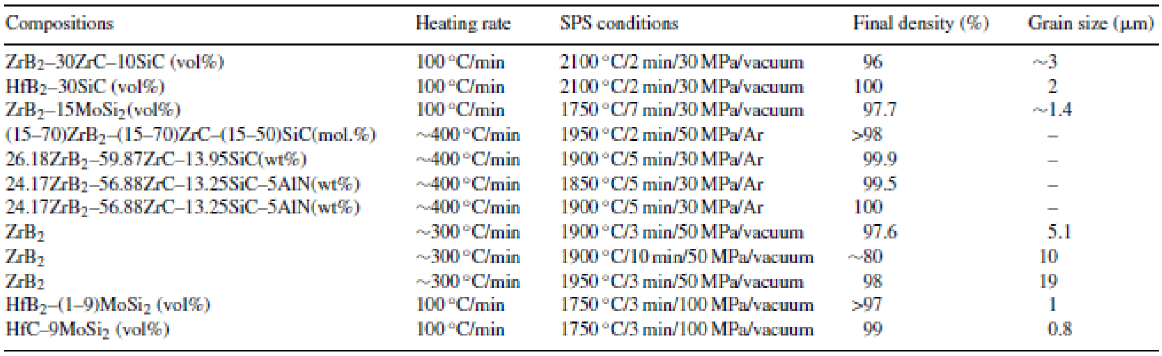

Compositions	Heating rate	SPS conditions	Final density (%)	Grain size (μm)
ZrB_2–30ZrC–10SiC (vol%)	100 °C/min	2100 °C/2 min/30 MPa/vacuum	96	~3
HfB_2–30SiC (vol%)	100 °C/min	2100 °C/2 min/30 MPa/vacuum	100	2
ZrB_2–15$MoSi_2$(vol%)	100 °C/min	1750 °C/7 min/30 MPa/vacuum	97.7	~1.4
(15–70)ZrB_2–(15–70)ZrC–(15–50)SiC(mol.%)	~400 °C/min	1950 °C/2 min/50 MPa/Ar	>98	–
26.18ZrB_2–59.87ZrC–13.95SiC(wt%)	~400 °C/min	1900 °C/5 min/30 MPa/Ar	99.9	–
24.17ZrB_2–56.88ZrC–13.25SiC–5AlN(wt%)	~400 °C/min	1850 °C/5 min/30 MPa/Ar	99.5	–
24.17ZrB_2–56.88ZrC–13.25SiC–5AlN(wt%)	~400 °C/min	1900 °C/5 min/30 MPa/Ar	100	–
ZrB_2	~300 °C/min	1900 °C/3 min/50 MPa/vacuum	97.6	5.1
ZrB_2	~300 °C/min	1900 °C/10 min/50 MPa/vacuum	~80	10
ZrB_2	~300 °C/min	1950 °C/3 min/50 MPa/vacuum	98	19
HfB_2–(1–9)$MoSi_2$ (vol%)	100 °C/min	1750 °C/3 min/100 MPa/vacuum	>97	1
HfC–9$MoSi_2$ (vol%)	100 °C/min	1750 °C/3 min/100 MPa/vacuum	99	0.8

Table 1.VI: Spark plasma sintering conditions, final density and grain size of ZrB_2 ceramics and ZrB_2 or HfB_2-based composites produced by an SPS process [61].

Without sintering additives, full density has, historically, been achieved only by HP at temperatures ≥ 2100°C [56, 57]. Densification and grain growth occurred simultaneously during the sintering. As a result, it was difficult to obtain a full density ZrB_2 compact. SPS of ZrB_2 ceramics required a temperature of 1900°C, a holding time of 3 min and a heating rate of 200°C/min or above. Increasing the sintering temperature to 1950°C or extending the holding time to 10 min or above, as well as lowering the heating rate below 200°C/min, led to coarsening of the grain size. In addition, SPS has been used for applications in other transition metal diborides, such as HfB_2-SiC [37], TiB_2-WB_2-CrB_2 [82], TiC-TiB_2 [83], HfB_2-$MoSi_2$ [84] and HfC and HfB_2-based composites with $MoSi_2$ additives [85]. The enhanced densification resulting from SPS was attributable to mass transfer processes, which are significantly enhanced in the process, effectively promoting densification. The mechanism in SPS technique that enhances densification - mainly whether or how an electric discharge is involved in accelerating the densification and grain growth - is still the subject of intense debate. However, it is suggested that enhancement is most probably due to (i) an efficient heat transfer; (ii) the use of comparatively high pressure; (iii) the presence of an electrical field (use of DC pulses); and (iv) the presence of local spark discharges generated between the powders under high-energy electrical pulses.

1.3.3 Self propagating high temperature synthesis (SHS)

SHS is not a densification method but uses solid-state combustion to produce materials by using internally generated chemical energy from exothermic reactions. The characteristics of this method include fast reaction times, low energy requirements, simple experimental apparatus and high-purity products. A disadvantage is that the reactions are difficult to control.

SHS can also be used to prepare ZrB_2 powders using inexpensive raw materials [86]. When used for the production of powders, the high heating and cooling rates involved are thought to introduce planar defects, such as stacking faults, and linear defects such as dislocations whose associated strain fields increase the sinterability of the powders by providing a driving force for rearrangement of atoms. ZrB_2 powders can be formed by SHS using zirconium and boron [87]. The powders are dry mixed and cold pressed to form pellets. The pellets are ignited and the process is an explosive one accompanied by a large gas release. As a consequence, the resulting material is too fragile to be used as a bulk material, although X-ray diffraction indicates it is ZrB_2.

SHS has several advantages over conventional hot pressing of UHTCs, such as control of exaggerated grain growth and lower processing temperatures. However, several problems with hot pressed materials have been overcome by addition of reinforcing phases and refinement of starting powder size.

1.3.4 Reactive hot pressing (RHP)

RHP has been identified as a potential route to produce ZrB_2 ceramics with low impurity levels and high density at a lower temperature. There are two processes that occur in RHP, *in situ* reaction of precursor powders and densification, which must be completed simultaneously during heating and subsequent holding.

Recently, RHP has been used to produce ZrB_2 and/or HfB_2 dense compacts by using Zr and/or Hf and B precursors as well as to fabricate the ZrB_2-based composites with SiC and/or ZrC by using Zr, Si and B_4C precursors. Table 1.VII summarizes RHP sintering conditions, precursors, grain size and final density of the ZrB_2 ceramics and ZrB_2-based ceramics fabricated by RHP.

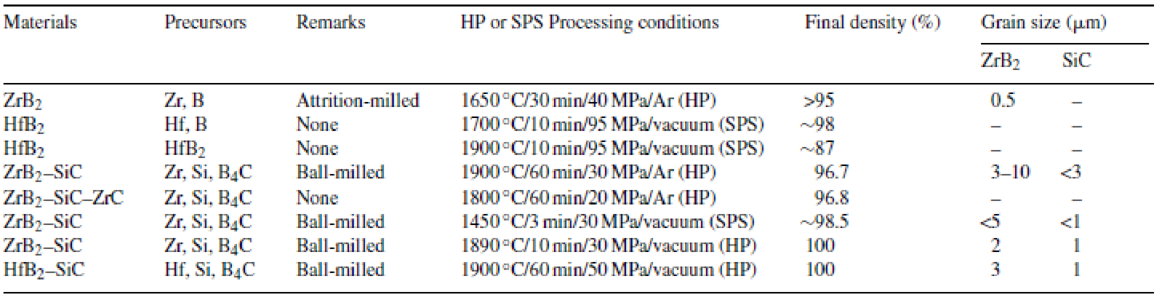

Materials	Precursors	Remarks	HP or SPS Processing conditions	Final density (%)	Grain size (μm)	
					ZrB_2	SiC
ZrB_2	Zr, B	Attrition-milled	1650 °C/30 min/40 MPa/Ar (HP)	>95	0.5	–
HfB_2	Hf, B	None	1700 °C/10 min/95 MPa/vacuum (SPS)	~98	–	–
HfB_2	HfB_2	None	1900 °C/10 min/95 MPa/vacuum (SPS)	~87	–	–
ZrB_2–SiC	Zr, Si, B_4C	Ball-milled	1900 °C/60 min/30 MPa/Ar (HP)	96.7	3–10	<3
ZrB_2–SiC–ZrC	Zr, Si, B_4C	None	1800 °C/60 min/20 MPa/Ar (HP)	96.8	–	–
ZrB_2–SiC	Zr, Si, B_4C	Ball-milled	1450 °C/3 min/30 MPa/vacuum (SPS)	~98.5	<5	<1
ZrB_2–SiC	Zr, Si, B_4C	Ball-milled	1890 °C/10 min/30 MPa/vacuum (HP)	100	2	1
HfB_2–SiC	Hf, Si, B_4C	Ball-milled	1900 °C/60 min/50 MPa/vacuum (HP)	100	3	1

Table 1.VII: Reactive hot-pressing conditions, precursors, grain size and final density of ZrB_2 or HfB_2 ceramics and ZrB_2 or HfB_2-based composites fabricated by a RHP method [61].

The main advantage of RHP compared with SHS from a processing point of view is that the displacement reactions can take place at much lower temperatures than those that occur during SHS. The heating rate during reactive hot pressing must be sufficiently slow (~ 10°C/min) to prevent spontaneous self-combustion. The starting powder size and morphology has a strong effect on the microstructure in RHP ceramics.

The improvement of densification by RHP was attributed to the formation of nano-sized ZrB_2 particles during the reactive process because the fine crystalline size should enhance the driving force for densification when the densification is driven by minimization of the surface free energy.

Another application of RHP is to produce ZrB_2-based composites with SiC and/or ZrC, using Zr, Si and B_4C powders as precursors. Zhang et al. [88] used RHP to fabricate ZrB_2-based composites with SiC, by reacting Zr, Si and B_4C at 1800°C where the following reaction (1.1) is thermodynamically favorable:

$$2\,Zr + Si + B_4C = 2\,ZrB_2 + SiC \qquad (1.1)$$

The relative density of ~ 98% was obtained by RHP of Zr, Si and B_4C powder mixtures at 1900°C and 30 MPa for 60 min. Later, Wu et al. [89] also successfully consolidated ZrB_2-SiC-ZrC composites (RD: ~ 97%) by RHP of Zr, Si and B_4C powders at 1800°C and 20 MPa for 60 min in an argon atmosphere. They found that the reactions for producing ZrB_2, ZrC and SiC were not simultaneously induced during the sintering, but in steps. ZrB_2 and ZrC were first formed by the reaction of B_4C with Zr at a low temperature, then SiC was produced by reaction of Si with ZrC and the residual B_4C at a higher temperature. In addition, Zimmermann et al. [90] found that excess B_4C and Si were necessary in the ZrH_2-B_4C-Si system for obtaining ZrB_2-SiC composites without oxide impurity as well as for avoiding grain coarsening during the sintering process. Similarly, RHP is also used to produce the HfB_2-based composites. Monteverde [91] obtained a fully densified HfB_2-22 vol.% SiC-6 vol.% HfC at 1900°C and 50MPa for 60 min through reaction of a mixture of Hf, B_4C and Si powders.

Recently, RHP has also been utilized to produce HfB_2 by reaction of Hf and B powders at a low temperature, by using SPS. An almost fully densified HfB_2 compact was achieved by reacting Hf and B at 1700°C and 95 MPa for 10 min in vacuo using SPS [92], instead of HP. For comparison, HfB_2 ceramics produced from commercially available powder could achieve only ~ 62% and ~ 87% densities at 1800°C with 30÷85 MPa for 10 min and at 1900°C with 80÷95 MPa for 10 min [92], respectively. The reaction between Hf and B occurred at 1100°C, while the completion of the reaction extended over a relatively wide temperature range [92]. However, the association of the reaction with densification was absent during the reactive sintering. Densification was observed only at a temperature where the conversion to the diboride was complete. Thus, the simultaneous synthesis and consolidation of the Zr, B, or B_4C and Si precursor powders, i.e. reactive sintering, could produce the densified ZrB_2-based composites at a lower temperature by using either HP or SPS, as compared with direct consolidation of commercially available powders.

1.3.5 Pressureless sintering (PS)

In studies that were conducted in the 1970s and earlier, densification of ZrB_2 ceramics was only accomplished by HP [27, 57, 59, 60]. Because of the extreme pressures required for densification, pressureless sintering of ZrB_2 was considered unlikely or impossible until the late 1980s, when studies of pressureless sintering actually began to show results. Compared with HP, the development of a PS process would enable almost-net-shape processing of ceramic parts with complex geometries using standard powder-processing methods, thus reducing processing costs. Various additives have been used to improve densification of ZrB_2. In general, the additives used can be divided into two main groups: liquid phase formers and reactive agents. Table 1.VIII summarizes the PS conditions, agents used, grain size and final density of the resulting ZrB_2 ceramics.

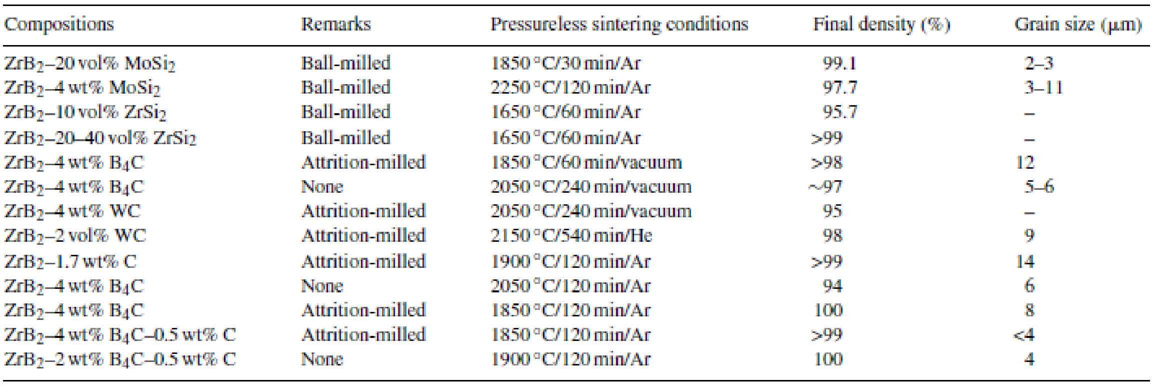

Compositions	Remarks	Pressureless sintering conditions	Final density (%)	Grain size (μm)
ZrB_2–20 vol% $MoSi_2$	Ball-milled	1850 °C/30 min/Ar	99.1	2–3
ZrB_2–4 wt% $MoSi_2$	Ball-milled	2250 °C/120 min/Ar	97.7	3–11
ZrB_2–10 vol% $ZrSi_2$	Ball-milled	1650 °C/60 min/Ar	95.7	–
ZrB_2–20–40 vol% $ZrSi_2$	Ball-milled	1650 °C/60 min/Ar	>99	–
ZrB_2–4 wt% B_4C	Attrition-milled	1850 °C/60 min/vacuum	>98	12
ZrB_2–4 wt% B_4C	None	2050 °C/240 min/vacuum	~97	5–6
ZrB_2–4 wt% WC	Attrition-milled	2050 °C/240 min/vacuum	95	–
ZrB_2–2 vol% WC	Attrition-milled	2150 °C/540 min/He	98	9
ZrB_2–1.7 wt% C	Attrition-milled	1900 °C/120 min/Ar	>99	14
ZrB_2–4 wt% B_4C	None	2050 °C/120 min/Ar	94	6
ZrB_2–4 wt% B_4C	Attrition-milled	1850 °C/120 min/Ar	100	8
ZrB_2–4 wt% B_4C–0.5 wt% C	Attrition-milled	1850 °C/120 min/Ar	>99	<4
ZrB_2–2 wt% B_4C–0.5 wt% C	None	1900 °C/120 min/Ar	100	4

Table 1.VIII: Pressureless sintering conditions, grain size and final densities of the pressureless sintered ZrB_2 ceramics with various additives [61].

Liquid phase formers include refractory metals, such as Ni, Fe, Co and Mo [93-95], as well as disilicides of transition metals, such as $MoSi_2$ [96, 97] and $ZrSi_2$ [39]. Cech et al. [93] found that addition of ≥ 2 wt.% of metals was required to bring about adequate sintering, because formation and continuous action of a liquid phase occurred only at higher contents of added metals. The additions are more efficient for producing adequate sintering in an argon atmosphere than in vacuo because of loss of the added metals in the vacuum from volatilization. Lattice parameter measurements showed a gradual decrease in the crystal lattice dimensions during sintering, resulting from substitution of zirconium atoms in the ZrB_2 lattice by the atoms of the added metals. Obviously, the mode of action of these metallic additives that influence sintering is associated with an appreciable contraction of the ZrB_2 crystal lattice. Presumably, the contraction of the ZrB_2 crystal lattice affected the surface free energy and consequently increased the driving force for densification.

Kislui and Kuzenkova [94] found that with Mo additions up to 15 wt.% the energy of activation of the densification process drops below 380 kJ/mol from 680 kJ/mol because

Mo was incorporated into a ZrB_2 solid solution. As a result, the addition of Mo activates diffusion processes during sintering, effectively promoting densification. This densification behavior of Mo is also found in ZrB_2-20 wt.% SiC mixture powder that could be sintered without pressure to a relative density exceeding 97.7% at 2250°C for 120 min when 4 wt.% Mo was added [98]. Other studies found that the addition of 20 vol.% $MoSi_2$ produced the almost fully densified ZrB_2 at 1850°C for 30 min without external pressure [96, 97]. Furthermore, the additions of $\geq$ 20 vol.% $ZrSi_2$ further reduced the densification temperature; the full density was obtained at 1650°C for 60 min [39].

Differing from the previously mentioned liquid phase formers, reactive agents act as densification aids by reacting with the oxide impurities present on the surface of starting particles (such as ZrO_2 and B_2O_3) which inhibit densification. The main reactive agents used recently include B_4C [53, 99, 100], C [99-101] and/or WC [53, 102]. Chamberlain et al. [102] showed that elimination of oxide impurities on ZrB_2 particles surface by the reactions of B_4C or WC with ZrO_2 was the key to densification. The above-mentioned reactions are thermodynamically favorable at a temperature $\geq$ 1200°C for B_4C, but > 1500°C for WC. As a result, the discrepancy in densification temperature between the two agent-doped ZrB_2 ceramics is likely associated with their different onset temperatures for the reactions.

Moreover, grain size measurement showed that excess B_4C restricts the grain growth during sintering. A similar densification and grain growth inhibition effect of B_4C was also reported in ZrB_2-containing B_4C and carbon, either alone or in combination [100]. In addition, the densification effect of B_4C depended on the starting ZrB_2 powder size [100]. ZrB_2 with a particle size of ~ 2 µm allows sintering to a density of ~ 95% at 2050°C for 120 min. For comparison, ZrB_2 could be achieved with full densification at 1850°C for 60 min when the particle size was reduced to ~ 0.5 µm by an attrition milling. Furthermore, the densification is more effective for a combination of B_4C and C than for B_4C alone. Using a combination of B_4C and C, the same ZrB_2 powder (~ 2 µm) could be sintered to almost full density at 1900°C for 120 min. However, the additional densification effect of carbon does not appear in the reduced particle size ZrB_2 powder (~ 0.5 µm), which could be sintered to a full density at 1850°C for 60 min using either B_4C or a combination of B_4C and carbon.

1.4 Properties

1.4.1 Thermal properties

Typical values for the coefficient of thermal expansion (CTE) and thermal conductivity of some UHTC materials including HfB_2, ZrB_2 and these diborides with SiC are given in table 1.IX [46]. In general, the CTE's for these materials increase sufficiently with temperature such that temperature dependent coefficients should be used during design. To illustrate this, a comparison of CTE of pure HfB_2, pure SiC and HfB_2-20 vol.% SiC is shown in figure 1.8(left).

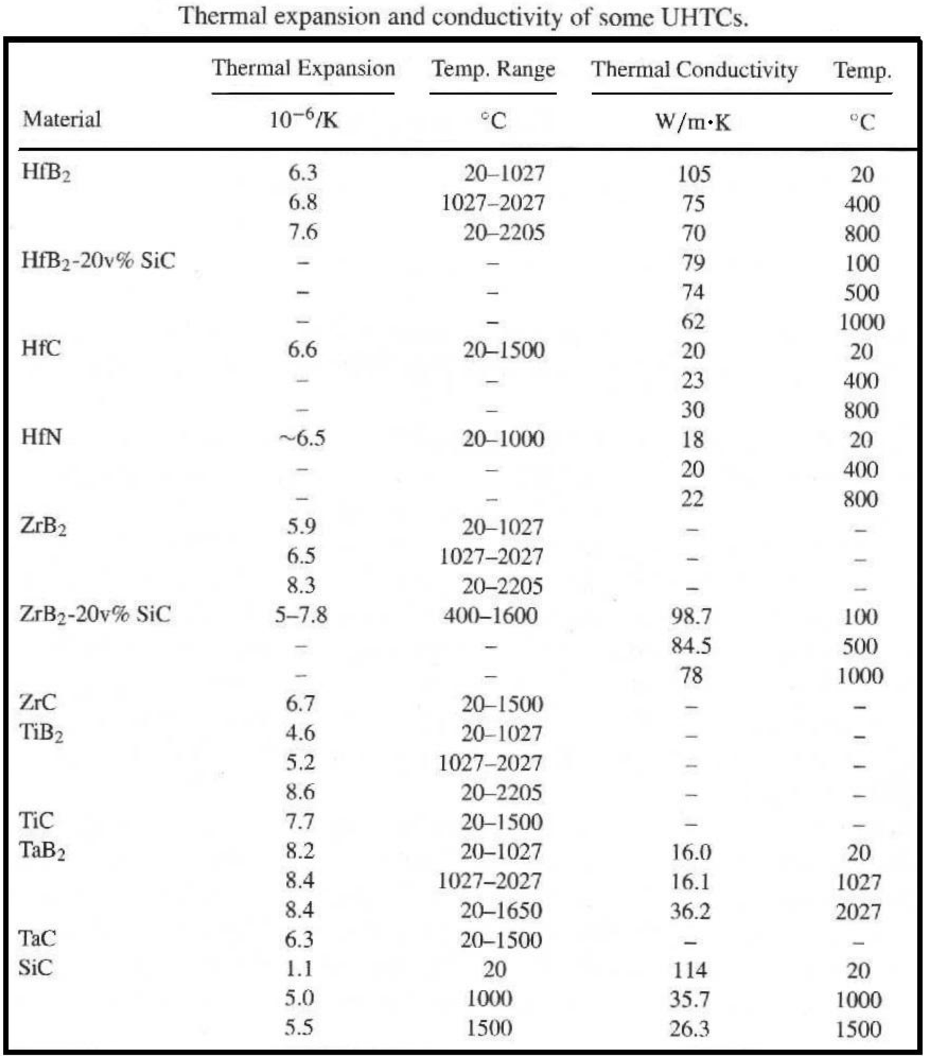

Thermal expansion and conductivity of some UHTCs.

Material	Thermal Expansion 10^{-6}/K	Temp. Range °C	Thermal Conductivity W/m·K	Temp. °C
HfB_2	6.3	20–1027	105	20
	6.8	1027–2027	75	400
	7.6	20–2205	70	800
HfB_2-20v% SiC	–	–	79	100
	–	–	74	500
	–	–	62	1000
HfC	6.6	20–1500	20	20
	–	–	23	400
	–	–	30	800
HfN	~6.5	20–1000	18	20
	–	–	20	400
	–	–	22	800
ZrB_2	5.9	20–1027	–	–
	6.5	1027–2027	–	–
	8.3	20–2205	–	–
ZrB_2-20v% SiC	5–7.8	400–1600	98.7	100
	–	–	84.5	500
	–	–	78	1000
ZrC	6.7	20–1500	–	–
TiB_2	4.6	20–1027	–	–
	5.2	1027–2027	–	–
	8.6	20–2205	–	–
TiC	7.7	20–1500	–	–
TaB_2	8.2	20–1027	16.0	20
	8.4	1027–2027	16.1	1027
	8.4	20–1650	36.2	2027
TaC	6.3	20–1500	–	–
SiC	1.1	20	114	20
	5.0	1000	35.7	1000
	5.5	1500	26.3	1500

Table 1.IX [46].

As previously indicated, the thermal conductivities of borides are typically higher in comparison to many other ceramics and are a result of both a lattice and an electronic contribution to phonon transport [5]. Figure 1.8(right) illustrates the large difference in conductivities of the borides from the nitride and carbide ceramics of hafnium [103-105]. Although the conductivities of the borides initially drop with increasing temperature, they eventually even out at levels still above that for the nitrides and carbides. For a leading edge, high thermal conductivity reduces thermal stresses within the material, by reducing the magnitude of the thermal gradients within the part. High thermal conductivity also allows energy to be conducted away from the tip of the leading edge and reradiated out of surfaces of the component with lower heat fluxes, reducing the surface temperature for a given incident heat flux, compared to an insulating material.

The added benefits of high temperature materials with high conductivity can be seen when comparing a sharp UHTC leading edge to a relatively blunt, low conductivity leading edge such as the conventional RCC (Reinforced Carbon Carbon) thermal protection system, used on the shuttle. Because of the low conductivity of conventional leading edge thermal protection system (TPS) materials, the maximum surface temperature is determined by a balance of the incident heat flux with the energy that is re-radiated out of the leading edge, hence the need for materials with an emittance as high as possible. Due to the low thermal conductivity of these materials there is little or no conduction of energy away from the tip of the leading edge.

Currently the leading edges of operational space vehicles are relatively blunt, due to temperature capability of the state of the art materials, which are typically based on SiC and limited to ~ 1600°C, before active oxidation becomes an issue. As the leading edge radius decreases the surface temperature increases. But the blunt leading edges significant1y impact the vehicles performance, which effects overall vehicle safety, as mentioned earlier. Therefore, in order to achieve maximum performance, materials are needed that are both capable of withstanding the reentry environment at temperatures greater than 2000°C and have a high thermal conductivity that will direct more energy away from the tip of the leading edge allowing for even further improvements in vehicle performance, i.e. faster velocities at lower altitudes.

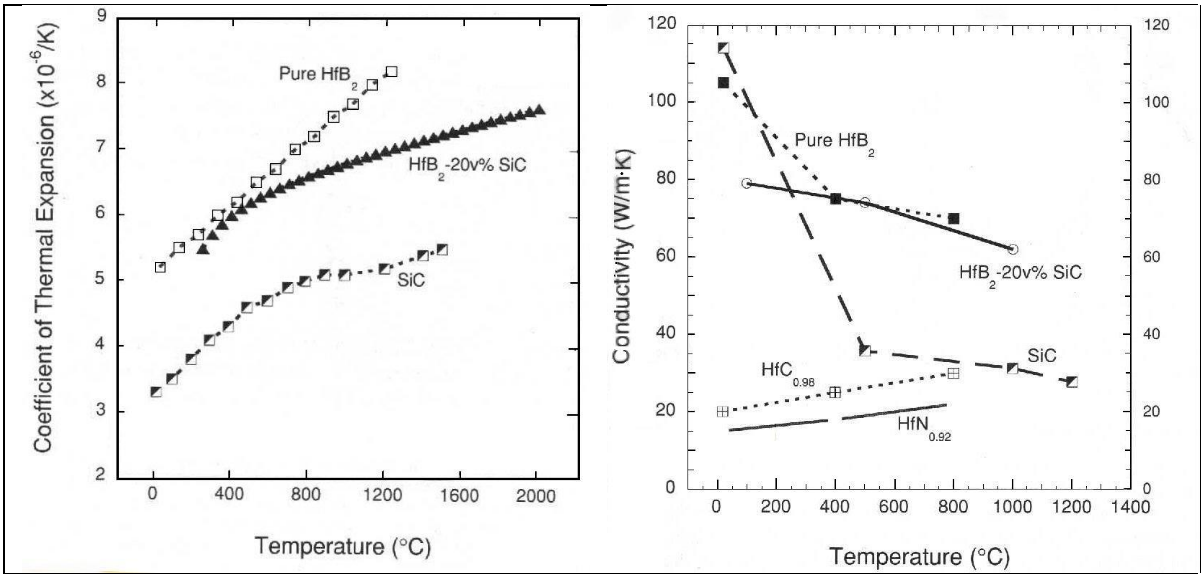

Figure 1.8: Left, plots of CTE vs. temperature for HfB_2, SiC and HfB_2-20 vol.% SiC [104, 105]. Right, plots of conductivity vs. temperature for several UHTCs [103-105].

Figure 1.9 illustrates how the surface temperature for the sharp UHTC leading edges is determined by an energy balance of incident heat flux, re-radiated energy and energy pulled away from the leading edge tip and re-radiated out the sides of the component where the incident heat flux is lower. In this sharp leading edge design, three dimensional heat transfer plays an important role in understanding and achieving the full potential of these materials. Thus the need for highly conducting, yet refractory materials is essential in the design of sharp vehicles.

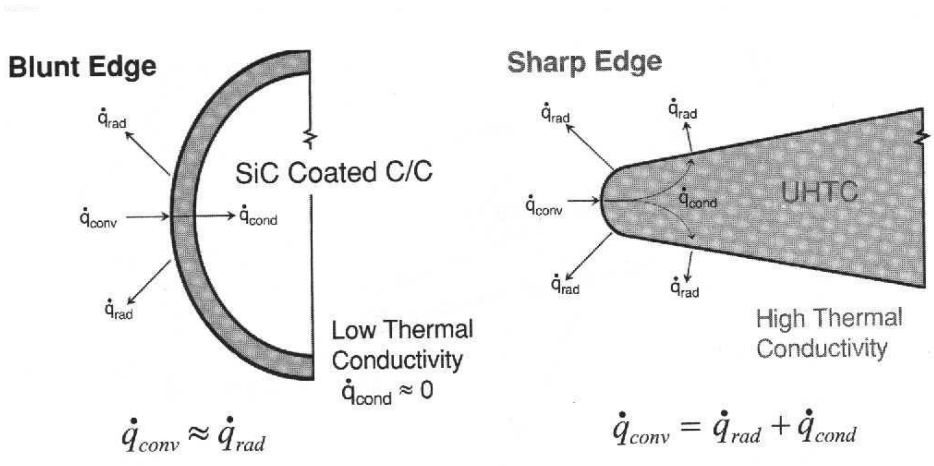

Figure 1.9: Comparison of the functionality of conduction for blunt and sharp leading edge designs of a hypersonic space vehicle [25].

1.4.2 Mechanical behavior

The mechanical properties of a number of materials, including HfB_2 and ZrB_2 with and without SiC additions, are given in table 1.X. Hardness values in these materials are typically relatively high, due to their high degree of covalent bonding. The wide scatter in the data is due to differences in processing of these materials resulting in different grain sizes and porosity [3].

The Young's modulus of HfB_2 and ZrB_2 ceramics ranges from ~ 350 GPa to 530 GPa, depending on porosity and additives; for a fully densified ZrB_2 without additive, it is equal to 498 GPa [30]. Historic studies have shown the Young's modulus of the fully densified hot-pressed polycrystalline ZrB_2 to be equal to 500 GPa [5, 106]. The additions of Ni, AlN, SiC, Si_3N_4, B_4C and C affect the Young's modulus of ZrB_2 ceramics. The modulus of HfB_2 and ZrB_2 with and without SiC addition begins to fall off above 800°C [47, 105, 107, 108]. The Young's modulus of fully densified solids is determined principally by interatomic forces, which decrease sharply with the interatomic distance [109]. The addition of Ni caused a decrease in the crystal lattice dimensions of ZrB_2, as a result of substitution of Zr atoms in the ZrB_2 lattice by atoms of the added Ni [93]. Therefore, the increase of Young's modulus due to Ni addition is associated with the decrease in the crystal lattice dimensions of ZrB_2. B_4C alone or a combination of B_4C with C also led to an increase in Young's modulus. In contrast, AlN and Si_3N_4 additions led to a lower Young's modulus. The different changes with the additives are associated with the different grain-boundary phase developed between ZrB_2 grains [51, 63, 100], which result from the interactions of the additives with impurities on the ZrB_2 particles surfaces, because the grain-boundary phase affects the Young's modulus of ceramics [64, 110].

For a fully densified composite, Young's modulus, E_c, may be described by the rule of mixtures [111]

$$E_c = \sum_{i=1}^{n} E_i V_i \qquad (1.2)$$

where E_i is Young's modulus of ith constituent phase, V_i is volume fraction of ith constituent phase and n is total number of constituent phases. A comparison between the measured and predicted values found that Young's modulus of pore-free ZrB_2-based composites obeys the rule of mixtures.

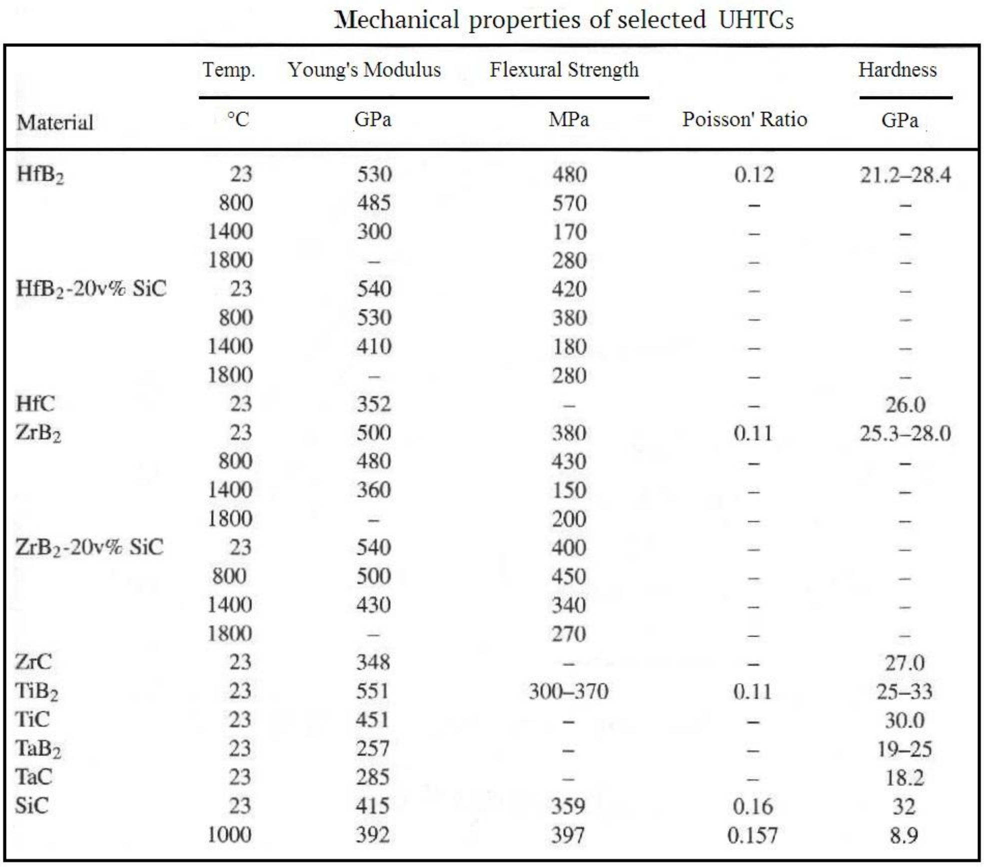

Mechanical properties of selected UHTCs

Material	Temp. °C	Young's Modulus GPa	Flexural Strength MPa	Poisson' Ratio	Hardness GPa
HfB_2	23	530	480	0.12	21.2–28.4
	800	485	570	–	–
	1400	300	170	–	–
	1800	–	280	–	–
HfB_2-20v% SiC	23	540	420	–	–
	800	530	380	–	–
	1400	410	180	–	–
	1800	–	280	–	–
HfC	23	352	–	–	26.0
ZrB_2	23	500	380	0.11	25.3–28.0
	800	480	430	–	–
	1400	360	150	–	–
	1800	–	200	–	–
ZrB_2-20v% SiC	23	540	400	–	–
	800	500	450	–	–
	1400	430	340	–	–
	1800	–	270	–	–
ZrC	23	348	–	–	27.0
TiB_2	23	551	300–370	0.11	25–33
TiC	23	451	–	–	30.0
TaB_2	23	257	–	–	19–25
TaC	23	285	–	–	18.2
SiC	23	415	359	0.16	32
	1000	392	397	0.157	8.9

Table 1.X [46].

It has been found that Young's modulus of the pores-containing ZrB_2-based composites is mostly dominated by the porosity. For ceramic materials, the use of a linear empirical dependence has been recommended. Assuming that the effect of pore structure and shape on Young's modulus is neglected, Young's modulus, E, can be given by [112]

$$E = E_0(1 - \alpha P) \qquad (1.3)$$

where E_0 is Young's modulus of pore-free materials, α is a constant and P is the volume fraction of porosity in the material.

In addition, the effect of pore structure and shape on Young's modulus have been investigated by other researchers [113, 114]. These studies demonstrated that the local elastic moduli decrease when the pore shape changed from spherical to oblate, as a result of the increased stress concentration around the pore. Therefore, the effective elastic modulus measured is lower for the case of non-spherical pores than for the case of spherical pores. Also, it has been found that elastic properties have a different sensitivity to porosity, regardless of pore shape. Bulk modulus is most affected by porosity; Young's modulus is the next most-affected modulus, followed by the shear modulus (which is slightly less sensitive than Young’s modulus). In contrast, Poisson’s ratio is insensitive to additives as well as to porosity and it remains almost constant for the various ZrB_2-based composites [38, 40, 64, 82].

Fracture toughness was in the range 2.4÷4.8 MPa $m^{1/2}$. For the ZrB_2 ceramics with low fracture toughness, intragranular cracking is common with the cracks propagated across ZrB_2 grains without being deflected along the grain boundaries. For the ZrB_2 with high fracture toughness, intergranular cracking is partially present. Thus, large grains and intergranular cracking are required for increasing fracture toughness. Also, the fracture toughness measured is larger in the ZrB_2 with nitrides and/or carbides than with metallic additives. This difference seems to be associated with a larger tensile residual thermal stress in the ZrB_2 ceramics with metallic additives than in the ZrB_2 ceramics with carbide and/or nitride ceramic additives.

Rezaie et al. [34] found that the fracture toughness of ZrB_2-based composites with SiC is dominated by the SiC particles size and distribution in the composites. Increased fracture toughness produced by SiC addition is attributed to the crack deflection that occurs near the SiC particles and/or at ZrB_2/SiC interfaces. The interactions of the crack with the microstructure are most likely controlled by the complex residual stress state that develops during cooling from the processing temperature; that in turn is caused by the thermal expansion mismatch between the ZrB_2 and SiC particles. The contribution of crack deflection to increasing fracture toughness depends on the total number of crack deflections and the crack deflection angle, i.e. crack propagation path. Crack deflection is enhanced in larger diameter grains. The increase of fracture toughness that accompanies crack deflection is also associated with the elastic and/or frictional bridging mechanism of grains. Elastic bridging is enhanced in larger diameter grains, while the frictional bridging mechanism is in operation only when crack deflection and grain pullout occur, which is prevalent in smaller diameter grains.

It was found that the flexural strengths range from 350 MPa to 580 MPa, depending on grain size, additives and on the relative density as well. In general, finer grain size results in higher strengths. Chamberlain et al. [30] showed that the addition of 10, 20 and 30 vol.% SiC led to the high room-temperature strengths of ZrB_2, typically ~ 1000 MPa, with fine ZrB_2 grain microstructure (average grain size: ~ 2÷3 μm).

Recently, the effects of microstructure and SiC grain size on room-temperature flexural strength were examined in hot pressed 30 vol.% SiC-containing ZrB_2 ceramics by Zhu et al. [33] and Rezaie et al. [34], both studies showed, based on the linear elastic fracture mechanics, that the critical flaw size correlates strongly with SiC particle size. Both studies concluded that the maximum SiC grain size in the ZrB_2-SiC composites is the strength-limiting factor and that the strength is not correlated with average ZrB_2 grain size. Although additives, such as Ni, SiC, nitrides and disilicides, could reduce the densification temperature of ZrB_2, the strength of the resulting composites is also degraded at high temperature, as a result of softening of the intergranular amorphous phase. For the ZrB_2-based ceramics with Ni and Si_3N_4, the strength degraded significantly above 800°C [55, 62]. For the ZrB_2-based ceramics with the Ni additive, in particular, the strength decreased sharply and dropped almost to zero at 1200°C. For comparison, the ZrB_2-based composites with $MoSi_2$ retained the constant strength at temperatures approaching 1200°C [37, 97]. However, the strength degraded rapidly above 1200°C, and the degradation was more rapid than in the ZrB_2 ceramics without additive. High-temperature strength may be improved by increasing the refractory index of the intergranular phase and minimizing impurities, as well as promoting crystallization of the intergranular amorphous phase [115].

1.5 Oxidation of transition metal diborides

Historical studies concluded that the relative oxidation resistances of ZrB_2 and HfB_2 were superior to those of other transition metal diborides [35]. The purpose of this section is to critically review historical and recent research related to the oxidation behavior of ultra-high temperature diboride ceramics with emphasis on ZrB_2 and HfB_2.

Zirconium and hafnium diborides undergo stoichiometric oxidation according to reactions (1.4) and (1.5) [116]. The expressions for the change in standard state Gibbs' free energy with reaction (ΔG°_{rxn}) were calculated for the temperature range from room temperature (~ 25°C) to ~ 2000°C using data from the standard reference tables [117] (reaction (1.4)) and thermodynamic software (reaction (1.5)) [118].

$$ZrB_2\,(cr) + 5/2\,O_2\,(g) \rightarrow ZrO_2\,(cr) + B_2O_3\,(l) \quad \Delta G^\circ_{rxn} = -\,1999500 + 374.4\,T\,[J] \quad (1.4)$$

$$HfB_2\,(cr) + 5/2\,O_2\,(g) \rightarrow HfO_2\,(cr) + B_2O_3\,(l) \quad \Delta G^\circ_{rxn} = -\,2000460 + 375.7\,T\,[J] \quad (1.5)$$

The reaction products, B_2O_3 and either ZrO_2 or HfO_2, show limited/no mutual solubility, so the scales contain two distinct phases. As with metals and other non-oxide ceramics, oxidation of these materials is favorable across a wide range of temperatures that includes from room temperature to > 2000°C. The implication is that differences in oxidation behavior depend on kinetic factors since a strong driving force exists across a wide temperature range. As such, the oxidation behavior of the phase-pure diborides is divided into two regimes based on whether the oxide that is formed is protective (at 'low' temperatures) or not (at 'high' temperatures).

Both ZrB_2 and HfB_2 exhibit mass gain kinetics consistent with diffusion limited processes in the low temperature regime. The upper limit of this regime depends on factors such as external pressure, oxygen partial pressure and gas flow-rate, but is generally considered to be between 1100°C and 1200°C in static air. Below the transition temperature, a protective oxide scale is formed on the surface of ZrB_2 and HfB_2 and both ceramics show parabolic trends for mass gain, scale thickness and oxygen consumption as a function of time [116, 119]. Historical [120] and current (Fig. 1.10(a)) analyses of cross-sections of oxidized specimens reveal a two layer oxide scale that consists of an outer layer of glassy B_2O_3 and an inner layer that contains porous ZrO_2 with the pores filled by glassy B_2O_3. More recently, Parthasarathy et al. [121-123] developed an oxidation model for TiB_2, ZrB_2 and HfB_2 showing that the oxidation rate is limited by the diffusion of oxygen through B_2O_3 (i.e. transport of oxygen through ZrO_2 is negligible). Based on the combination of historical and recent experimental and modelling results, diborides exhibit passive oxidation behavior with the formation of a protective oxide scale in the low temperature regime.

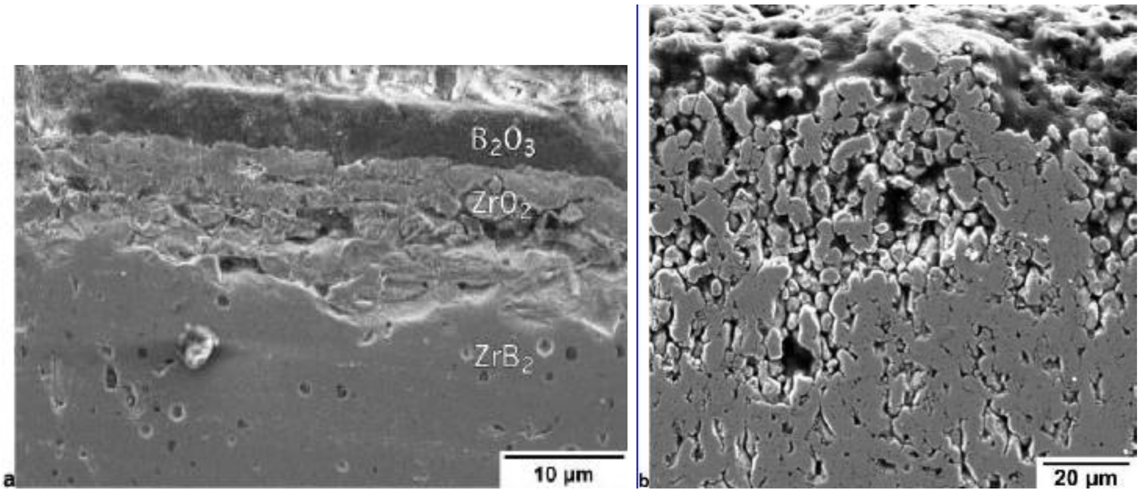

Figure 1.10: Cross-section images of oxide scale on nominally pure ZrB_2 oxidized in air at (a) 900°C for 8h (oxide layer thickness, ~ 10 μm) and (b) 1500°C for 2h (oxide layer thickness, ~ 400 μm) [124].

In the high temperature regime (i.e. above ~ 1200°C), the oxidation behavior of the diborides changes [119, 125-127]. Microstructural analysis (previous [120, 128] and Fig. 1.10(b)) reveals that loss of protection for ZrB_2 coincides with evaporation of B_2O_3 from the oxide scale. Thermodynamic models that employ either volatility diagrams [129, 130] or kinetic models, such as the one proposed by Parthasarathy et al. [121], support the evaporation of B_2O_3 as the cause of the transition. Thermodynamic models predict vapour pressures of the various gaseous boron oxides that form as a function of external conditions such as temperature, oxygen partial pressure, etc. As shown in Fig. 1.11, B_2O_3 (g) is the predominant vapour species formed by evaporation of B_2O_3 in air at 1500°C. Although B_2O_3 volatilises over a wide range of conditions, changes in the partial pressure of oxygen in the external atmosphere or temperature at which oxidation occurs affect the predominant species in the vapour phase. HfB_2 exhibits the best oxidation resistance of the diborides over this temperature range because the oxide layer that remains after B_2O_3 evaporation has a more equiaxed microstructure, which gives it greater resistance to oxygen transport [116]. Although ZrB_2 is inferior to HfB_2, both have significantly better oxidation protection than other diborides such as TiB_2, TaB_2 and NbB_2 [46].

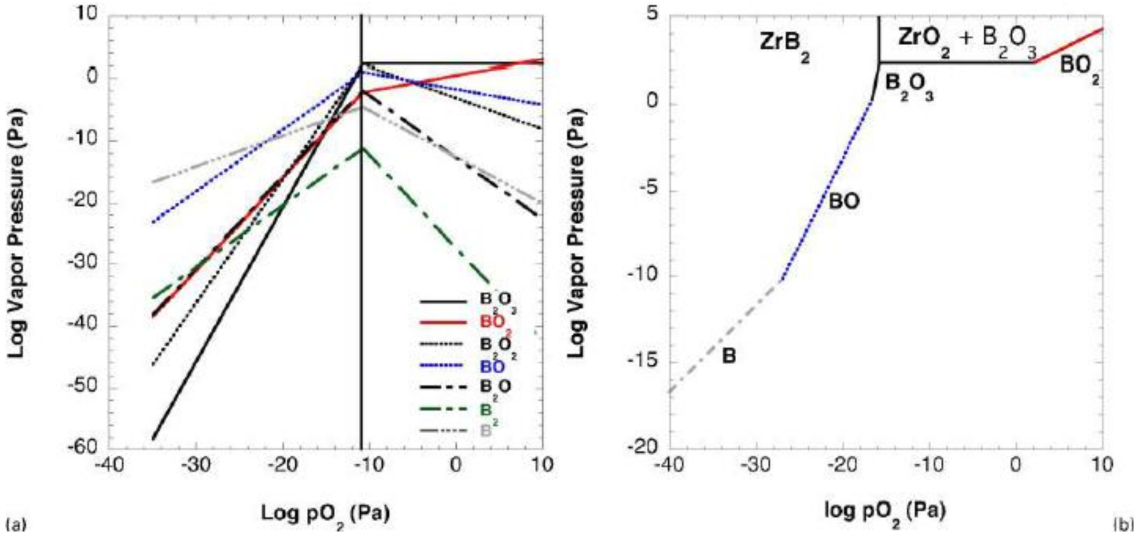

Figure 1.11: (a) vapour pressure of various B-O species as function of oxygen partial pressure at 1500°C and (b) ZrB_2 volatility diagram based on calculations [130].

Direct comparisons of historical and recent oxidation results for nominally pure diborides is difficult due to lack of convention in reporting results. Whereas historical studies have used a combination of mass gain, scale thickness, parabolic rate constant and oxygen uptake as a function of temperature and time, more recent studies have focused on thermal gravimetric analysis (TGA) to measure mass gain as a function of temperature and/or time. In addition, differences in oxidation temperature and time also complicate direct comparison, but table 1.XI provides an overview of some historical and recent reports [131]. Where direct comparisons are possible for nominally phase-pure diborides, the trends are consistent, but the quantitative values do not agree. No obvious differences in density, composition or microstructure can be identified as the cause of the difference in mass gain. Based on the model of Parthasarathy et al. [121], small changes in the fraction of porosity in the ZrO_2 have a significant effect on the oxidation rate. Trace impurities in the diborides are one potential cause of the differences in oxidation behavior.

Material	Oxidation conditions	Weight gain/mg cm^{-2}	Parabolic rate constant K_P/kg^2 m^{-4} s^{-1}
ZrB_2	1000°C, 4 h	1·1	…
	1500°C, 4 h	6·6	
ZrB_2	1200°C, 2 h	2·2	…
	1300°C, 2 h	2·8	
	1400°C, 2 h	5·6	
HfB_2	1522°C, 60 min	…	5×10^{-6}
ZrB_2	1522°C, 58 min		1×10^{-4}
ZrB_2	1166°C, 1 h	4·8	7×10^{-7}
	1256°C, 1 h	5·7	9×10^{-7}
ZrB_2	1025°C	…	9×10^{-4}
ZrB_2	1400°C, 2 h	18·7	…
ZrB_2	1500°C, 2 h	11	…
	1600°C, 2 h	14	

Table 1.XI: Summary of historical and recent oxidation results for nominally pure ZrB_2 and HfB_2 ceramics [124].

Furnace oxidation studies, such as those described above, do not reproduce conditions that are representative of extreme environments such as the aerothermal heating encountered during hypersonic flight. While the conclusions of these studies provide insight into oxidation mechanisms and may be useful for screening candidate materials, hypersonic flight produces higher heat fluxes, dissociated gaseous species and gas flow-rates that cannot be duplicated in typical laboratory furnaces [46]. Specialised facilities such as arc heaters [132], plasma wind tunnels [133], oxyacetylene torch testing [134] and inductively coupled plasma facilities [135] have been developed to test materials in more realistic environments.

The response of the refractory UHTC materials to high temperature oxidizing conditions imposed by furnace heating has been observed to differ markedly from the behavior observed in arc plasma facilities that provide a simulated reentry environment [136]. Furnace evaluations are normally performed for long times at fixed temperature and slow gas flow with well defined solid/gas-reactant/product chemistry. Arc jet tests, on the other hand, are carried out under high velocity gas flow conditions in which energy flux, rather than temperature, is defined. Furthermore, furnace studies employ air at 1 atmosphere and as diatomic species. But during a typical reentry profile for a manned space vehicle, the pressures will generally be much less than 1 atmosphere and a significant portion of the gas molecules will be dissociated into highly reactive monatomic species as they cross the bow shock formed during reentry. The resulting monatomic species may recombine at the surface giving up some of their energy to the material and, depending on the catalycity of the substrate, this recombination can add a significant fraction to the overall heating of the articles's surface. Because of the differences between static or flowing air oxidation experiments and experiments in the arc jet, correlation of material responses from the two test situations is difficult, if not impossible in many cases, i.e. if material A performs better in the furnace test than material B it does not necessarily hold that the same trend will occur in the arc jet [137].

Oxidation rates during furnace tests were found to be much greater than oxidation rates during arc jet testing [138]. This was explained by the formation of significant temperature gradients (between the oxide surface and materials substrate) during arc jet testing, that were otherwise absent during furnace tests. During arc jet testing the gradients maintained the bulk material at a lower temperature than the surface, thus reducing the levels of surface recession. The harsher conditions of the arc heater may have also resulted in a thinner scale due to loss of material by evaporation and/or flow off of the surface during testing. Further, it could be concluded that the more severe conditions encountered during arc heater testing may promote the formation of an oxide scale (ZrO_2 or HfO_2) having a higher density that is more protective than the scale formed in static laboratory furnace tests.

1.5.1 Oxidation of diborides ceramics containing SiC

The relatively poor oxidation resistance of nominally phase-pure diborides at temperatures above ~ 1200°C motivated researchers to investigate a number of approaches to improve oxidation resistance including solid solution additions, synthesising ternary diboride compositions and adding second phases [35]. The most promising approach was found to be the addition of SiC as a second phase, which reduced the thickness of the oxide scale across a wide temperature range when compared to either a pure diboride or pure SiC [29, 35]. The improved oxidation resistance was attributed to the formation of a stable borosilicate glass layer on the surface of the oxidized ceramics [120]. Since this pioneering work, research on oxidation resistant ZrB_2 and HfB_2 based compositions with silica scale forming additions has resulted in a significantly larger body of work on SiC containing materials than other systems.

Several groups have studied the effects of SiC additions on the behavior of diborides when exposed to air at elevated temperatures (Fig. 1.12). The reported behavior is summarized in table 1.XII.

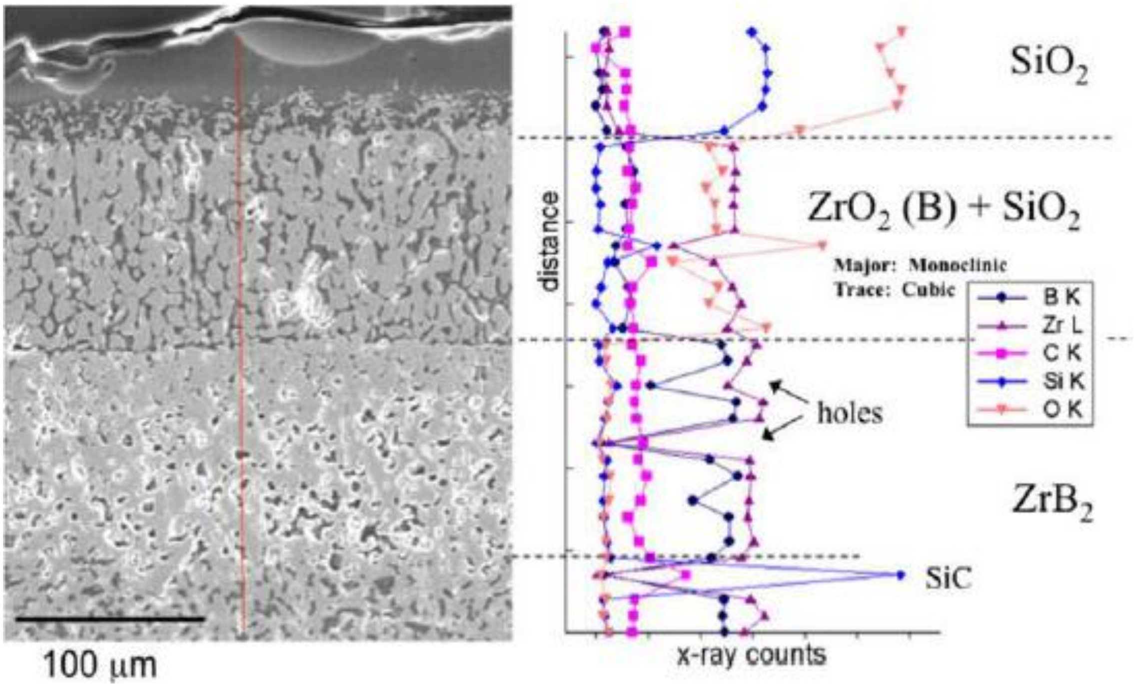

Figure 1.12: The layered structure that developed on ZrB_2-SiC oxidized by heating to 1627°C for 10 cycles. The oxide scale consists of an outer layer of SiO_2, a layer of ZrO_2 and SiO_2 and a layer of SiC depleted ZrB_2 on top of unreacted ZrB_2-SiC [139].

In addition to furnace oxidation and TGA studies that have been used to determine oxide layer thicknesses and mass gains as functions of time and/or temperature, recent progress has been made in the use of real time observations of growing oxide layers. Because diborides are electrically conductive, direct heating of specimens is possible using conventional furnace power supply and control systems [140, 141]. Direct heating allows observation of the specimen surface during oxidation, which has led to discoveries related to liquid convection and oxide particle transport during oxidation [142, 143]. Notably, this technique has led to the identification of zirconia rich nodules that grow up and through the liquid oxide (Fig. 1.13). The presence of these nodules has provided insight into potential causes for the variability in thicknesses of the outer glassy oxide and underlying partially oxidized regions noted by some authors [144-146].

Temperature range	Scale	Oxidation behaviour
<600°C	Native oxide	Little, if any mass gain/scale growth
600–1100°C	ZrO_2 or $HfO_2+B_2O_3$ SiC not oxidised	Parabolic kinetics due to presence of a dense glassy oxide layer (B_2O_3)
1100–1300°C	Borosilicate glass outer layer ZrO_2 or HfO_2+SiO_2 layer	B_2O_3 evaporation and SiC oxidation Paralinear kinetics: evaporation of B_2O_3 plus protection from borosilicate glass
1300–1600°C	Borosilicate glass outer layer	B_2O_3 evaporation, ZrO_2 transport, and SiC oxidation
	ZrO_2 or HfO_2+SiO_2 layer	Parabolic kinetics due to dense borosilicate glass layer
	Partially oxidised layer	SiC depletion observed in some cases
>1600°C	Gas pressure at scale/boride interface and scale evaporation	Bubbles in scale, presumably CO
		Evaporation of silica from scale The ZrO_2 scale can be protective or not

Table 1.XII: Summary of oxidation behavior of SiC containing ZrB_2 and HfB_2 ceramics [124].

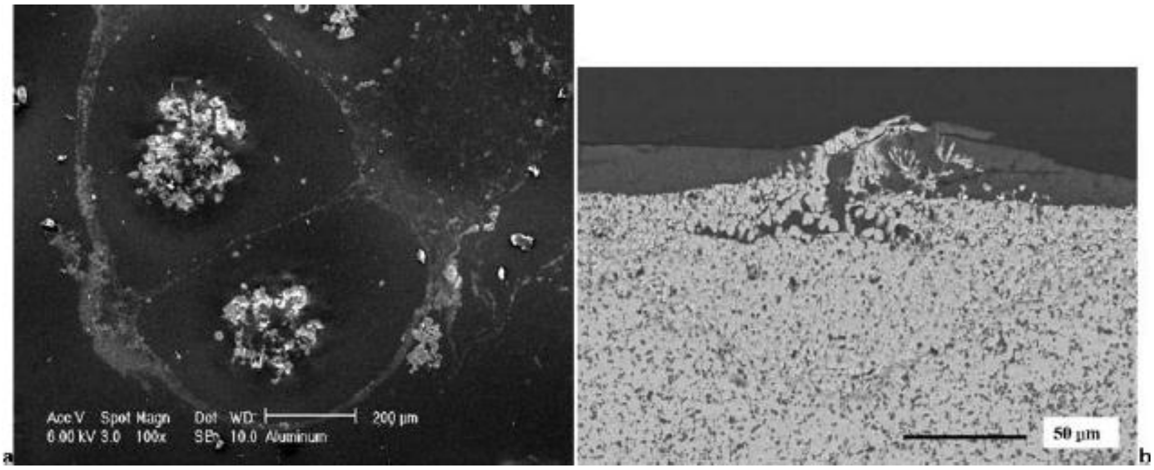

Figure 1.13: Images of ZrB_2-SiC after oxidation at 1550°C showing (a) lighter colored ZrO_2 rich nodules protruding through the darker glassy surface oxide layer [140] and (b) the cross-section of a lighter colored ZrO_2 rich nodule extending through the outer glassy oxide layer [142].

1.5.2 Additives

The oxidation products of a material formed during exposure to an oxidizing environment are largely responsible for the high-temperature performance of that material. This is determined by the extent to which the oxidized layer can protect the bulk material from subsequent oxidation. The physical and chemical processes that occur at the exposed surface depend on the microstructure and composition of the oxidized material. It follows that modification of the microstructure and composition can have a beneficial (or detrimental) effect on the material's oxidation resistance.

Additives can be used in several ways to improve the oxidation resistance of the UHTCs. The main areas of interest are as follows:

A. Increasing viscosity of the borosilicate liquid
B. Inhibiting the ZrO_2 polymorphic transformations
C. Using alternatives to SiC to introduce silicon
D. Forming protective refractory phases at high temperature
E. Modifying the microstructure of the ZrO_2 scale

A. Increasing viscosity of the borosilicate liquid

Systems with higher viscosity and increased liquidus temperatures inhibit oxygen diffusion to the unreacted bulk, retain the protective liquid at higher temperatures, and suppress evaporation of boria from the glassy phase. Diffusivity is inversely proportional to the viscosity of the liquid through which the diffusion is taking place, which is shown in the Stokes-Einstein relationship [147]

$$D = \frac{kT}{6\pi\eta r} \qquad (1.6)$$

where D is the diffusion constant, k is Boltzmann's constant, T is temperature in Kelvin, η is viscosity and r is the spherical particle radius.

The viscosity of the borosilicate glass can be increased even more by adding certain elements to the bulk material. The addition of tungsten, in 10 and 20 vol.% additions, to ZrB_2-SiC ceramics increased the viscosity of the borosilicate glassy phase significantly but also reduced the material's thermal shock resistance and structural stability at elevated temperatures, which is highly undesirable for sharp, leading-edge materials [129].

The oxidation resistance of hot-pressed ZrB_2 + 25 vol.% SiC composites has been improved by the addition of diborides of Cr, Ti, Ta, Nb and V [148]. These additions result in the production of the respective oxides in the glass. The improvement in oxidation resistance comes from the fact that borate and silicate glasses containing oxides of the elements listed (Group IV-VI transition metals) are immiscible and lead to phase separation. Such systems contain compositions with high viscosity and liquidus temperatures [147]. The immiscibility of the glass increases with increasing cation field strength of the metallic oxide forming element z/r^2 where z is the valence and r is the ionic radius. ZrB_2 ceramics with additions of 10 mol % CrB_2, NbB_2, TaB_2, TiB_2 and VB_2 had improved oxidation resistance, but most improvement was observed in the ZrB_2-SiC + 10 mol % TaB_2. The order in which the oxidation resistance was improved correlated well with the cation field strength of the modifying additive.

Opila et al. [149] investigated the effect of tantalum additions on the oxidation performance of zirconium diboride. They found that the addition of $TaSi_2$ improved the oxidation resistance of a ZrB_2 + 20 vol.% SiC composite. The oxidation rate was reduced by a factor of 10 at 1627°C. They concluded that more research was required to confirm that the improvement in oxidation was a result of the tantalum addition and not from the accompanying increase in silicon. It was suggested that the introduction of Ta resulted in immiscibility of the liquid formed on oxidation, which increased the viscosity of the liquid phase, providing a protective layer that was more resistant to volatilization.

The finer particles are more effective at trapping the liquid phase in the ZrO_2 layer and preventing oxygen transport through the liquid. The additives were effective only at small concentrations (~ 3.32 mol %) and at larger concentrations were detrimental to the oxidation resistance because of the formation of zirconia dendrites, which act as conduits for oxygen transport into the bulk. The addition of yttria has been investigated by several groups. Zhang et al. [150] found that adding 3 vol.% improved sinterability of the powders and suppressed grain growth by reacting with oxides on the starting powder surfaces. Grain size refinement improved the fracture toughness and flexural strength of the material. Adding LaB_6 to a ZrB_2 + 20 vol.% SiC UHTC [151] resulted in significantly higher fracture toughness compared with the same UHTC without the LaB_6 (5.7 MPa $m^{1/2}$ and 4.0 to 4.8 MPa $m^{1/2}$, respectively) because of enhanced crack deflection and bridging near SiC particles.

B. Inhibiting the ZrO_2 polymorphic transformations

The integrity of the oxide scale can be improved by inhibiting the ZrO_2 polymorphic transformations and their associated volume changes. In low temperature systems, this is achieved by the addition of stabilizing cations such as Mg, Ca and Y. However, these cations are lost from the ZrO_2 lattice at relatively low temperatures, and for UHTCs, alternative cations have been sought. The addition of a cation such as Ta results in substitution of the cation on the Zr site in ZrO_2, thus reducing the concentration of oxygen vacancies because of the higher valence of the cation (Ta forms Ta_2O_5 when oxidized). This decreases oxygen diffusion through the scale and stabilizes the oxide phase, increasing adhesion of the scale to the bulk ZrB_2-SiC material. The cation must be of higher valence and must form a refractory oxide scale. In addition to this, candidate additives must be introduced as a refractory phase and form a refractory oxide. The two best candidates are those based on niobium and tantalum, but tantalum is preferable as Ta_2O_5 has a melting temperature of 1880°C (compared with 1520°C for Nb_2O_5) [148]. Tantalum can be added in elemental form or as a carbide, boride, or silicide. The formation of intermediate phases should be considered. For instance, the addition of Ta_2O_5 could form $Ta_2O_5{*}6\ ZrO_2$ with ZrO_2. This phase has a lower melting temperature than the pure oxides and could have a beneficial or detrimental effect on the oxidation behavior of the composite.

C. Using alternatives to SiC to introduce silicon

Alternative methods of introducing Si to the system have been investigated. Ceramics in the system ZrB_2-Ta_5Si_3 have been investigated, as Ta_5Si_3 has a higher melting point than SiC (2500°C and 2300°C, respectively). Ta_5Si_3 provides the tantalum to induce glass immiscibility and silicon to form the protective borosilicate glass in the oxidized layer [152]. ZrB_2- and HfB_2-$TaSi_2$ composites have been formed by hot pressing [153], resulting in formation of a solid solution as the tantalum entered the boride matrix. The HfB_2-$TaSi_2$ displayed superior mechanical properties to the ZrB_2-based material. The substitution of Ti for SiC (e.g., a Zr-B-Ti system) has been suggested for making an alternative UHTC system because of the significantly reduced vaporization rate displayed by TiO_2 compared with SiO_2 [154].

D. Forming protective refractory phases at high temperature

Research into the introduction of additives to ZrB_2-SiC ceramics largely focuses on using the additives to alter the properties of the liquid phase formed at oxidation. A different approach is to use additives to form a solid refractory scale at high temperatures, which can resist oxidation at higher temperatures than the original material, thus providing effective protection to the underlying bulk and preventing subsequent oxidation. Candidate additives for this approach include those based on rare earth elements, in particular those containing lanthanum.

Lanthanum has also been added to a ZrB_2-SiC material as La_2O_3 [155], but resulted in the formation of an amorphous grain boundary phase and substantial ZrB_2 and SiC grain growth. The same work found that additions of other rare earth oxides (Y_2O_3 and Yb_2O_3) had beneficial effects on the densification, hardness and fracture toughness of the ZrB_2-SiC but did not investigate their effect on oxidation resistance.

Jayaseelan [156] investigated the addition of several rare earth (RE)-containing compounds to ZrB_2 + 20 vol.% SiC. Samples were prepared with 10 vol.% LaB_6, La_2O_3, or Gd_2O_3 and underwent oxidation testing at 1600°C. All samples successfully formed a thick (> 100 μm), dense layer of $RE_2Zr_2O_7$ during oxidation (Fig. 1.14). These zirconates have melting temperatures > 2300°C and will provide oxidation protection at temperatures when the borosilicate phase has vaporized from the exposed surface. Also, the reaction of the RE with ZrO_2 is expansive and therefore fills voids at the oxidized surface created by the removal of volatile species such as B_2O_3.

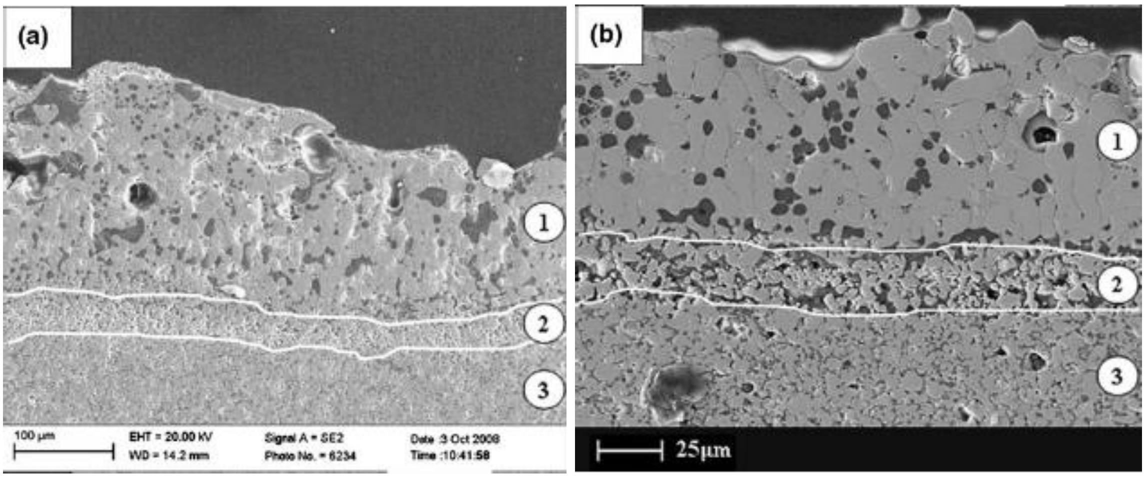

Figure 1.14: Secondary electron micrographs of oxidized scale on (a) ZrB_2-20 vol.% SiC-10 vol.% La_2O_3 and (b) ZrB_2-20 vol.% SiC-10 vol.% LaB_6 after oxidation for 1h at 1600°C showing (1) dense La-containing layer, (2) intermediate ZrO_2-containing layer and (3) unreacted bulk [156].

E. Modifying the microstructure of the ZrO_2 scale

Another novel technique is the use of additives to alter the microstructure of the ZrO_2 scale. By providing a liquid phase sintering route for the ZrO_2, it is possible to decrease the porosity of the scale and inhibit the subsequent transport of oxygen into the bulk material. As ZrO_2 has a melting point of 2715°C, a sufficiently dense scale would provide effective oxidation resistance at temperatures above those at which the boria or borosilicate phase is vaporized (~ 1600°C). This approach has been investigated by Zhang et al. [157] with additions of W to ZrB_2, which results in formation of a WO_3-ZrO_2 eutectic at ~ 1275°C. ZrB_2 + 4 mol % WC ceramics underwent TGA at 10°C/min to 1500°C and isothermal oxidation studies at 1500°C or 1600°C for 1, 2, or 3 hours in flowing air. The ZrB_2 + 4 mol % WC had better oxidation resistance than ZrB_2, as indicated by the normalized mass gain after TGA heating to 1500°C (~ 4.5 mg/cm^2 and ~ 14 mg/cm^2, respectively). ZrB_2 + WC also showed superior oxidation resistance in the isothermal oxidation tests at 1500°C and 1600°C, and the reduced mass gain of the ZrB_2 + WC samples was more significant at longer oxidation times, supporting densification of the ZrO_2 scale. The addition of WC to ZrB_2-SiC ceramics was also investigated and the presence of W increased the oxidation resistance of these ceramics as well. However, additional research is necessary to confirm that the improved oxidation resistance is caused by liquid phase sintering of the ZrO_2 scale.

1.6 Siliconized silicon carbide (Si-SiC)

Research on UHTCs slowed considerably until the early 1990's, when interest in the monolithic UHTC materials was renewed. The high costs of raw materials in addition to the high temperatures and pressures required to hot press UHTCs powders has led many new investigations into alternate starting materials and methods of fabricating UHTCs. In addition to conventional methods, researchers are also looking at reactive hot pressing and pressureless sintering by liquid infiltration and reaction [88, 116, 158]. These new reaction-based processes share the near-net shape and near-net dimension capabilities of gas-phase and liquid-phase reaction bonding as well as reduced processing temperatures and times required for solid state sintering.

Siliconised silicon carbide (Si-SiC) ceramics were developed originally as a potential nuclear fuel cladding material, now finding applications as submersible pump shaft seals. They have undergone successful trials as high-temperature gas turbine components, principally for the combustion chamber. Si-SiC is one of the promising CMC (Ceramic Matrix Composite) materials currently being promoted in Ultra High Temperature Heat Exchanger (UHTHE) systems for their improved heat transfer properties as well as their operational durability. Under solid fuel combustion conditions, however, the formation of ash deposition onto heat transfer surfaces of CMC tubes, reduces their envisaged thermal efficiency and long time applicability.

Silicon infiltrated reaction bonded Si-SiC, is an important member of this SiC-ceramics family, due to its suitability in oxidizing atmospheres at high temperature and the passivating effect of the silica scale formed during exposure. It not only protects against further oxidation, but also against corrosion by other gaseous species. To assure good protection, a good cohesion within the scale and adhesion to the Si/SiC substrate is required.

Si-SiC composites were developed in 1975 by Hillig and his collaborators. Their production involved conversion of the surface of a graphite component to silicon carbide by a vapour-phase reaction. In this way the easy machining of graphite is combined with the wear characteristics of silicon carbide. The mechanical properties of Si-SiC composites are similar to those of normal reaction-bonded silicon carbide.

Reaction-bonded (or self-bonded) silicon carbide covers a wide range of compositions and manufacturing processes, some of which have been used since the 1960s. Typical examples are the commercial materials REFEL and KT, and silicon-infiltrated sintered silicon carbides.

In general, a plastic body is formed using a mixture of silicon carbide powder (~ 5 μm), carbon or graphite and a plasticizer. In some variations of the process, silicon carbide powder and a char-forming plastic binder is used. The plastic body is pressed, extruded, injection moulded or otherwise formed into a green body. The plasticizers are then burned off or converted to a porous char by pyrolysis. Silicon either as a liquid or vapour, is then introduced into the body where it reacts with graphite or char to form silicon carbide *in situ*. The reaction product crystallizes on and serves to bond the primary silicon carbide powder. Excess silicon, about 10 vol.% is usually left to fill the pores, thus yielding a non-porous body. It is completely impermeable and fine-grained in structure, consisting of interlocking grains interspersed with a small proportion of free silicon and it has a very high strength, which can be retained up to the melting point of silicon, about 1413°C. These materials show good bending strength (at room temperature) in the order of 400÷600 MPa. When silicon melts, but skeleton is unaffected, the strength can be retained up to 50%. The Young modulus of this material is approximately 415 GPa.

1.6.1 Infiltration theory

Infiltration (also known as sinter casting) is a process whereby a molten phase is wicked into the open pores of a previously sintered porous structure [159]. The liquid is added from an external source. For infiltration to occur, the structure to be infiltrated should have pores which are open and interconnected. The preform to be infiltrated should have at least 10% porosity [159]. Infiltration offers the advantages of sintering at lower temperatures, shorter processing time, possibility of fully dense products, elimination of porosity with minimal dimensional change and near net-shaping without necessarily requiring application of an external pressure. It can also be successfully performed at low pressures giving a dense product. Below is a schematic illustration of the infiltration sequence (Fig. 1.15).

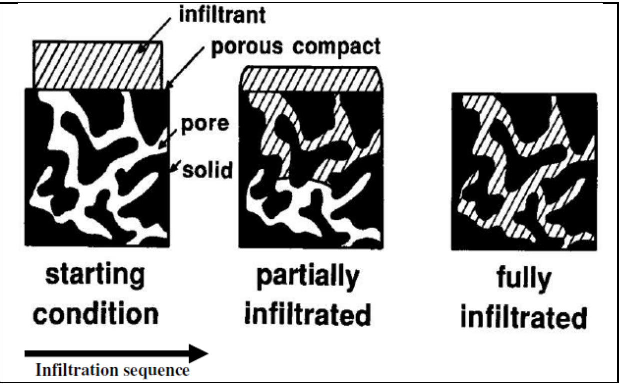

Figure 1.15: Schematic infiltration sintering, where the pore space in a powder or sintered porous structure is filled with molten phase by cycling to a temperature between the melting points between the two materials [159].

Infiltration can occur in two different ways, namely reactive infiltration and non-reactive infiltration. For a reactive infiltration system, there is interaction (reaction) between the melt (infiltrant) and the preform whereas for the non-reactive infiltration system, there is no interaction (reaction) between the melt and the preform. The former system mainly depends on the wetting behavior and the reaction between the melt and the preform whereas the latter system depends on the wetting behavior of the melt and the preform only. The infiltration process is sensitive to surface contamination therefore it requires clean surfaces for wetting.

A. Non-reactive infiltration

For the non-reactive infiltration system, the wetting behavior of the liquid and the preform material plays a major role. The wicking of the melt only occurs if the liquid wets the solid phase. The wetting and spreading of a liquid on a solid surface (Fig. 1.16) depend on short range molecular forces that can be modified by a monolayer coating. Wetting may cause compressive forces between particles and liquid migration.

A system with $\theta < 90°$ is considered as wetting and a system with $90° < \theta < 180°$ is considered as non-wetting.

The wetting angle of the interfacial tensions at the liquid-vapour-solid juncture is described by the Young equation ($\theta > 0$).

$$\cos\theta = \frac{\gamma_{SV}-\gamma_{SL}}{\gamma_{LV}} \qquad (1.7)$$ [160]

Where γ_{SV}, γ_{SL}, γ_{LV} are the effective interfacial tensions as indicated in Fig. 1.16(d).

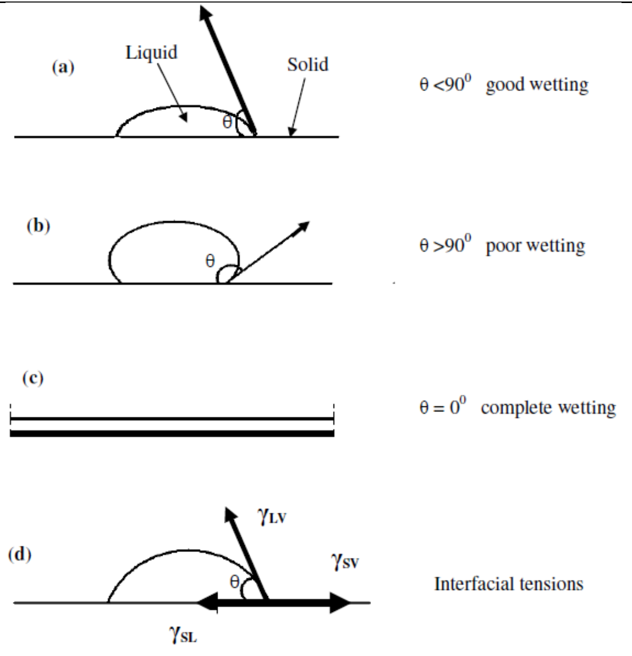

Figure 1.16: Wetting behavior between a liquid and a solid showing a) good wetting b) poor wetting c) complete wetting and d) the balance between the interfacial tensions for a liquid with contact angle θ [160].

Assuming cylindrical pore channels, the height of infiltration (height risen by the fluid in the preform), that can be obtained from the capillary force is:

From:

$$\Delta P = \frac{2\gamma_{LV}\cos\theta}{R_C} = \rho g \Delta H \qquad (1.8)$$

Thus

$$\Delta H = \frac{\Delta P}{\rho g} = \frac{2\gamma_{LV}\cos\theta}{R_C \rho g} \qquad (1.9)$$ [160]

Where: ΔH = height risen by the liquid; ΔP = internal pressure; ρ = density of the liquid; g = acceleration due to gravity; R_c = pore radius; γ_{LV} = surface tension; θ = contact (wetting) angle.

It can be deduced from equation 1.9 that fine pores give rise to a higher liquid rise (i.e. provide a greater suction) than larger pores.

Capillary pressure provides the driving force for infiltration and good wetting on the surfaces by the liquid is a key requirement. The kinetics of infiltration is complex [161]. However, if the pore structure of the preform is simplified as a set of parallel cylinders, the kinetics can be determined from Poiseuille’s equation of viscous flow through a tube. The average laminar flow velocity (υ) of a column of liquid in a horizontal cylindrical capillary is therefore given by the Poiseuille equation.

$$\upsilon = \frac{\Delta P {R_C}^2}{8\eta L} \qquad (1.10)$$ [161]

Combining equations 1.8 and 1.10, thus,

$$\upsilon = \frac{\gamma_{LV}\, R_C \cos\theta}{4\eta L} \qquad (1.11)\ [161]$$

Where η = viscosity of the liquid; L = length filled by the liquid.

From equation 1.11, it can be seen that the rate of penetration of the liquid into a preform, will be greater for a liquid of lower viscosity and higher surface tension and for pores of larger radius [161].

If time is taken into consideration during infiltration, the depth of infiltration varies with the square root of time. The height infiltrated in time t is then found to be:

$$h^2 = \left(\frac{\mathrm{r}\gamma\cos\theta}{2\eta}\right)t \qquad (1.12)\ [162]$$

Where, h = height of infiltration; r = radius of the tube; γ = surface tension of the liquid; θ = contact (wetting) angle; t = time taken for infiltration; η = viscosity of the fluid.

Equation 1.12 shows that the rate of infiltration is proportional to the pore size. Since the pore size increases with the particle size, preforms made with larger particles are more readily infiltrated [162]. Theoretically, it is possible to calculate the green density of the preform required to produce a fully dense composite, but in practice it is necessary to leave additional porosity to allow the infiltrating liquid to move freely.

In a non-wetting system, infiltration does not readily occur, as opposed to the wetting system. In-fact a liquid that is non-wetting tends to force particles apart. For such a system, for infiltration to take place, an external pressure has to be applied. This pressure should be greater than the maximum capillary resistance of the preform to the penetration of the liquid melt into the largest interfaces [162]. Darcy's law states that:

$$h^2 = \frac{2kt}{\mu(1-V_P)}\Delta P \qquad (1.13)\ [163]$$

Where, h = infiltration height; t = infiltration time; k = intrinsic permeability; V_p = particle volume fraction of packed sample; μ = viscosity of liquid melt; ΔP = pressure drop in the liquid.

When a plot of h^2 against pressure is done (Fig. 1.17), we get a straight line and this also shows the threshold pressure (P_o) that is needed to kick-start infiltration [163].

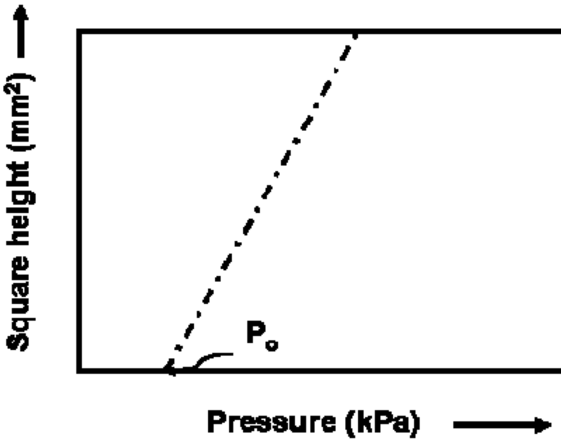

Figure 1.17: An illustration of Darcy’s plot of infiltration height vs. pressure [164].

B. Reactive infiltration

Reaction sintering is a method whereby objects are made by reacting two components in a mix in order to produce a third, ceramic phase. The high temperature needed to initiate the reaction is sometimes further boosted by the heat generated from the enthalpy of the reaction taking place. This high temperature further serves to sinter the particles of the new phase generated into a generally dense ceramic body. However, for the reaction sintering route, voids seem to be a problem if the reaction proceeds under low pressure conditions, due to volume reduction occurring during the reaction of carbon with silicon to form silicon carbide [165].

For a reactive infiltration system, the wetting behavior and the rate of reaction of the system plays a major role. There are many factors that influence these parameters. Good wetting is an important factor during reactive infiltration. A liquid possessing a low contact angle readily wets the solid thus allowing easier wicking of the liquid into the pores. Both carbon and SiC show good equilibrium wetting with liquid silicon.

Another important factor in such systems is the pore size distribution and porosity. For infiltration to occur, the preform should have at least 10% porosity and pores which are open and interconnected [159]. There is volume expansion of the solid phase during the reaction in the carbon-SiC system, so this means that there exists an optimal pore diameter that should allow full infiltration and at the same time accommodating this volume expansion. In the carbon-SiC system, too large pores are undesirable because there will be a high probability of ending up with free silicon in the final product. One major advantage to the reactive infiltration technique is the avoidance of porosity defects. Residual silicon (free silicon) of relatively low melting point (1410ºC) is detrimental to high-temperature application and it impairs the mechanical properties, so it has to be minimal in the final product [166].

For reactive infiltration to occur, temperature also plays a major role. Infiltration is carried out at temperatures higher than the melting point of the infiltrant but less than the softening or deformation temperature of the preform. Higher temperatures greater than the melting point of the infiltrant also have an advantage of reducing the melt viscosity thereby allowing easier wicking of the melt into the porous preform. The temperature has to be strictly controlled though, because there is a need to establish the refractoriness of the preform material so that maximum temperatures can be determined which will allow the melt viscosity to be reduced without compromising the preform material.

In most cases, the reaction and infiltration occur simultaneously. Also sometimes, as in the carbon-silicon system, the rate of product formation is very fast and this results in blocking of the pore channels thus making further infiltration of the preform very difficult. So in order to maintain an interconnected porosity, ways should be found that can retard the rate of reaction (product formation) so that this phenomenon is curbed. If the system is non-wetting, an external pressure is required to force the liquid into the pores. Even if the system is wetting, the external pressure can also be used to accelerate the rate of infiltration and also help the melt to reach the much smaller pores.

The reaction between carbon and silicon to form silicon carbide is mainly thought to be a diffusion process though existing literature presents conflicting interpretations of the mechanism of the reaction. The assessed equilibrium phase diagram of the Si-C system is presented in Fig. 1.18.

Researchers, Olesinski and Abbaschian [167], studied the thermodynamics of the Si-C system to determine the stability of various phases of the Si-C system. They concluded that silicon carbide is a thermodynamically stable compound, with the cubic form (β-SiC) more stable than the hexagonal form (α-SiC) at any temperature below the peritectic point. The heat of formation from the elements is given by: $\Delta H^0_{298} = -(69 \div 73)$ kJ/mol, which means a distinctive exothermal chemical reaction [168].

Studies on the kinetics and the reaction mechanism of the SiC formation from different precursors have been reported and several theories have been put forward. There is a general agreement that the rate controlling step of the reaction is the diffusion of carbon atoms through the newly formed SiC with activation energies of 100÷400 kJ/mol [169].

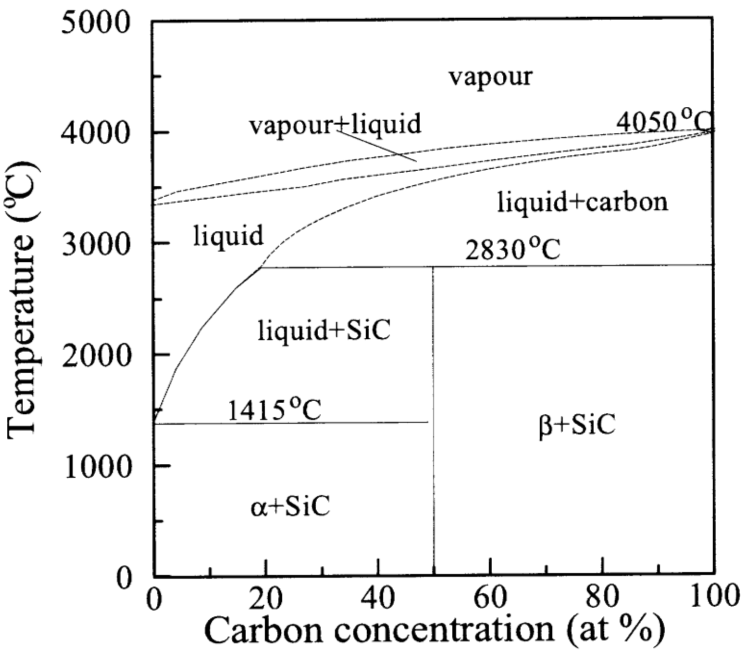

Figure 1.18: Equilibrium phase diagram of the carbon-silicon system [167].

Other suggestions pointed that the vacancy mechanism is responsible for the diffusion of silicon and carbon through β-SiC [170]. Carbon is the faster diffusing component in the lattice of β-SiC due to its smaller atomic size. The lowest energy migration route is believed to be the direct jump to the nearest Si vacancy without the occupation of an intermediate vacant octahedral position. The diffusion constants of carbon and silicon in β-SiC are given in Fig. 1.19.

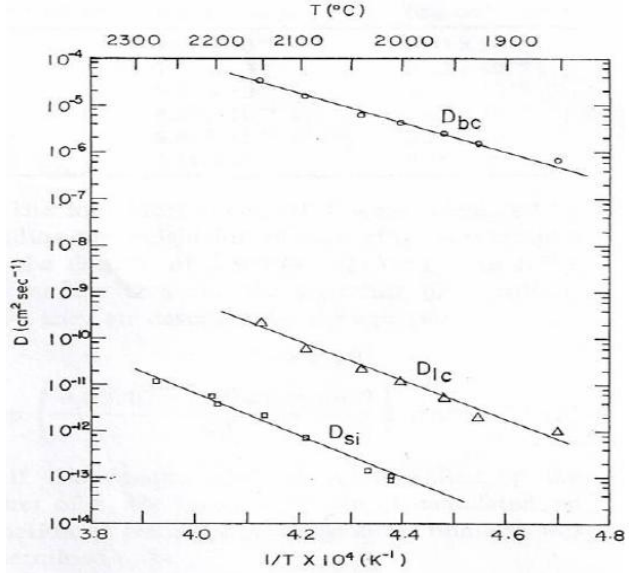

Figure 1.19: Self-diffusion coefficients of ^{14}C lattice diffusion (D_{lc}), ^{14}C grain-boundary diffusion (D_{bc}) and ^{30}Si lattice diffusion (D_{si}), in β-SiC as a function of 1/T [170].

Fitzer and Gadow [168] investigated the reactivity of different carbons with liquid silicon. They found out that the microstructure and porosity of the original carbon determines how the heterogeneous chemical reaction between carbon and liquid silicon takes place. The reaction mechanism involves three stages: a silicon mass transfer by volume diffusion caused by capillary effect, the complete wetting of molten silicon on pure carbon surfaces and the grain boundary and bulk diffusion of silicon through the primarily formed SiC layer. The structure of the SiC layer on the inner and outer surface of the sample determines the effective diffusion coefficient. This further supports the theories that the reaction between carbon and silicon is mainly a diffusion process. However, Hase and Suzuki [171] found no continuous product layer between carbon particles and silicon. They suggested that the reaction product quickly spalled owing to the volume misfit between SiC and carbon leading to an interface-limited reaction directly between silicon and carbon.

Sawyer and Page [172] and Ness and Page [173] also proposed a different reaction mechanism. They proposed that the reaction mechanism is mainly a solution re-precipitation mechanism. The SiC is precipitated from a supersaturated solution of graphite in liquid silicon on to local nucleation sites. The rate of carbon dissolution is accelerated by the heat evolved in the reaction and this allows the reaction to go to completion. The highest dissolution of carbon in silicon is believed to be at the reaction front since the reaction is highly exothermic and the supersaturation is believed to exist in the cooler regions away from the reaction front [174]. The newly formed SiC grows as the β-polytype and nucleates either on the existing grits or less frequently, on the graphite or even homogenously [173]. The finely dispersed β-SiC forms during the local cooling down of the liquid silicon immediately behind the reaction front and thus never experiences sufficient thermal activation to transform to α-SiC. Zhou and Singh [174] supported this solution-precipitation mechanism. They found SiC precipitates in the silicon phase and this was assumed that carbon had dissolved in the liquid phase and got carried away into the silicon phase and finally precipitated as SiC during cooling.

The kinetics of the reaction between carbon and silicon has also been studied. Zhou and Singh [174] studied the reaction kinetics of glass carbon and a pure silicon melt. In their study, they found out that most of the SiC was formed during the early stage of the reaction and the growth rate of the SiC layer decreased in the latter stage of the reaction. A model which can explain the experimentally observed rate law was proposed, in which a negative space charge was assumed to exist in the growing SiC layer. The diffusion of the carbon-ion vacancy through this layer under an electric field is proposed as the rate limiting step for the growth of the SiC layer [174]. A critical analysis of the data of Zhou and Singh [174] would suggest that there is a change in the mechanism after the layer has formed. Assuming such change in the reaction mechanism, there is no necessity for a forth power rate law to describe the data. The time dependence of the growth of the SiC film itself is difficult to determine due to the low growth rate and the relative low time of the experiments.

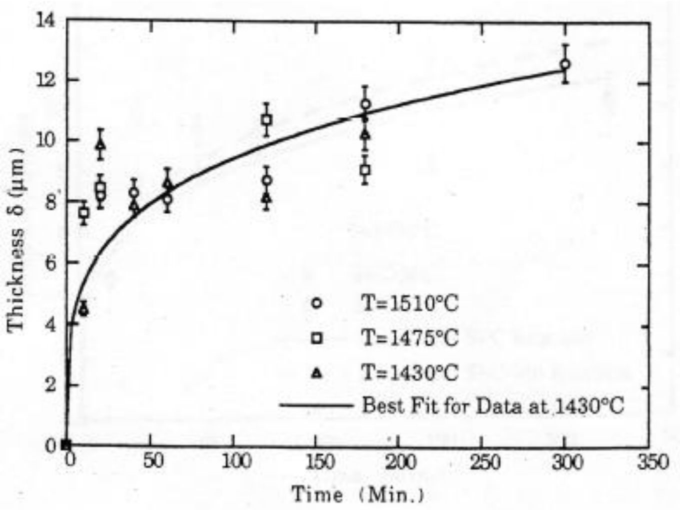

Figure 1.20: Thickness of the SiC layer as a function of the reaction time for Si-C at 1430°C, 1475°C and 1510°C [174].

From Fig. 1.20, it can be observed that an increase in the reaction time gave rise to an increase in the SiC thickness layer. There is a sharp increase in the SiC thickness at the initial stages of the reaction and then it slows down as the reaction progresses.

1.7 References

[1] L. Kaufman and E. V. Clougherty, *Investigation of Boride Compounds for Very High Temperature Applications*, RTD-TRD-N63-4096, Part III, ManLabs Inc., Cambridge, MA, (1966).

[2] E. V. Clougherty, D. Kalish and E. T. Peters, *Research and Development of Refractory Oxidation Resistant Diborides*, AFML-TR-68-190, ManLabs Inc., Cambridge, MA, (1968).

[3] J. J. Gangler, *NASA Research on Refractory Compounds*, High Temp. High Press., 3 487-502 (1971).

[4] E. L. Courtright, H. C. Graham, A. P. Katz and R. J. Kerans, *Ultra High Temperature Assessment Study - Ceramic Matrix Composites*, AFWAL-TR-91-4061, Wright Patterson Air Force Base, Ohio, (1992).

[5] R. A. Cutler, *Engineering Properties of Borides*, In Ceramics and Glasses, Engineering Materials Handbook, vol. 4, ed. S. J. Schneider Jr. ASM International, Materials Park, OH, 787- 803 (1991).

[6] E. P. Simonenko, D. V. Sevast'yanov, N. P. Simonenko, V. G. Sevast'yanov and N. T. Kuznetsov, *Promising Ultra-High-Temperature Ceramic Materials for Aerospace Applications*, Rus. J. Inorg. Chem., 58 [14] 1669-93 (2013).

[7] S. A. Tucker and H. R. Moody, *II. - The Production of Hitherto Unknown Metallic Borides*, J. Chem. Soc., 81 14-7 (1902).

[8] G. V. Samsonov, *Refractory Transition Metal Compounds: High Temperature Cermets*, Academic Press, New York, (1964).

[9] P. Schwarzkopf and R. Kieffer, *Refractory Hard Metals: Borides, Carbides, Nitrides, and Silicides*, New York, MacMillan, (1953).

[10] S. R. Levine, E. J. Opila, M. C. Halbig, J. D. Kiser, M. Singh and J. A. Salem, *Evaluation of Ultra-High Temperature Ceramics for Aeropropulsion Use*, J. Eur. Ceram. Soc., 22 [14-15] 2757-67 (2002).

[11] J. Han, P. Hu, X. Zhang and S. Meng, *Oxidation Behavior of Zirconium Diboride-Silicon Carbide at 1800°C*, Scripta Mater., 57 [9] 825-8 (2007).

[12] W. G. Fahrenholtz, *Thermodynamic Analysis of* Zrb_2*-SiC Oxidation: Formation of a SiC-Depleted Region*, J. Am. Ceram. Soc. 90 [1] 143-148 (2007).

[13] F. Monteverde and A. Bellosi, *Oxidation of* ZrB_2*-Based Ceramics in Dry Air*, J. Electrochem. Soc., 150 [11] B552-9 (2003).

[14] C. Mroz, *Annual Mineral Review; Zirconium Diboride*, Am. Ceram. Soc. Bull., 74 165-6 (1995).

[15] R. Telle, L. S. Sigl and K. Takagi: in 'Handbook of ceramic hard materials', (ed. R. Riedel), Weinheim, Wiley-VCH, 802-945 (2000).

[16] B. Stucker, W. Bradley, P. T. Eubank, S. Norasetthekul and B. Bozkurt: Proc. Symp. on 'Solid freeform fabrication', Austin, TX, USA, SAMPE, Vol. 1, 257-65 (1997).

[17] N. Kaji, H. Skikano and I. Tanaka, Taikabutsu Overseas, 14 39-43 (1992).

[18] J. Sung, D. M. Goedde, G. S. Girolami and J. R. Abelson, *Remote-Plasma Chemical Vapor Deposition of Conformal* ZrB_2 *Films at Low Temperature: A Promising Diffusion Barrier for Ultralarge Scale Integrated Electronics*, J. Appl. Phys., 91 [6] 3904-11 (2002).

[19] Y. Murata, *Cutting tool tips and ceramics containing hafnium nitride and zirconium diboride*, US Patent 3, 487 594 (1970).

[20] Z. J. Jin, M. Zhang, D. M. Guo and R. K. Kang, *Electroforming of Copper/*ZrB_2 *Composite Coating and its Performance as Electro-Discharge Machining Electrodes*, Key Eng. Mater., 291-2 537-42 (2005).

[21] K. Upadhya, J. M. Yang and W. P. Hoffmann, *Materials for Ultrahigh Temperature Structural Applications*, Am. Ceram. Soc. Bull., 76 [12] 51-6 (1997).

[22] F. Monteverde, A. Bellosi and S. Guicciardi, *Processing and Properties of Zirconium Diboride-Based Composites*, J. Europ. Ceram. Soc., 22 [3] 279-88 (2002).

[23] I. M. Low and R. McPherson, *Fabrication of New Zirconium Boride Ceramics*, J. Mat. Sci. Lett., 8 [11] 1281-4 (1989).

[24] P. Kolodziej, J. Salute and D. L. Keese, *First Flight Demonstration of a Sharp Ultra-High Temperature Ceramic Nosetip*, NASA TM-112215, (1997).

[25] D. A. Kontinos, K. Gee and D. K. Prabhu, *Temperature Constraints at the Sharp Leading Edge of a Crew Transfer Vehicle*, AIAA 2001-886 (2001).

[26] A. F. Guillermet and G. Grimvall, *Phase Stability Properties of Transition Metal Diborides*, Am. Inst. Phy. Conf. Proc., 231 423-31 (1991).

[27] W. G. Fahrenholtz, G. E. Hilmas, I. G. Talmy, and J. A. Zaykoski, *Refractory Diborides of Zirconium and Hafnium*, J. Am. Ceram. Soc., 90 [5] 1347-64 (2007).

[28] A. S. Brown, *Hypersonic Designs with a Sharp Edge*, Aerospace Am., 35 [9] 20-1 (1997).

[29] W. C. Tripp, H. H. Davis and H. C. Graham, *Effect of an SiC Addition on the Oxidation of* ZrB_2, Bull. Am. Ceram. Soc., 52 [8] 612-6 (1973).

[30] A. L. Chamberlain, W. G. Fahrenholtz, G. E. Hilmas and D. T. Ellerby, *High-Strength Zirconium Diboride-Based Ceramics*, J. Am. Ceram. Soc., 87 [6] 1170-2 (2004).

[31] F. Monteverde, *Beneficial Effects of an Ultra-Fine α-SiC Incorporation on the Sinterability and Mechanical Properties of ZrB_2*, Appl. Phys. A, 82 [2] 329-37 (2006).

[32] S. S. Hwang, A. L. Vasiliev and N. P. Padture, *Improved Processing and Oxidation-Resistance of ZrB_2 Ultra-High Temperature Ceramics Containing SiC Nanodispersoids*, Mater. Sci. Eng. A, 464 [1-2] 216-24 (2007).

[33] S. Zhu, W. G. Fahrenholtz and G. E. Hilmas, *Influence of Silicon Carbide Particle Size on the Microstructure and Mechanical Properties of Zirconium Diboride-Silicon Carbide Ceramics*, J. Eur. Ceram. Soc., 27 [4] 2077-83 (2007).

[34] A. Rezaie, W. G. Fahrenholtz and G. E. Hilmas, *Effect of Hot-Pressing Time and Temperature on the Microstructure and Mechanical Properties of ZrB_2-SiC*, J. Mater. Sci., 42 [8] 2735-44 (2007).

[35] E. V. Clougherty, R. L. Pober and L. Kaufman, *Synthesis of Oxidation Resistance Metal Diboride Composites*, Trans. TMS AIME, 242 [6] 1077-82 (1968).

[36] D. Sciti, F. Monteverde, S. Guicciardi, G. Pezzotti and A. Bellosi, *Microstructure and Mechanical Properties of ZrB_2-$MoSi_2$ Ceramic Composites Produced by Different Sintering Techniques*, Mater. Sci. Eng. A, 434 [1-2] 303–309 (2006).

[37] A. Bellosi, F. Monteverde and D. Sciti, *Fast Densification of Ultra-High Temperature Ceramics by Spark Plasma Sintering*, Int. J. Appl. Ceram. Technol., 3 [1] 32-40 (2006).

[38] S.-Q. Guo, T. Nishimura, T. Mizuguchi and Y. Kagawa, *Mechanical Properties of Hot-Pressed ZrB_2-$MoSi_2$-SiC Composites*, J. Eur. Ceram. Soc., 28 [9] 1891-8 (2008).

[39] S.-Q. Guo, Y. Kagawa, T. Nishimura and H. Tanaka, *Pressureless-Sintering and Physical Properties of ZrB_2-Based Composites with $ZrSi_2$ Additive*, Scripta Mater., 58 [7] 579-82 (2008).

[40] S.-Q. Guo, Y. Kagawa and T. Nishimura, *Mechanical Behavior of Two-Step Hot-Pressed ZrB_2-Based Composites with $ZrSi_2$*, J. Eur. Ceram. Soc., 29 [4] 787-94 (2009).

[41] P. T. B. Shaffer, *Engineering Properties of Carbides*, in ASTM Engineered Materials Handbook, Vol. 4 - Ceramics and Glasses, S. J. Schneider, technical chairman, 804-11 (1991).

[42] Battelle Columbus Laboratories, *Engineering Property Data on Selected Ceramics*,Vol. 2: Carbides. Metals and Ceramics Information Center, Battelle Columbus Laboratories, Report MCIC-HB-07-Vol. 2 (1979).

[43] S. Hampshire, *Engineering Properties of Nitrides*, in ASTM Engineered Materials Handbook, Vol. 4 - Ceramics and Glasses, S. J. Schneider, technical chairman, 812-20 (1991).

[44] K. E. Spear, *Chemical Bonding in AlB_2-Type Borides*, J. Less-Common Metals, 47 [C] 195-201 (1976).

[45] J. K. Burdett, E. Canadell and G. J. Miller, *Electronic Structure of Transition Metal Borides with the AlB_2 Structure*, J. Am. Chem. Soc., 108 [21] 6561-8 (1986).

[46] M. J. Gasch, D. T. Ellerby and S. M. Johnson, *Ultra High Temperature Ceramic Composites*, Handbook of Ceramic Composites, ed. N. P. Bansal, Kluwer Academic Publishers, (2005).

[47] G. V. Samsonov and I. M. Vinitskii, *Handbook of Refractory Compounds*, Plenum Press, (1980).

[48] A. F. Guillermet and G. Grimvall, *Bonding Properties and Vibrational Entropy of Transition Metal MeB_2(AlB_2) Diborides*, J. Less-Common Metals, 169 [2] 257-81 (1991).

[49] L. B. Pankratz, J. M. Stuve and N. A. Gokcen, *Thermodynamic Data for Mineral Technology*, Bulletin 677, U.S. Bureau of Mines, 98-102 (1984).

[50] F. Monteverde and A. Bellosi, *Development and Characterization of Metal-Diboride-Based Composites Toughened with Ultra-Fine SiC Particulates*, Solid State Sci., 7 [5] 622-30 (2005).

[51] F. Monteverde and A. Bellosi, *Beneficial Effects of AlN as Sintering Aid on Microstructure and Mechanical Properties of Hot-Pressed ZrB_2*, Adv. Eng. Mater., 5 [7] 508-12 (2003).

[52] F. Monteverde and A. Bellosi, *Effect of the Addition of Silicon Nitride on Sintering Behaviour and Microstructure of Zirconium Diboride*, Scripta Mater., 46 [3] 223-8 (2002).

[53] S. Zhang, G. E. Hilmas, and W. G. Fahrenholtz, *Pressureless Densification of Zirconium Diboride with Boron Carbide Additions*, J. Am. Ceram. Soc., 89 [5] 1544-50 (2006).

[54] J. B. Hedrick, *Zirconium and Hafnium*, U.S. Geological Survey Minerals Yearbook, 86.2-86.8, (1999).

[55] M. Pastor, *Metallic Borides: Preparation of Solid Bodies, Sintering Methods and Properties of Solid Bodies*, In Boron and Refractory Borides, ed. V. I. Matkovich. Springer, New York, 457-93 (1977).

[56] G. A. Meeson and A. F. Gorbunow, *Activated Sintering of Zirconium Boride*, Inorg. Mater., 4 267-70 (1968).

[57] M. Kinoshita, S. Kose and Y. Hamano, *Hot-Pressing of Zirconium Diboride-Molybdenum Disilicide Mixtures*, Yogyo-Kyokai-Shi, 78 [2] 32-41 (1970).

[58] S.-Q. Guo, J.-M. Yang, H. Tanaka and Y. Kagawa, *Effect of Thermal Exposure on Strength of ZrB_2-Based Composites with Nano-Sized SiC Particles*, Compos. Sci. Technol., 68 [14] 3033-40 (2008).

[59] D. Kalish and E. V. Clougherty, *Densification Mechanisms in High-Pressure Hot-Pressing of HfB_2*, J. Am. Ceram. Soc., 52 [1] 26-30 (1969).

[60] D. Kalish, E. V. Clougherty and K. Kreder, *Strength, Fracture Mode, and Thermal Stress Resistance of HfB_2 and ZrB_2*, J. Am. Ceram. Soc., 52 [1] 30-6 (1969).

[61] S.-Q. Guo, *Densification of ZrB_2-Based Composites and their Mechanical and Physical Properties: A Review*, J. Eur. Ceram. Soc., 29 [6] 995-1011 (2009).

[62] J. J. Melendez-Martinez, A. Dominguez-Rodriguez, F. Monteverde, C. Melandri and G. De Portu, *Characterization and High Temperature Mechanical Properties of Zirconium Boride-Based Materials,* J. Eur. Ceram. Soc., 22 [14-15] 2543-9 (2002).

[63] F. Monteverde, S. Guicciardi and A. Bellosi, *Advances in Microstructure and Mechanical Properties of Zirconium Diboride Based Ceramics*, Mater. Sci. Eng. A, 346 [1-2] 310-9 (2003).

[64] S.-Q. Guo, Y. Kagawa, T. Nishimura and H. Tanaka, *Elastic Properties of Spark Plasma Sintered (SPSed) ZrB_2–ZrC–SiC Composites*, Ceram. Int., 34 [8] 1811-7 (2008).

[65] F. Monteverde and A. Bellosi, *Efficacy of HfN as Sintering Aid in the Manufacture of Ultra-High-Temperature Metal Diborides-Matrix Ceramics*, J. Mater. Res., 19 [12] 3576-85 (2004).

[66] S. Baik and P. F. Becher, *Effect of Oxygen Contamination on Densification of TiB_2*, J. Am. Ceram. Soc., 70 [8] 527-30 (1987).

[67] T. J. Rockett and W. R. Foster, *Phase Relations in the System Boron Oxidesilica*, J. Am. Ceram. Soc., 48 [2] 75-80 (1965).

[68] Y.-L. Jeng and E. J. Lavernia, *Review: Processing of Molybdenum Disilicide*, J. Mater. Sci., 29 [10] 2557-71 (1994).

[69] R. Rosenkranz and G. Frommeyer, *Microstructures and Properties of the Refractory Compounds $TiSi_2$ and $ZrSi_2$*, Z. Metalkd., 83 [9] 685-9 (1992).

[70] M. Tokida, *Trends in Advanced Spark Plasma Sintering System and Technology*, J. Soc. Powder Technol. Jpn., 30 [11] 790-804 (1993).

[71] M. Nygren and Z. Shen, *On the Preparation of Bio-, Nano- and Structural Ceramics and Composites by Spark Plasma Sintering*, Solid State Sci., 5 [1] 125-31 (2003).

[72] Z. Shen, M. Johnsson, Z. Zhao and M. Nygren, *Spark Plasma Sintering of Alumina*, J. Am. Ceram. Soc., 85 [8] 1921-7 (2002).

[73] K. A. Khor, K. H. Cheng, L. G. Yu and F. Boey, *Thermal Conductivity and Dielectric Constant of Spark Plasma Sintered Aluminum Nitride*, Mater. Sci. Eng. A, 347 [1-2] 300-5 (2003).

[74] F. Guillard, A. Allemand, J. D. Lulewicz and J. Galy, *Densification of SiC by SPS-Effects of Times, Temperature and Pressure*, J. Eur. Ceram. Soc., 27 [7] 2725-28 (2007).

[75] M. Stuer, Z. Zhao, U. Aschauer and P. Bowen, *Transparent Polycrystalline Alumina Using Spark Plasma Sintering: Effect of Mg, Y and La Doping*, J. Eur. Ceram. Soc., 30 [6] 1335-43 (2010).

[76] R. Licheri, R. Orrù, C. Musa, A. M. Locci and G. Cao, *Spark Plasma Sintering of UHTC Powders Obtained by Self-Propagating High-Temperature Synthesis*, J. Mater. Sci., 43 [19] 6406-13 (2008).

[77] A. Bellosi, F. Monteverde, D. D. Fabbriche and C. Melandri, *Microstructure and Properties of ZrB_2-Based Ceramics*, J. Mater. Process. Manuf. Sci., 9 [2] 156-70 (2000).

[78] J. Groza and A. Zavaliangos, *Sintering Activation by External Electrical Field*, Mater. Sci. Eng. A, 287 [2] 171-7 (2000).

[79] J. Groza, M. Garcia and J. A. Schneider, *Surface Effects in Field-Assisted Sintering*, J. Mater. Res., 16 [1] 286-92 (2001).

[80] V. Medri, F. Monteverde, A. Balbo and A. Bellosi, *Comparison of ZrB_2-ZrC-SiC Composites Fabricated by Spark Plasma Sintering and Hot-Pressing*, Adv. Eng. Mater., 7 [3] 159-63 (2005).

[81] S.-Q. Guo, Y. Kagawa, T. Nishimura, D. Chung and J.-M. Yang, *Mechanical and Physical Behavior of Spark Plasma Sintered ZrC–ZrB_2–SiC Multiphase Composites*, J. Eur. Ceram. Soc., 28 [6] 1279-85 (2008).

[82] H. Kaga, E. M. Heian, Z. A. Munir, C. Schmalzried and R. Telle, *Synthesis of Hard Materials by Field Activation: the Synthesis of Solid Solutions and Composites in the TiB_2-WB_2-CrB_2 System*, J. Am. Ceram. Soc., 84 [12] 2764-70 (2001).

[83] A. M. Locci, R. Orru, G. Cao and Z. A. Munir, *Simultaneous Spark Plasma Synthesis and Densification of TiC–TiB_2 Composites*, J. Am. Ceram. Soc., 89 [3] 848-55 (2006).

[84] D. Sciti, L. Silvestroni and A. Bellosi, *Fabrication and Properties of HfB_2-$MoSi_2$ Composites Produced by Hot Pressing and Spark Plasma Sintering*. J. Mater. Res., 21 [6] 1460-66 (2006).

[85] D. Sciti, S. Guicciardi and M. Nygren, *Densification and Mechanical Behavior of HfC and HfB_2 Fabricated by Spark Plasma Sintering*, J. Am. Ceram. Soc., 91 [5] 1433-40 (2008).

[86] A. K. Khanra, L. C. Pathak, S. K. Mishra and M. M. Godkhindi, *Self-Propagating-High-Temperature Synthesis (SHS) of Ultrafine ZrB_2 Powder*, J. Mater. Sci. Lett., 22 [17] 1189-91 (2003).

[87] N. Bertolino, M. Monagheddu, A. Tacca, P. Giuliani, C. Zanotti, F. Maglia and U. A. Tamburini, *Self-Propagating High-Temperature Synthesis of Functionally Graded Materials as Thermal Protection Systems for High-Temperature Applications*, J. Mater. Res., 18 [2] 448-55 (2003).

[88] G.-J. Zhang, Z.-Y. Deng, N. Kondo, J.-F. Yang and T. Ohji, *Reactive Hot Pressing of ZrB_2-SiC Composites*, J. Am. Ceram. Soc., 83 [9] 2330-32 (2000).

[89] W.-W. Wu, G.-J. Zhang, Y.-M. Kan and P.-L. Wang, *Reactive Hot Pressing of ZrB_2-SiC-ZrC Ultra High-Temperature Ceramics at 1800°C*, J. Am. Ceram. Soc., 89 [9] 2967-9 (2006).

[90] J. W. Zimmermann, G. E. Hilmas, W. G. Fahrenholtz, F. Monteverde and A. Bellosi, *Fabrication and Properties of Reactively Hot Pressed ZrB_2-SiC Ceramics*, J. Eur. Ceram. Soc., 27 [7] 2729-36 (2007).

[91] F. Monteverde, *Progress in the Fabrication of Ultra-High-Temperature Ceramics: In Situ Synthesis, Microstructure and Properties of a Reactive Hot-Pressed HfB_2-SiC Composite*, Compos. Sci. Technol., 65 [11-12] 1869-79 (2005).

[92] U. Anselmi-Tamburini, Y. Kodera, M. Gasch, C. Unuvar, Z. A. Munir, M. Ohyanagi and S. M. Johnson, *Synthesis and Characterization of Dense Ultra-High Temperature Thermal Protection Materials Produced by Field Activation Through Spark Plasma Sintering (SPS): 1. Hafnium Diboride*, J. Mater. Sci., 41 [10] 3097-104 (2006).

[93] B. Cech, P. Oliverius and J. Sejbal, *Sintering of Zirconium Boride with Activating Additions*, Powder Metall., 8 [15] 142-51 (1965).

[94] P. S. Kislui and M. A. Kuzenkova, *Regularities of Sintering of Zirconium Diboride-Molybdenum Alloys*, Sov. Powder Metall. Met. Ceram., 5 360-5 (1966).

[95] M.-A. Einarsrud, E. Hagen, G. Pettersen and T. Grande, *Pressureless Sintering of Titanium Diboride with Nickel, Nickel Boride, and Iron Additives*, J. Am. Ceram. Soc., 80 [12] 3013-20 (1997).

[96] D. Sciti, M. Brach and A. Bellosi, *Oxidation Behavior of a Pressureless Sintered ZrB_2-$MoSi_2$ Ceramic Composites*, J. Mater. Res., 20 [4] 922-30 (2005).

[97] D. Sciti, S. Guicciardi, A. Bellosi and G. Pezzotti, *Properties of a Pressureless-Sintered ZrB_2-$MoSi_2$ Ceramic Composite*, J. Am. Ceram. Soc., 89 [7] 2320-2 (2006).

[98] Y. Yan, Z. Huang, S. Dong and D. Jiang, *Pressureless Sintering of High Density ZrB_2-SiC Ceramic Composites*, J. Am. Ceram. Soc., 89 [11] 3589-92 (2006).

[99] S. Zhu, W. G. Fahrenholtz, G. E. Hilmas and S. C. Zhang, *Pressureless Sintering of Zirconium Diboride Using Boron Carbide and Carbon Additions*, J. Am. Ceram. Soc., 90 [11] 3660-63 (2007).

[100] W. G. Fahrenholtz, G. E. Hilmas, S. C. Zhang and S. Zhu, *Pressureless Sintering of Zirconium Diboride: Particle Size and Additive Effects*. J. Am. Ceram. Soc., 91 [5] 1398-404 (2008).

[101] S. Zhu, W. G. Fahrenholtz, G. E. Hilmas and S. C. Zhang, *Pressureless Ssintering of Carbon-Coated Zirconium Diboride Powders*, Mater. Sci. Eng. A, 459 [1-2] 167-71 (2007).

[102] A. L. Chamberlain, W. G. Fahrenholtz and G. E. Hilmas, *Pressureless Sintering of Zirconium Diboride*, J. Am. Ceram. Soc., 89 [2] 450-6 (2006).

[103] M. M. Opeka, I. G. Talmy, E. J. Wuchina, J. A. Zaykoski and S. J. Causey, *Mechanical, Thermal and Oxidation Properties of Refractory Hafnium and Zirconium Compounds*, J. Europ. Ceram. Soc., 19 [13-14] 2405-14 (1999).

[104] E. V. Clougherty, K. E. Wilkes and R. P. Tye, *Research and Development of Refractory Oxidation Resistant Diborides*, Part II, Vol. V: Thermal, Physical, Electrical and Optical Properties, AFML-TR-68-190, ManLabs lnc., Cambridge, MA, (1969).

[105] R. G. Munro, *Material Properties of a Sintered α-SiC*, J. Physical and Chemical Reference Data, 26 [5] 1195-203 (1997).

[106] D. E. Wiley, W. R. Manning and O. Hunter Jr., *Elastic Properties of Polycrystalline TiB_2, ZrB_2 and HfB_2 From Room Temperature to 1300 K*, J. Less-Common Met., 18 [2] 149-57 (1969).

[107] H. E. Exner, *Physical and Chemical Nature of Cemented Carbides*, Int. Metall. Rev., 24 [4] 149-73 (1979).

[108] W. H. Rhodes, E. V. Clougherty and D. Kalish, *Research and Development of Refractory Oxidation Resistant Diborides*, Part II, Vol. IV: Mechanical Properties, AFML-TR-68-190, ManLabs lnc., Cambridge, MA, (1970).

[109] R. Pampuch, *Ceramic Materials: An Introduction to Their Properties*, Elsevier Scientific Publishers/PWN-Polish Scientific Publishers, New York/Warsaw, Poland, 172-90 (1976).

[110] S.-Q. Guo, N. Hirosaki, Y. Yamamoto, T. Nishimura and M. Mitomo, *Hot-Press Sintering Silicon Nitride with Lu_2O_3 Addition: Elastic Moduli and Fracture Toughness*, J. Eur. Ceram. Soc., 23 [3] 537-45 (2003).

[111] R. W. Rice, *Particle Effects on Elastic Properties, Crack Propagation, and Fracture Toughness of Ceramic Composites at ∼ 22°C*, Mechanical Properties of Ceramics and Composites. Marcel Dekker, Inc., New York, 457 (2000).

[112] E. A. Dean and J. A. Lopez, *Empirical Dependence of Elastic Moduli on Porosity for Ceramic Materials*, J. Am. Ceram. Soc., 66 [5] 366-70 (1983).

[113] C. W. Bert, *Prediction of Elastic Moduli of Solid with Oriented Porosity*, J. Mater. Sci., 20 [6] 2220-4 (1985).

[114] H. Jeong and D. K. Hsu, *Quantitative Estimation of Material Properties of Porous Ceramics by Means of Composite Micromechanics and Ultrasonic Velocity*, NDT Int., 29 [2] 95-101 (1996).

[115] S.-Q. Guo, N. Hirosaki, Y. Yamamoto, T. Nishimura and M. Mitomo, *Improvement of High-Temperature Strength of Hot-Pressed Sintering Silicon Nitride with* Lu_2O_3 *Addition*, Scripta Mater., 45 [7] 867-74 (2001).

[116] L. Kaufman, E. V. Clougherty and J. B. Berkowitz-Mattuck, *Oxidation Characteristics of Hafnium and Zirconium Diboride*, Trans. TMS-AIME, 239 458-66 (1967).

[117] M. W. Chase Jr, *NIST-JANAF Thermochemical Tables*, 4th edn, Woodbury, New York, American Chemical Society and the American Institute of Physics, (1998).

[118] FactSage 6 1, Thermfact and GTT-Technologies, Montreal, QC, Canada, (2009).

[119] J. B. Berkowitz-Mattuck, J. Electrochem. Soc., 113 908-14 (1966).

[120] H. C. Graham, H. H. Davis, I. A. Kvernes and W. C. Tripp, *Ceramics in Severe Environments*, ed. W. W. Kriegel and H. Palmour III, New York, Plenum Press, 35-48 (1971).

[121] T. A. Parthasarathy, R. A. Rapp, M. Opeka and R. J. Kerans, *A Model for the Oxidation of* ZrB_2*,* HfB_2 *and* TiB_2, Acta Mater., 55 [17] 5999-6010 (2007).

[122] T. A. Parthasarathy, R. A. Rapp, M. Opeka and R. J. Kerans, *A Model for Transitions in Oxidation Regimes of* ZrB_2, Mater. Sci. Forum, 595-8 PART 2 823-32 (2008).

[123] T. A. Parthasarathy, R. A. Rapp, M. Opeka and R. J. Kerans, *Effects of Phase Change and Oxygen Permeability in Oxide Scales on Oxidation Kinetics of* ZrB_2 *and* HfB_2, J. Am. Ceram. Soc., 92 [5] 1079-86 (2009).

[124] W. G. Fahrenholtz and G. E. Hilmas, *Oxidation of Ultra-High Temperature Transition Metal Diboride Cceramics*, Intern. Mater. Rev., 57 [1] 61-72 (2012).

[125] A. K. Kuriakose and J. L. Margrave, J. Electrochem. Soc., 111 827-31 (1966).

[126] C. B. Bargeron, R. C. Benson, R. W. Newman, A. N. Jette and T. E. Phillips, *Oxidation Mechanisms of Hafnium Carbide and Hafnium Diboride in the Temperature Range 1400 to 2100°C*, John Hopkins APL Technical Digest (Applied Physics Laboratory), 14 [1] 29-36 (1993).

[127] W. C. Tripp and H. C. Graham, Solid State Sci., 118 1195-9 (1971).

[128] R. J. Irving and I. G. Worsley, *The Oxidation of Titanium Diboride and Zirconium Diboride at High Temperatures*, J. Less Common Met., 16 [2] 103-12 (1968).

[129] M. M. Opeka, I. G. Talmy and J. A. Zaykoski, *Oxidation-Based Materials Selection for 2000°C + Hypersonic Aerosurfaces: Theoretical Considerations and Historical Experience*, J. Mater. Sci., 39 [19] 5887-904 (2004).

[130] W. G. Fahrenholtz, *The* ZrB_2 *Volatility Diagram*, J. Am. Ceram. Soc., 88 [12] 3509-12 (2005).

[131] S. C. Zhang, G. E. Hilmas and W. G. Fahrenholtz, *Improved Oxidation Resistance of Zirconium Diboride by Tungsten Carbide Additions*, J. Am. Ceram. Soc., 91 [11] 3530-5 (2008).

[132] M. Gasch, D. Ellerby, E. Irby, S. Beckman, M. Gusman and S. Johnson, *Processing, Properties and Arc Jet Oxidation of Hafnium Diboride/Silicon Carbide Ultra High Temperature Ceramics*, J. Mater. Sci., 39 [19] 5925-37 (2004).

[133] F. Monteverde, R. Savino, M. De Stefano Fumo and A. Di Maso, *Plasma Wind Tunnel Testing of Ultra-High Temperature* ZrB_2*-SiC Composites Under Hypersonic Re-Entry Conditions*, J. Eur. Ceram. Soc., 30 [11] 2313-21 (2010).

[134] A. Paul, D. D. Jayaseelan, S. Venugopal, E. Zapata-Solvas, J. Binner, B. Vaidhyanathan, A. Heaton, P. Brown and W. E. Lee, *UHTC Composites for Hypersonic Applications*, Am. Ceram. Soc. Bull., 91 [1] 22-29B (2011).

[135] J. Marschall and D. G. Fletcher, *High-Enthalpy Test Environments, Flow Modeling and In Situ Diagnostics for Characterizing Ultra-High Temperature Ceramics*, J. Eur. Ceram. Soc., 30 [11] 2323-36 (2010).

[136] R. Perkins, L. Kaufman and H. Nesor, *Stability Characterization of Refractory Materials Under Velocity Atmospheric Flight Conditions*, Experimental Results of High Velocity Cold Gas/Hot Wall Test, Part III, Vol. II, AFML-TR-68-84, ManLabs Inc., Cambridge, MA, (1969).

[137] L. Kaufman and H. Nesor, *Stability Characterization of Refractory Materials Under High Velocity Atmospheric Flight Conditions*, Part II, Vol. II, AFML-TR-69-84, ManLabs Inc., Cambridge, MA, (1969).

[138] E. V. Clougherty, E. T. Peters and D. Kalish, *Diboride Materials, Candidates for Aerospace Applications*, Proc. 15th SAMPE Symp. on ‘Materials and processes for the 1970s’, Los Angeles, CA, USA, SAMPE, 297-308 (1969).

[139] E. J. Opila and M. C. Halbig, *Oxidation of* ZrB_2*-SiC*, Ceram. Eng. Sci. Proc., 22 [3] 221-8 (2001).

[140] S. Gangireddy, S. N. Karlsdottir, S. J. Norton, J. C. Tucker and J. W. Halloran, *In Situ Microscopy Observation of Liquid Flow, Zirconia Growth, and CO Bubble Formation during High Temperature Oxidation of Zirconium Diboride-Silicon Carbide*, J. Eur. Ceram. Soc., 30 [11] 2365-74 (2010).

[141] S. N. Karlsdottir and J. W. Halloran, *Rapid Oxidation Characterization of Ultra-High Temperature Ceramics*, J. Am. Ceram. Soc., 90 [10] 3233-8 (2007).

[142] S. N. Karlsdottir, J. W. Halloran and C. E. Henderson, *Convection Patterns in Liquid Oxide Films on* ZrB_2*-SiC Composites Oxidized at a High Temperature*, J. Am. Ceram. Soc., 90 [9] 2863-7 (2007).

[143] S. N. Karlsdottir, J. W. Halloran and A. N. Grundy, *Zirconia Transport by Liquid Convection during Oxidation of Zirconium Diboride-Silicon Carbide*, J. Am. Ceram. Soc., 91 [1] 3652-8 (2008).

[144] O. N. Grigoriev, B. A. Galanov, V. A. Lavrenko, A. D. Panasyuk, S. M. Ivanov, A. V. Koroteev and K. G. Nickel, *Oxidation of* ZrB_2*-SiC-*$ZrSi_2$ *Ceramics in Oxygen*, J. Eur. Ceram. Soc., 30 [11] 2397-405 (2010).

[145] C. M. Carney, P. Mogilvesky and T. A. Parthasarathy, *Oxidation Behavior of Zirconium Diboride Silicon Carbide Produced by the Spark Plasma Sintering Method*, J. Am. Ceram. Soc., 92 [9] 2046-52 (2009).

[146] F. Monteverde, *The Thermal Stability in Air of Hot-Pressed Diboride Matrix Composites for uses at Ultra-High Temperatures*, Corros. Sci., 47 [8] 2020-33 (2005).

[147] D. R. Uhlmann and N. J. Kreidl, *Glass: Science and Technology*, vol. 3: Viscosity and Relaxation, Academic Press, New York, 412 (1986).

[148] I. G. Talmy, J. A. Zaykoski, M. M. Opeka and S. Dallek, *High Temperature Corrosion and Materials Chemistry III*, 144-58 (2001).

[149] E. Opila, S. Levine and J. Lorincz, *Oxidation of* ZrB_2*- and* HfB_2*-Based Ultra-High Temperature Ceramics: Effect of Ta Additions*, J. Mater. Sci., 39 [19] 5969-77 (2004).

[150] X. Zhang, X. Li, J. Han, W. Han and C. Hong, *Effects of* Y_2O_3 *on Microstructure and Mechanical Properties of* ZrB_2*-SiC Ceramics*, J. Alloys Compd., 465 [1-2] 506-11 (2008).

[151] A. Spring, W.-M. Guo, G.-J. Zhang, P.-L. Wang and V. D. Krstic, *Fabrication and Characterization of* ZrB_2*-Based Ceramic Using Synthesized* ZrB_2*-*LaB_6 *Powder*, J. Am. Ceram. Soc., 91 [8] 2763-5 (2008).

[152] I. G. Talmy, J. A. Zaykoski, M. M. Opeka and A. H. Smith, *Properties of Ceramics in the System* ZrB_2*-*Ta_5Si_3, J. Mater. Res., 21 [10] 2593-9 (2006).

[153] D. Sciti, L. Silvestroni, G. Celotti, C. Melandri and S. Guicciardi, *Sintering and Mechanical Properties of* ZrB_2*-*$TaSi_2$ *and* HfB_2*-*$TaSi_2$ *Ceramic Composites*, J. Am. Ceram. Soc., 91 [10] 3285-91 (2008).

[154] J. C. A. Bronson and J. Chessa, *An Evaluation of Vaporizing Rates of* SiO_2 *and* TiO_2 *as Protective Coatings for Ultrahigh Temperature Ceramic Composites*, J. Am. Ceram. Soc., 91 [5] 1448-52 (2008).

[155] W. Guo, J. Vleugels, G. Zhang, P. Wang and O. Van der Biest, *Effects of* Re_2O_3 *(Re = La, Nd, Y and Yb) Addition in Hot-Pressed* ZrB_2*-SiC Ceramics*, J. Eur. Ceram. Soc., 29 [14] 3063-8 (2009).

[156] D. D. Jayaseelan: unpublished research, Imperial College London, 2010.

[157] S. C. Zhang, W. G. Fahrenholtz and G. E. Hilmas, *Oxidation of* ZrB_2 *and* ZrB_2*-SiC Ceramics with Tungsten Additions*, ECS Trans., 16 [44] 137-45 (2009).

[158] S. K. Woo, C. H. Kim and E. S. Kang, *Fabrication and Microstructural Evaluation of* ZrB_2*/ZrC/Zr Composites by Liquid Infiltration*, J. Mat. Sci., 29 [20] 5309-15 (1994).

[159] R. German, *Sintering Theory and Practice*, John Wiley and Sons Inc., New York, 385-9 (1996).

[160] M. N. Rahaman, *Ceramic Processing and Sintering*, Marcel Dekker Inc., New York, 526-30 (1995).

[161] L. R. Radovic, P. M. Walker and P. A. Thrower, *Chemistry and Physics of Carbon: A Series of Advances*, Marcel Dekker Inc., New York, 149-61 (1965).

[162] M. N. Rahaman, *Ceramic Processing and Sintering*, 2nd Edition, Marcel Dekker Inc., New York, 15-7 (2003).

[163] J. Narciso, E. Louis and C. Garcia-Cordovilla, *Pressure Infiltration in a Reactive System: Packed SiC Particulates Infiltrated by Pure Silver with Dissolved Oxygen*, Acta Mater., 45 [12] 5111-8 (1997).

[164] K. Mlungwane, *The Development of a Diamond-Silicon Carbide Composite*, PhD thesis, University of the Witwatersrand, South Africa, (2008).

[165] W. B. Hillig, *Making Ceramic Composites by Melt Infiltration*, Am. Ceram. Bull., 73 [4] 56-62 (1994).

[166] L. Hozer, J.-R. Lee and Y.-M. Chiang, *Reaction-Infiltrated, Net-Shape SiC Composites*, Mater. Sci. Eng., 195 [C] 131-43 (1995).

[167] R. W. Olesinski and G. J. Abbaschian, *The C-Si (Carbon-Silicon) system*, Bulletin of Alloy Phase Diagrams, 5 [5] 486-9 (1984).

[168] E. Fitzer and R. Gadow, *Investigations of the Reactivity of Different Carbons with Liquid Silicon*, Proc. Of International Symposium on Ceramic Components for Engine, Japan, S. Somiya, 561-72 (1983).

[169] C. Pantea, G. A. Voronin, T. W. Zerda, J. Zhang, L. Wang, Y. Wang, T. Uchida and Y. Zhao, *Kinetics of SiC Formation during High P-T Reaction between Diamond and Silicon*, Diamond & Related Materials, 14 [10] 1611-5 (2005).

[170] M. H. Hon, R. F. Davis and D. E. Newbury, *Self-Diffusion of* ^{30}Si *in Polycrystalline* β*-SiC*, J. Mater. Sci., 15 [8] 2073-80 (1980).

[171] T. Hase, H. Suzuki and T. Iseki, *Rise in Temperature of SiC Pellet Involving Reaction Sintering*, J. Nucl. Mater., 59 [1] 42-8 (1976).

[172] G. R. Sawyer and T. F. Page, *Microstructural Characterization of "REFEL" (Reaction-Bonded) Silicon Carbides*, J. Mater. Sci. I, 13 [4] 885-904 (1978).

[173] J. N. Ness and T. F. Page, *Microstructural Evolution in Reaction-Bonded Silicon Carbide*, J. Mate. Sci., 21 [4] 1377-97 (1986).

[174] H. Zhou and R. N. Singh, *Kinetics Model for the Growth of Silicon Carbide by the Reaction of Liquid Silicon with Carbon*, J. Am. Ceram. Soc., 78 [9] 2456-62 (1995).

2. Si-SiC-ZrB_2 ceramics by silicon reactive infiltration

2.1 Introduction

Molten silicon reactive infiltration is a manufacturing technique in which a carbon bound porous body, usually called “preform”, is infiltrated with silicon in the liquid or vapor phase which, through an *in situ* chemical reaction, converts into silicon carbide. Si-SiC ceramics were first obtained by Hillig et al. [1] by infiltrating carbonaceous material with molten Si in vacuum (10^{-2} mbar) at temperatures ranging from 1450°C and 1600°C.

The related chemical reaction [2] is:

$$Si_{liquid} + C_{solid} = SiC_{solid}\ [\Delta H = -73\ kJ\ mol^{-1}]\ (2.1)$$

At these temperatures molten Si first infiltrates the porous carbon body by capillarity then reacts with it. In Ceramic Matrix Composite (CMC) manufacturing, this process is usually known as Melt Infiltration (MI) or Liquid Silicon Infiltration (LSI) [3].

Si-SiC CMC, are well known for their good thermo-mechanical properties [3] and are one of the few CMC “mass products” (e.g. ceramic brakes, furnace parts) on the market. The “price to pay” is for the presence of unreacted silicon (5÷15 vol.%) percolated into the structure. Indeed, in order to allow molten Si to fully infiltrate the preform in reasonable time, the volume of its porosity must be higher than the volume of silicon necessary for the stoichiometric reaction with carbon [4]. Si-SiC are fully dense materials and thus are oxidation resistant, but their use is limited by their working temperatures [5, 6].

For applications at higher temperatures other ceramics, usually known as ultra high temperature ceramics (UHTCs), are used including the transition metal diborides of group IV [7]. ZrB_2 and HfB_2 have been widely studied for their high melting points, hardness, chemical and thermal stabilities [8]. Zirconium diboride can be of great interest in some applications (e.g. aerospace) not only because of its lower density with respect to hafnium diboride. ZrB_2 powders have been densified into compact bodies by hot pressing, pressureless sintering, reactive routes and spark plasma sintering [9, 10]. In general these processes involve the use of expensive equipment, because of the processing conditions, and present limitations in product shaping. ZrB_2 has also been processed with additives to tailor its properties; among these, silicon carbide is one of the most widely employed [9, 10]. The flexural strength and thermal conductivity of ZrB_2 ceramics can be increased by adding SiC particles [10, 11]. ZrB_2-SiC ceramics can maintain the “protective” passive oxidation regime over a wide range of temperatures. Adding SiC (up to 30 vol.%) to ZrB_2 not only extends the oxidation temperature range, thanks to the protective behavior of the formed mixed oxide scale [12], but it also allows the ceramic to rapidly regain its protective behavior if scale detaches during excessive temperature exposure [10]. Peng et al. [13] showed that higher concentrations of SiC resulted in thinner glassy surface layers, with lower concentrations of embedded zirconia, and thinner zirconium oxide under layers which could be beneficial or detrimental, depending on the application.

There are few works in the literature which try to produce ZrB_2-SiC based ceramics with alternative routes and they are mainly targeted at producing ceramic matrices for CMCs [14, 15].

To the authors knowledge, literature reports two studies that explore “mild processes” in order to obtain dense Si-SiC-ZrB_2 composites at relatively a low temperature (1500°C) and under pressureless conditions. Blum et al., using molten silicon reactive infiltration [16], developed thick UHTC protective coatings on the top of lightweight C-SiC, SiC-SiC and C-C fiber reinforced ceramics. Zhou et al. produced coatings on C/C composites by vapor silicon infiltration [17].

In this chapter a methodology to produce Si-SiC-ZrB_2 bulk ceramics, taking advantage of the reactive infiltration technique, is proposed. Preforms with different contents of SiC and ZrB_2 were compacted with phenolic resin, pyrolysed and finally infiltrated with molten silicon at temperature above its melting point. The process was intentionally kept as simple as possible in order to maximize its cost efficiency.

Following the historical path of Si-SiC ceramics our long-term goal, starting from this work, is to develop Si-SiC-ZrB_2 ceramic matrix composites by silicon reactive infiltration.

2.2 Experimental procedure

In order to study how the SiC/ZrB_2 volume ratios affect composite manufacturing steps and the resulting microstructure, three different constituent compositions were prepared for this study. The compounds were compacted, pyrolysed in an inert atmosphere, and further infiltrated in vacuum with molten silicon.

2.2.1 Materials

The ceramic powders employed in this work were:

- α-Silicon carbide (Grade UF15 Stark Ag, D) with an average particle size d50 of 0.55 μm by Laser Diffraction and a specific area of 14÷16 m^2/g.
- Zirconium diboride (grade A Stark Ag D) average particle size d50 of 0.3÷5.0 μm by Laser Diffraction.

The powders were pre-mixed to obtain a bimodal particle size distribution [11].

To produce the green bodies, a micronized (~ 64 μm diameter) phenolic novolac powder (Hexion, USA) was mixed with the powders.

Samples were mixed maintaining a constant ratio between the solid charge (powders) and the plastic binder (phenolic resin). For the solid charge, three SiC-ZrB_2 powder mixtures were prepared (Tab. 2.I). Pyrolysed samples presented a similar porosity volume because the ratio of ceramic powders and phenolic resin was kept equal. A volume of around 50% of phenolic resin allowed to the compacted enough green and to the self-standing pyrolysed porous body with a sufficient amount of glassy carbon [18, 19] to be prepared.

Sample	**Solid content (vol.%)**				**Binder (vol.%)**
	51.44				48.56
	SiC (vol.%)		**ZrB_2 (vol.%)**		**Phenolic resin (vol.%)**
	On solid content	**On total**	**On solid content**	**On total**	
S100	100.00	51.44	0.00	0.00	48.56
S50Z50	50.00	25.72	50.00	25.72	48.56
S25Z75	25.00	12.86	75.00	38.58	48.56

Table 2.I: SiC ($\rho = 3.21\ g/cm^3$), ZrB_2 ($\rho = 6.10\ g/cm^3$) and phenolic resin ratios for the produced samples.

2.2.2 Green forming

The powders and phenolic resin were first dried separately in a vacuum oven for 30 min at 40°C and 50 mbar residual pressure. First the solid charge was dry mixed for 30 min by slow ball milling in a sealed container, then milling was continued for a further 30 min with phenolic powder. The compound was immediately hot pressed with a uniaxial press for 150 s at 180°C and at a pressure of 56 MPa. In plane dimensions the die and thus the sample was 90 x 40 mm^2. The amount of powder put into the die was calculated in order to produce green preforms of 4÷5 mm thick.

This first set of samples was over packed to be successfully infiltrated with Si. After pyrolysis, silicon was not able to infiltrate these bodies even for long dwelling times. In a second set, samples were then pressed under the same conditions with the exception of the temperature, which was lowered to 60°C. At this temperature phenolic resin becomes more plastic than liquid. This allowed the compaction of green bodies which, after pyrolysis, were porous enough to be fully silicon infiltrated.

2.2.3 Pyrolysis

Green samples were pyrolysed in an electrical furnace inside a steel retort under inert atmosphere. During pyrolysis argon was injected into the retort at 300 SCCM. The heat ramp is reported in table 2.II.

After pyrolysis, samples were then measured, weighted and new volume fractions calculated (Tab. 2.III). The plain phenolic resin carbon yield was 70% while the other powders were unaffected by this thermal treatment. An overall volumetric shrinking was similar for all the samples (5÷7%). The apparent density was then calculated dividing the new mass by the new volume. These values were then used to calculate samples porosity.

It is worth noting that the bodies did not crumble during pyrolysis, keeping high mechanical resistance after this processing step.

Temperature [°C]	**Temperature rate [°C/h]**	**Ramp Time [h]**	**Total Time [h]**
21÷500	40	12	12
500÷1000	60	8	20
1000	dwell	1	21
1000÷21	Power OFF	~ 24	~ 45

Table 2.II: Pyrolysis heat ramp.

Sample	**ZrB_2 (vol.%)**	**SiC (vol.%)**	**Res. carbon (vol.%)**	**Porosity (vol.%)**
S100	0.0	38.3	15.0	46.7
S50Z50	18.8	19.2	15.9	46.3
S25Z75	31.6	10.6	19.4	38.2

Table 2.III: Constituent materials calculated volume fractions after pyrolysis.

2.2.4 Silicon reactive infiltration

After pyrolysis, samples were placed on a boron nitride painted graphite plate. Carbon wicks were placed between the samples and the plate, to drain excess molten silicon. Silicon flakes were placed onto the samples. The amount of silicon was much higher than needed to react with phenolic derived carbon and to infiltrate the remaining porosity. However, based on our experience, this is necessary to fully infiltrate the preforms. Silicon infiltration was performed at 1500°C with a 10^{-2} mbar residual pressure. The furnace was quickly brought to process temperature and held at that temperature for 2h. The excess silicon reacted with the wicks or remained outside the sample as per Fig. 2.1.

2.2.5 Machining

Sample plates (Fig. 2.1) were first ground with a diamond mill on the outer surfaces, their thickness was consequently reduced in order to be sure to have a genuine Si-SiC-ZrB_2 system on the outer surface. The samples were then cut with a diamond saw into several pieces for characterization.

2.2.6 High temperature oxidation

In order to compare oxidized Si-SiC-ZrB_2 with other works [11, 16, 17, 20], specimens were oxidized in a resistance heated tubular furnace at atmospheric pressure. They were placed in an alumina boat which was then positioned at the centre of an alumina tube. The furnace was brought to 1500°C with an heating rate of 10°C/min and held at that temperature for 2h. A dry air flow of 200 SCCM was maintained in the furnace during the tests.

2.2.7 Characterisation

Samples were characterized by several techniques.

Vickers micro-hardness measurements were carried out with a micro-durometer (Leitz Wetzlar D). Microstructure evaluations on both oxidized and non-oxidized samples were performed with a Field Emission Scanning Electron Microscope (FESEM Zeiss Supra 25 D). Phase analysis was performed, during micrographs acquisition, with a Scandium 5.0 Soft Imaging System GmbH. XRD data were collected with a Philips PW3830 X-ray generator system.

2.3 Results and discussion

The following are the results of an initial characterization study aiming at evaluating Si-SiC-ZrB_2 properties and comparing them with a Si-SiC (S100) compound produced with the same methodology and with literature data. Si-SiC-ZrB_2 oxidation behavior was compared with similar systems adopted as protective coatings [16, 17] and with ZrB_2-SiC [12, 21, 22].

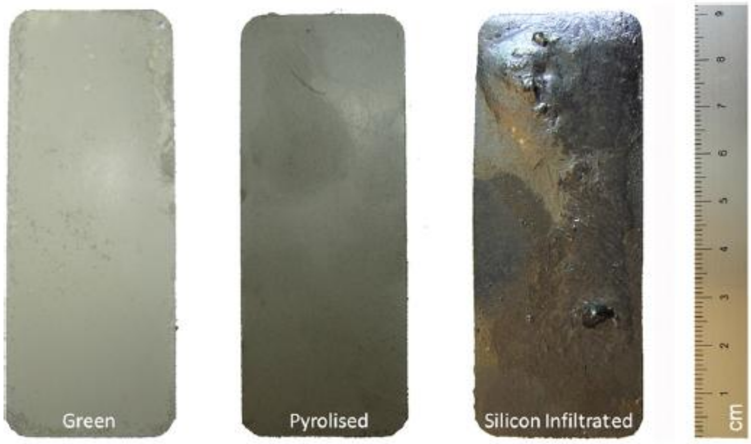

Figure 2.1: Samples during processing steps.

2.3.1 Microstructure

Sample fracture surfaces after pyrolysis were analyzed by SEM. Well dispersed ZrB_2 powder is clearly visible as well as residual carbon around the big pores (Fig. 2.2(a)). Much finer SiC powders, in an agglomerate state (Fig. 2.2(b)) are present, while they are hardly discernible inside the pyrolysed carbon. Samples show a twofold pore size: bigger pores (Fig. 2.2(c)) correspond to the volume formerly occupied by the phenolic powders, smaller pores to the intra particle porosity. It was this bimodal porosity which allowed the silicon infiltration of rather thick (4÷5 mm) samples. During the pyrolysis step the phenolic decomposed byproducts filled the intra particle porosity, keeping the ceramic body compact.

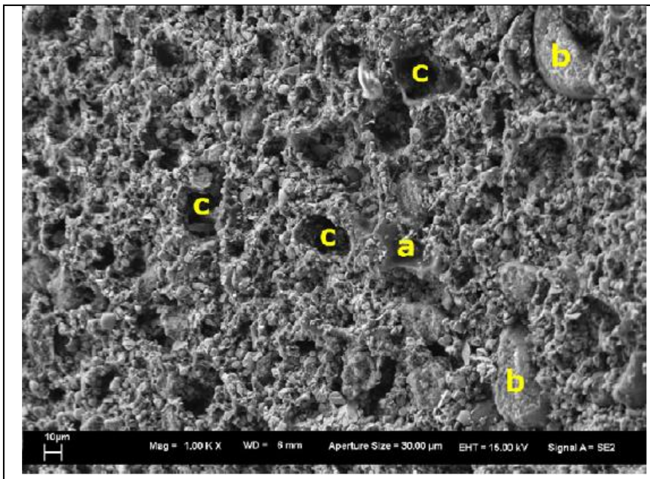	Figure 2.2: S25Z75 sample after pyrolysis (fracture surface). Beside the dispersed ZrB_2 which is visible throughout the fracture surface, the micrograph shows (magnification: 1000X, voltage: 15 kV, working distance: 6 mm, aperture size: 30 µm): (a) glassy carbon, (b) SiC powders agglomerates and (c) big pores.

The patterns in Fig. 2.3 show the crystalline phases detected by the instrument in the Si infiltrated samples. As expected, in S100 both silicon and silicon carbide are present. S50Z50 and S25Z75 samples show three crystal phases, namely: silicon, silicon carbide and zirconium diboride. Their presence is confirmed by micro hardness measurements whose data are reported in table 2.IV. Average results are lower than ZrB_2-SiC systems [23, 24], due to the presence of silicon, while the hardness of each phase is in good agreement with literature data [25].

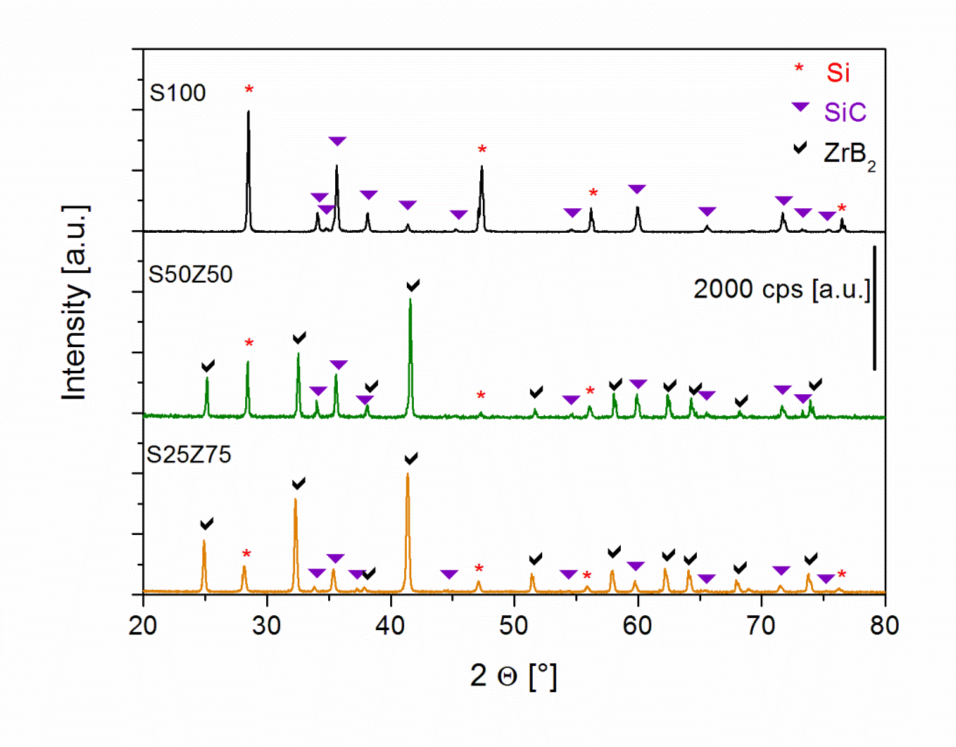

Figure 2.3: XRD patterns of S100, S50Z50 and S25Z75 sample, respectively.

Fig. 2.4 shows the microstructures of S100, S50Z50 and S25Z75 samples after reactive silicon infiltration. Micrographs confirm the tendency of the SiC powders to agglomerate, due to the powder size and the fabrication method. Agglomeration is the cause of the small size pores clearly visible in Fig. 2.4 (a and c).

The micrographs were taken in back-scattered electrons (BSE) mode to enhance the contrast between each phase. In Fig. 2.4(a) two phases with different gray tones are distinguishable, while in Fig. 2.4 (b and c) a third white phase appears. An Energy-dispersive X-Ray spectroscopy (EDS or EDX) analysis on these three phases revealed that the light gray zones are made of Si, the dark gray zones of SiC and the white grains of ZrB_2. A further confirmation of the phases present in the samples comes from the elemental mapping reported in Fig. 2.5 for the S25Z75 sample. Furthermore, the interfaces between the different phases, especially for ZrB_2 compared with the rest of the matrix, are well defined.

Sample	Multiphase indentations		Single phase indentations		
	Average value [GPa]	SD [GPa]	Si [GPa]	SiC [GPa]	ZrB_2 [GPa]
S100	16.2	3.2	9.9	24.0	-
S50Z50	17.6	0.8	9.5	26.1	15.6
S25Z75	14.2	2.4	9.3	24.2	14.0

Table 2.IV: Vickers micro-hardness (load 300 g).

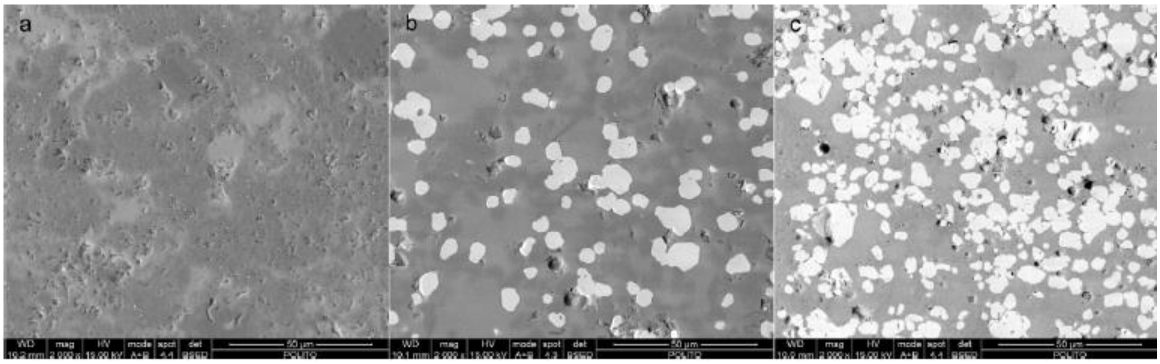

Figure 2.4: SEM images of S100 (a), S50Z50 (b) and S25Z75 (c) obtained with back scattered electrons.

XRD patterns in Fig. 2.3 and the micrographs in Fig. 2.4 (b and c) also show that, during molten infiltration, silicon did not react with ZrB_2 although it formed SiC with the polymer derived carbon.

Silicon infiltrated the porous preforms regardless what SiC to ZrB_2 amounts was into the solid charge. Phenolic derived carbon was the real “neck bottle” in terms of wetting since it presents poor wetting properties before reacting with silicon and forming SiC. When SiC is formed, all Si contact angles, measured on bulk specimens, are quite similar (Tab. 2.V). There are no data available on silicon wetting onto ZrB_2. The suggestion [26] of assuming a wetting behavior similar to TiB_2 for ZrB_2 (Tab. 2.V) was carried out. This hypothesis was confirmed by the weight gains during reactive infiltration and by the morphology analysis in Fig. 2.4 (b and c) in which it is evident that silicon wrapped the ZrB_2 particles. Infiltration was somehow hindered by SiC powder agglomeration (Fig. 2.4 (a and c)) since intra particle gaps were smaller inside the agglomerates.

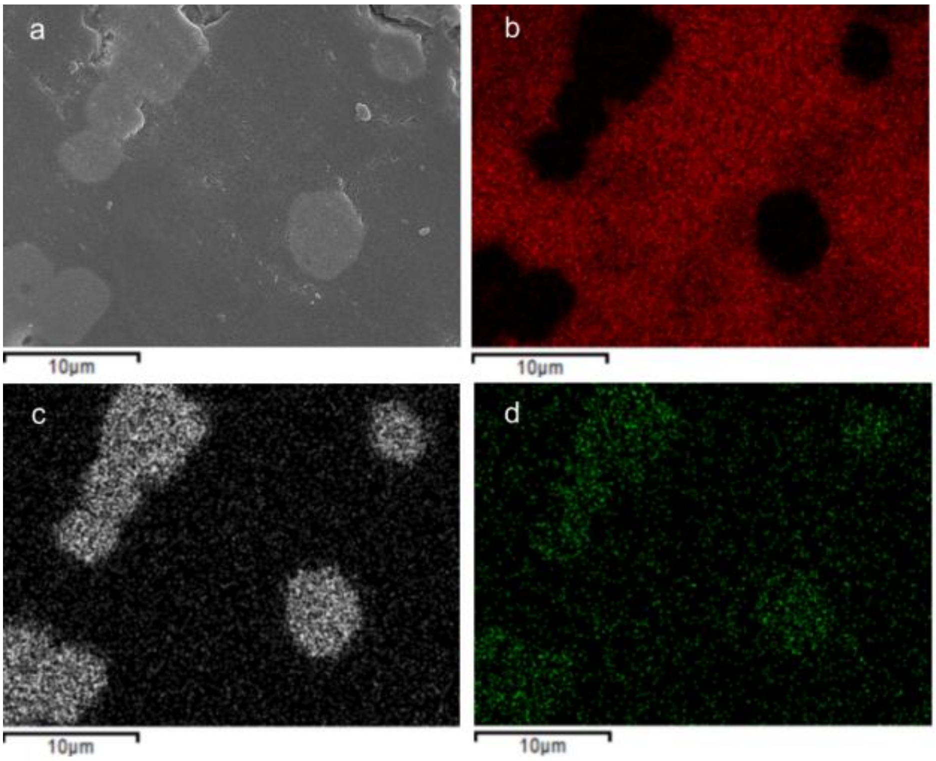

Figure 2.5: Maps of the elements (b) silicon = red, (c) zirconium = white, (d) boron = green present on the detail SEM image of sample S25Z75.

Surface material	Equilibrium contact angle ϑ [°] of molten silicon					
Unreacted glassy carbon	>120	[27, 28]				
Reacted glassy carbon	10÷40	[28]	40÷50 $^{a)}$	[29]	35÷40	[27]
Reacted graphite	3÷35 $^{a)}$	[28]	5÷15 $^{b)}$	[29]		
SiC	38,5 ± 2 $^{c)}$	[30]	30 $^{d)}$	[29]	38 $^{d)}$, 41.5 $^{e)}$	[31]
ZrB_2	15 $^{f)}$	[26]				
a) Depending on surface roughness, b) pyrolitic graphite, c) α-SiC, d) sintered, e) β-SiC, f) datum is referred to TiB_2.						

Table 2.V: Literature contact angles of molten silicon on constituent materials.

Table 2.VI shows the phase volume percentages calculated from Fig. 2.4. SiC volume was calculated as the sum of the α-SiC powders and the SiC formed by reaction bonding between glassy carbon and Si. Values in table 2.VI take into account the fact that the porosity, after silicon infiltration, was completely filled by unreacted Si.

Considering that, during reactive infiltration, carbon and Si became SiC as per Eq. (2.1), given the densities of SiC, ZrB_2 (Tab. 2.I) and Si (ρ = 2.33 g/cm^3), it was possible to calculate Si-SiC-ZrB_2 theoretical density and, after samples real density measurements, to estimate porosity.

Sample	Theoretical				Experimental	
	SiC phase (vol.%)	ZrB_2 phase (vol.%)	Si phase (vol.%)	$\rho_{theor.}$ [g/cm^3]	$\rho_{exp.}$ [g/cm^3]	Porosity (%)
S100	61.7	0.0	38.3	2.87	2.75	4.2%
S50Z50	43.8	18.8	37.4	3.43	3.30	3.8%
S25Z75	41.0	31.6	27.4	3.88	3.85	0.8%

Table 2.VI: Calculated phase volume fractions and overall densities on a ideally fully infiltrated sample. Measured density and estimated porosity.

2.3.2 Oxidation behavior

Fig. 2.6 shows the SEM analysis of the Si-SiC specimens (S100). From a morphological point of view, a continuous 20÷30 μm external layer can hardly be detected, but it becomes evident if oxygen mapping is performed (Fig. 2.6(b)). Even at higher magnifications (Fig. 2.6(d)) the interface between oxidized and un-oxidized material is undistinguishable without the help of the oxygen map (Fig. 2.6(e)), meaning that the external oxidized layer is well adherent. The composition of the oxidized layer is primarily SiO_2, according to EDS analysis.

Fig. 2.7 shows a SEM analysis of the specimen with the highest amount of ZrB_2 (S25Z75). Similarly to Fig. 2.6, it is rather difficult to distinguish an oxidized layer (Fig. 2.7(a)), but one does become evident with the help of an oxygen map (Fig. 2.7(b)). Scale thickness is around 20÷30 μm and it is composed of two phases; ZrO_2 (phase 3) and SiO_2 (phase 4). In the same figure the labels phase 1 and phase 2 are referred to ZrB_2 and Si-SiC, respectively. It is possible to point out that the difference between ZrB_2 and ZrO_2 is distinguishable also by a morphological point of view: ZrB_2 particles have smooth contours while ZrO_2 particles in the oxidized material have irregular and broken contours.

Boron distribution is difficult to characterize due to the low sensitivity of energy-dispersive spectroscopy to light elements but, as suggested by the literature on UHTCs [11, 13, 20], boron is oxidized to B_2O_3 which together with SiO_2 forms a borosilicate glass that is reported to significantly increase the resistance to oxygen diffusion through the surface.

Several authors have reported that oxidation of ZrB_2-SiC at 1500°C in air produces a structure that consists of four layers [12, 21, 22, 32]:

1) continuous SiO_2 on the outer surface;
2) ZrO_2 embedded in amorphous SiO_2;
3) SiC-depleted and ZrB_2;
4) unaffected ZrB_2-SiC.

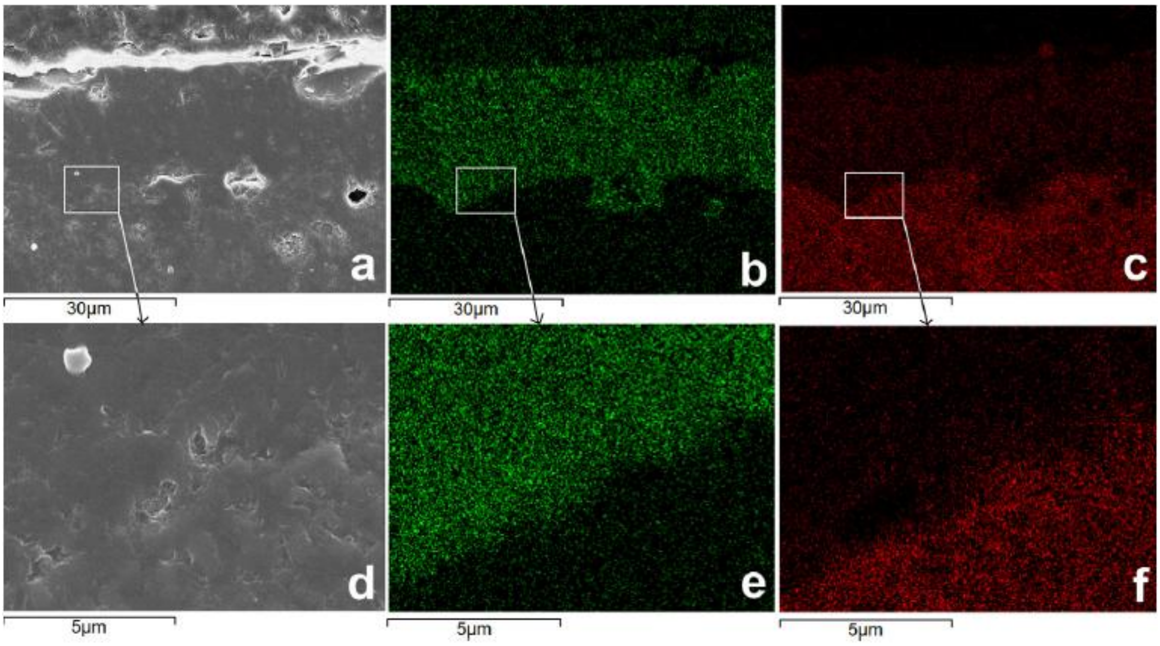

Figure 2.6: SEM analysis of specimen S100 after oxidation. (a) General view with: (b) oxygen map, (c) silicon map. (d) Details of the interface between oxidized and un-oxidized material with: (e) oxygen map and (f) silicon map.

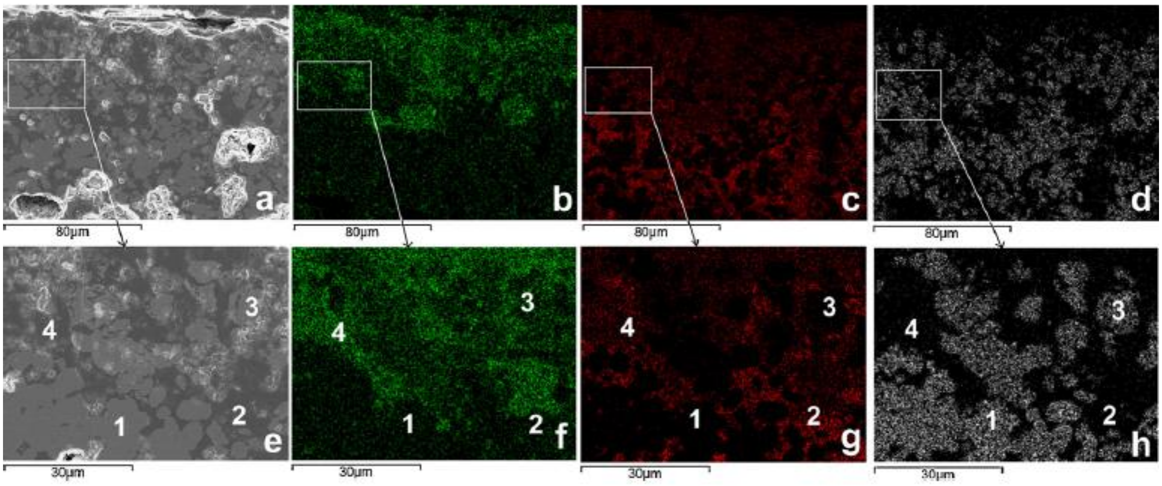

Figure 2.7: SEM analysis of specimen S25Z75 after oxidation. (a) General view with: (b) oxygen map, (c) silicon map, (d) zirconium map. (e) Details of the interface between oxidized and un-oxidized material with: (f) oxygen map, (g) silicon map and (h) zirconium map.

Conversely to these findings, our oxidized Si-SiC-ZrB_2 specimens showed two layers (Fig. 2.7):

1) ZrO_2 embedded in SiO_2 and B_2O_3;
2) unaffected Si-SiC-ZrB_2.

These results are comparable with other Si-SiC-ZrB_2 systems employed as a protective coating [16, 17] which were oxidized in similar conditions. Si-SiC-ZrB_2 systems differ from ZrB_2-SiC by the relative amount of SiC, which is much higher in Si-SiC-ZrB_2 and, of course, by the presence of unreacted silicon. An oxidation campaign is currently ongoing, in order to better understand Si-SiC-ZrB_2 oxidation behavior.

2.4 Conclusions

This work shows that Si-SiC-ZrB_2 composite bulks can be produced via silicon reactive infiltration. Although the process was kept as simple as possible in order to prove its cost efficiency, some features, like powder size selection and mixing, need to be improved in order to avoid powder agglomeration. ZrB_2 powders did not react with molten silicon and remained a separate phase within the composite system. Preform porosity of samples after pyrolysis was intentionally kept at ~ 50% to ease Si infiltration. These high values affect the corresponding quantity of unreacted silicon after reactive infiltration. Further work will focus on reducing preform porosity and Si quantity.

Oxidized Si-SiC-ZrB_2 presented a double layer structure:

1) ZrO_2 embedded in SiO_2 and B_2O_3;
2) unaffected Si-SiC-ZrB_2.

The SiO_2 and B_2O_3 layer seems to act as a better oxygen barrier for the unaffected material. The typical SiC depleted region, present in oxidized ZrB_2-SiC materials, was not observed in this study.

2.5 References

[1] W. B. Hillig, R. L. Mehan, C. R. Morelock, V. J. DeCarlo and W. Laskow, *Silicon-Silicon Carbide Composites*, Am. Ceram. Soc. Bull., 54 [12] 1054-6 (1975).

[2] M. W. Chase Jr., *NIST-JANAF Thermo-chemical Tables*, fourth edition, J. Phys. Chem. Ref. Data, (Monograph 9) 1-1951 (1998).

[3] B. Heidenreich, *Melt Infiltration Process in Ceramic Matrix Composites*, in: W. Krenkel (Ed.), Wiley-VCH, 113-9 (2008).

[4] Y. Wang, S. Tan and D. Jiang, *The Effect of Porous Carbon Preform and the Infiltration Process on the Properties of Reaction-Formed SiC*, Carbon, 42 [8-9] 1833-9 (2004).

[5] N. S. Jacobson, *Corrosion of Silicon-Based Ceramics in Combustion Environments*, J. Am. Ceram. Soc., 76 [1] 13-28 (1993).

[6] C. E. Ramberg and W. L. Worrell, *Oxygen Transport in Silica at High Temperatures: Implications of Oxidation Kinetics*, J. Am. Ceram. Soc., 84 [11] 2607-16 (2001).

[7] R. A. Cutler, *Engineering Properties of Borides*, in ASTM Engineered Materials Handbook, vol. 4 Ceramics and Glasses, Schneider, S.J., technical chairman, 787-803 (1991).

[8] M. J. Gasch, D. T. Ellerby and S. Johnson, *Ultra High Temperature Ceramic Composites*, in: N. P. Bansal (Ed.), Handbook of Ceramic Composites, Springer US, 197-224 (2005).

[9] W. G. Fahrenholtz, G. E. Hilmas, I. G. Talmy and J. A. Zaykoski, *Refractory Diborides of Zirconium and Hafnium*, J. Am. Ceram. Soc., 90 [5] 1347-64 (2007).

[10] S.-Q. Guo, *Densification of ZrB_2-Based Composites and their Mechanical and Physical Properties: A Review*, J. Eur. Ceram. Soc., 29 [6] 995-1011 (2009).

[11] E. Eakins, D. D. Jayaseelan and W. E. Lee, *Toward Oxidation-Resistant ZrB_2-SiC Ultra High Temperature Ceramics*, Metall. Mater. Trans. A, 42 [4] 878-87 (2011).

[12] W. G. Fahrenholtz, *Thermodynamic Analysis of ZrB_2-SiC Oxidation: Formation of a SiC-Depleted Region*, J. Am. Ceram. Soc., 90 [1] 143-48 (2007).

[13] F. Peng, Y. Berta and R. F. Speye, *Effect of SiC, TaB_2 and $TaSi_2$ Additives on the Isothermal Oxidation Resistance of Fully Dense Zirconium Diboride*, J. Mater. Res., 24 [5] 1855-67 (2008).

[14] N. Padmavathi, K. K. Ray, J. Subrahmanyam, P. Ghosal and S. Kumari, *New Route to Process Uni-Directional Carbon Fiber Reinforced (SiC + ZrB_2) Matrix Mini-Composites*, Mater. Sci., 44 [12] 3255-64 (2009).

[15] H. Hu, Q. Wang, Z. Chen, C. Zhang, Y. Zhang and J. Wang, *Preparation and Characterization of C/SiC-ZrB_2 Composites by Precursor Infiltration and Pyrolysis Process*, Ceram. Int., 36 [3] 1011-16 (2010).

[16] Y. D. Blum, J. Marschall, D. Hui and S. Young, *Thick Protective UHTC Coatings for SiC-Based Structures: Process Establishment*, J. Am. Ceram. Soc., 91 [5] 1453-60 (2008).

[17] H. Zhou, L. Gao, Z. Wang and S. Dong, *ZrB_2-SiC Oxidation Protective Coating on C/C Composites Prepared by Vapor Silicon Infiltration Process*, J. Am. Ceram. Soc., 93 [4] 915-9 (2010).

[18] S. J. Wheeler, J. Sibold and I. Reimans, *The Effect of Carbon on the Processing of SiC/SiC_f Composites*, in: J.P. Singh, N.P. Bansal, M. Singh (Eds.), Advances in Ceramic Matrix Composites VIII, John Wiley & Sons, 43-53 (2002).

[19] C. A. Nannetti, A. Borello, D. A. de Pinto, D. Carbone, A. Licciulli and A. Ortona, *C Fiber Reinforced Ceramic Matrix Composites by a Combination of CVI, PIP and RB*, in: W. Krenkel, R. Naslain, H. Schneider (Eds.), High Temperature Ceramic Matrix Composites, Wiley-VCH Verlag GmbH & Co. KGaA, Weinheim, 368-74 (2006).

[20] A. Rezaie, W. G. Fahrenholtz and G. E. Hilmas, *Evolution of Structure during the Oxidation of Zirconium Diboride-Silicon Carbide in Air up to 1500°C*, J. Eur. Ceram. Soc., 27 [6] 2495-501 (2007).

[21] E. J. Opila, S. Levine and J. Lorincz, *Oxidation of ZrB_2- and HfB_2-Based Ultra High Temperature Ceramics: Effect of Ta Additions*, J. Mater. Sci., 39 [19] 5969-77 (2004).

[22] M. Gasch, D. Ellerby, E. Irby, S. Beckman, M. Gusman and S. Johnson, *Processing, Properties, and Arc Jet Oxidation of Hafnium Diboride/Silicon Carbide Ultra High Temperature Ceramics*, J. Mater. Sci., 39 [19] 5925-37 (2004).

[23] S. C. Zhang, G. E. Hilmas and W. G. Fahrenholtz, *Mechanical Properties of Sintered ZrB_2-SiC Ceramics*, J. Eur. Ceram. Soc., 31 [5] 893-901 (2011).

[24] S. C. Zhang, G. E. Hilmas and W. G. Fahrenholtz, *Pressureless Sintering of ZrB_2-SiC Ceramics*, J. Am. Ceram. Soc., 91 [1] 26-32 (2008).

[25] http://www.schunk-sik.com/en/schunk01.c.9111.de/all_productarticle.

[26] G. V. Samsonov, A. D. Panasiuk and M. S. Boriskova, *Wettability of Group IV Metal Borides by Molten Metals*, Smachivaemost Poverrkh. Svoistva Rasplavov Tverd. Tel-Naumka Dumka-Kiev, (1972).

[27] O. Dezellus, S. Jacques, F. Hodaj and N. Eustathopulos, *Wetting and Infiltration of Carbon by Liquid Silicon*, J. Mater. Sci., 40 [9-10] 2307-11 (2005).

[28] J.-G. Li and H. Hausner, *Reactive Wetting in the Liquid-Silicon/Solid-Carbon System*, J. Am. Ceram. Soc., 79 [4] 873 (1996).

[29] T. J. Whalen and A. T. Anderson, *Wetting of SiC,* Si_3N_4 *and Carbon by Si and Binary Si Alloys*, J. Am. Ceram. Soc., 58 [9-10] 396 (1975).

[30] C. Rado, S. Kalegeropoulou and N. Eustathopulos, *Wetting and Adhesion in Metal-Silicon Carbide Systems: the Effect of Surface Polarity of SiC*, Scripta Mater., 42 [2] 203-8 (2000).

[31] P. Nikolopoulos, S. Agatho Pou Los, G.N. Angelopoulos, A. Naoumidis and H. Grűbmeier, *Wettability and Interfacial Energies in SiC-Liquid Metal Systems*, J. Mater. Sci., 27 [1] 139-45 (1992).

[32] E. J. Opila and M. C. Halbig, *Oxidation of* ZrB_2*-SiC*, Ceram. Eng. Sci. Proc., 22 [3] 221-28 (2001).

3. Short-term and long-term oxidation behavior of Si-SiC-ZrB_2 composites produced by SRI

3.1 Introduction

Dense silicon carbide materials are commonly employed in air at high temperatures because their outer SiO_2 scale, under passive oxidation conditions, has the lowest permeability to oxygen among common oxides [1]. By “dense SiC” one usually refers to ceramics without open/close porosity produced by techniques such as sintering (pressureless or pressure assisted), chemical vapour deposition (CVD), self-propagating high-temperature synthesis (SHS) or spark plasma sintering (SPS). The drawback of these techniques is that they are expensive, in fact the high melting points and the strong covalent interactions present in UHTCs make it difficult to achieve uniform densification in these materials. Densification is only achieved at temperatures above 1800°C once grain boundary diffusion mechanisms become active [2, 3]. Furthermore these techniques present limitations in product thickness or shape and, in the case of pressureless sintering, may contain sintering aids (typically carbon [4] and boron [4]) which, under particular operating conditions, decrease oxide scale viscosity and thus enhance oxygen diffusion [5]. Silicon carbide ceramics produced by silicon reactive infiltration (SRI) were first obtained by Hillig et al. [6]. They infiltrated carbonaceous material with molten Si under 10^{-2} mbar residual pressure at temperatures ranging from 1450°C to 1600°C. This process allows the shaping and consolidation of preforms made of ceramic powders or fibers that are bound by a polymer with a high carbon yield after pyrolysis. Reaction-bonded SiC ceramics have low synthesizing temperatures, short processing times and minimal dimension changes after the densification process (near-net shaping) in comparison with pressure-less sintered SiC and hot-pressed sintered SiC. Morover, fine, high purity SiC powders are not required for the fabrication of reaction-bonded SiC ceramics, which results in a significant reduction in cost. The major drawback of this technique is that SiC grains are interpenetrated with a continuous phase made of unreacted silicon which melts at 1423°C. Liquid silicon may reduce the thermo-mechanical properties of the composite and their resistance to oxygen. This is why the application of these multiphase materials is currently foreseen as a coating or as a matrix in fiber reinforced composites in a specific range of temperatures (1400÷1600°C) or in applications where no mechanical loads are applied. In TPS (thermal protection system), however, high mechanical strength is not required so that for this application have been proposed materials such as SiC, ZrB_2 and their composites that in the conditions of reentry into Earth's atmosphere may give rise to oxidizing vitreous phases that become progressively more fluid with increasing temperature.

SiC has been added to transition metal diborides (ZrB_2 and HfB_2) for aerospace applications to increase the relative poor oxidation resistance of pure ZrB_2 and HfB_2 at temperatures above 1600°C [7]. At these temperatures several researchers reported the formation of an oxide scale of borosilicate glass layer (BSZ) containing SiO_2, ZrO_2 and B_2O_3 and the formation of an intermediate region, between the oxides and the unreacted material, characterized by SiC depletion [8-10]. Recently Willams et al. [11] studied the oxidation performance of ZrB_2-SiC composites with a significantly higher amount of SiC than the standard 20÷30 vol.%. They showed that oxidized samples containing > 50 vol.% of SiC did not present a SiC depleted region because their larger SiC reservoir did not allow SiO (g) to be transported from the SiC depleted region to the SiO_2 layer. In the general case, the mechanism of an interfacial reaction of composite oxidation can be represented as the formation of a reaction interface and the subsequent interaction of a solid phase with products of melt dissociation and afterwards gaseous by-products. The rate of the process is governed by the diffusion of reaction products in the growing scale layer and the three-dimensional decrease in the reactant volume due to the propagation of the reaction interface [12]. The oxidation processes of refractory carbides/borides have been shown to be the combined processes of oxygen inward or metal ion outward diffusion and gaseous (or liquid at relatively lower temperatures) by-product outward diffusion through oxide scale. Therefore, the oxidation resistances of carbides/borides are largely influenced by the formation and escape of gaseous by-products (such as CO, CO_2, B_2O_3) during the oxidation processes which are significantly different from those of their metal counterparts.

In the previous chapter we presented Si-SiC-ZrB_2 composites produced by SRI [13]. Both works showed similar oxide layers and the absence of a SiC depleted region. The main difference, mainly due to the presence of silicon, stands in the thickness of the outer borosilicate layer. This chapter presents a detailed study of the mutual interactions between the Si-SiC-ZrB_2 constituent materials during their processing and of their chemical activity with oxygen at high temperatures in the prospect of using this material as a matrix of a continuous fiber reinforced composite.

The first part of this chapter is devoted to the study of the early stage of oxidation (up to 2 hours at 1600°C), while the second part is focused on the long-term oxidation of some selected samples at a high temperature (1500°C) for dwelling times of up to 48 hours. The microstructural features after long-term oxidation were reported and discussed, together with the weight gains and the average thicknesses of the resulting scale. The oxidation process was then analyzed on the basis of elemental maps and XRD patterns taken on the surface of the specimens. In addition, the effect of oxidation time on the room-temperature flexural strength was also studied.

As silicon is the more reactive component in Si-SiC-ZrB_2 composites, we also developed a technique to quantify its amount from the analysis of the silicon XRD peaks. Si wt.% was inferred from a curve that was drawn on the basis of data from XRD acquisitions of Si-SiC powder samples with a known composition.

3.2 Experimental procedure

3.2.1 Materials

The composites were produced by mixing ceramic powders with a plastic binder. The ceramic powders and the plastic binder employed in this chapter were respectively:

- α-silicon carbide (Grade UF 05,. Stark Ag, Goslar, D) with an average particle size d50 of 1.4 μm and a specific area of 4÷6 m^2/g;
- zirconium diboride (grade A, Stark Ag, Goslar, D), the particle size d50 is 0.3÷5.0 μm;
- micronized (~ 64 μm diameter) phenolic novolac powder (Momentive, Columbus, OH, USA).

Different compositions, (Tab. 3.I), were prepared in order to study the effect of the constituent materials on the ceramic microstructure before and after their oxidation.

Four vol.% compositions were selected for the ceramic part of the mix (Tab. 3.I). Each one of these compositions was mixed with the phenolic resin in three different volume fractions. The first three ceramic compositions have been studied in the short-term oxidative treatment, while for the long-term oxidative study only the batches with the 40 vol.% of phenolic resin were chosen. In the short-term oxidation, the data were acquired also on Si-SiC composites produced by SRI and on SiC and ZrB_2 samples pressureless sintered for comparison.

Vol.% in the ceramic content		**Vol.% in the mix**		
ZrB_2	**SiC**	**ZrB_2**	**SiC**	**Ph. Res.**
100	0	70.00 60.00 50.00	0.00 0.00 0.00	30.00 40.00 50.00
75	25	52.50 45.00 37.50	17.50 15.00 12.50	30.00 40.00 50.00
50	50	35.00 30.00 25.00	35.00 30.00 25.00	30.00 40.00 50.00
0	100	- 0.00 -	- 60.00 -	- 40.00 -

Table 3.I: Volume fractions of constituent materials in the ceramic powders and in the mix green before forming by cold uniaxial pressing.

3.2.2 Sample preparation

Samples were produced improving on the process adopted in the previous chapter, by performing wet instead of dry milling. The powders were mixed with distilled water (70 wt.%) for 60 minutes by ball milling in a sealed container, then the phenolic powder was added and milling continued for a further 60 minutes. The compound was dried in a vacuum oven at 60°C for 24 hours. Ambient temperature pressing was then performed with an uniaxial press. The holding time and pressure were respectively 150 seconds and 56 MPa. The amount of the mix to put into the die was calculated in order to produce, after pressing, 4÷5 mm thick green preforms.

The green samples were pyrolysed at 1000°C under inert atmosphere and the pyrolysis details can be found in the previous chapter. After pyrolysis, samples were measured and weighed. They were then positioned on carbon wicks placed on a BN painted graphite plate. Silicon flakes were put onto the samples. The set up was heated at 1500°C with a

10^{-2} mbar residual pressure in a vacuum furnace which was quickly brought to the dwelling temperature and held for 1h (for details see chapter 2). The furnace was then slowly brought to environment temperature by natural cooling.

For the TGA measurements, to avoid the influence of the sample surface area, the specimens were milled and cut in 3 x 3 x 3 mm^3 (± 0.01 mm) cubes with diamond tools.

For the bending tests plates with dimensions of 90x40x4 mm^3 were milled and cut with diamond tools to produce 25x5x2 mm^3 bars.

3.2.3 Short-term oxidation treatment

With the aim to compare oxidized Si-SiC-ZrB_2 with other studies in literature for similar systems [14, 15] and for SiC materials [16, 17], specimens were oxidized at 1600°C in a resistance heated furnace (HT64/17, Nabertherm GmbH, Lilienthal, Germany) in static air at atmospheric pressure. To avoid contact with the furnace, the samples were placed in an alumina boat. As this work intends to study their early stage of oxidation, each set of samples was brought to 1600°C with a heating rate of $10°C\cdot min^{-1}$ and held at that temperature for 5, 30 and 120 minutes.

3.2.4 Long-term oxidation treatment

With the purpose of comparing oxidized Si-SiC-ZrB_2 with other works [2, 12, 18-24] and sintered SiC, specimens were oxidized at 1500°C with a resistance heated furnace (HT64/17, Nabertherm GmbH, Lilienthal, Germany) in static air at atmospheric pressure for 4, 8, 24 and 48 hours. The eight-hour time was achieved with two cycles of 4 hours, while 48 hours were obtained with two cycles of 24 hours. The furnace was slowly heated and cooled to avoid thermal shock on the samples and preserve the oxide layer. To prevent contact with the furnace in order to evaluate the weight gain of the samples, silicon carbide fibers were employed as supports for the specimens. The fibers were suspended between two alumina plates. This solution allowed the contact surface of the samples to be minimized and thus the weight variations of the specimens to be more accurately evaluated.

3.2.5 Characterisation methods

Samples were characterized by several techniques.

Thermogravimetry analysis was carried out using TGA/SDTA 851^{e}Module, (Mettler Toldedo Inc., Im Langacher Greifensee CH) from RT to 1600°C using a heating rate of 10°C min^{-1}. The atmospheric conditions were dry air and different contents of oxygen in argon (respectively 0.25%, 1%, 10% and 21% of O_2 in Ar) with all of them flowing at 50 ml min^{-1}. The sample density was measured with a He pycnometer (ASAP 2010, Micromeritics, Norcross, GA, USA) and by water pycnometry.

Microstructure evaluations were performed with an optical microscope (Leica DMLM, Wetzlar, D) and scanning electron microscopy (SEM-FEG Assing SUPRA 25, Zeiss, Germany) coupled with energy dispersive spectroscopy (EDS Oxford INCA X-Sight analyzer). Phase quantification was performed, during micrograph acquisition, with the Gimp 2.6.11 (GNU Image Manipulation Program). XRD analysis was performed with a X-ray generator system (PW3830, Philips, Eindhoven, Netherlands).

A key factor in this typology of composite material is represented by the amount of unreacted silicon present in the material. To evaluate this amount, an ad-hoc procedure was developed. It consisted in preparing five standards covering the range of the expected phase composition of the samples. The standards were made by mixing powders of silicon (≥ 99.7% of purity, average particles size < 150 μm; Schuchardt, Műnchen, D) with powders of silicon carbide (grade UF-10, Stark Ag, Goslar, D); with the following weight percentages of silicon: 3%, 5%, 10%, 15% and 25%.

A calibration curve was then drawn correlating the integrated areas of the XRD diffraction pattern peaks of Si (111) for each standard.

Calibration was performed by using the peak areas. In principle this is more accurate than exploiting their intensities (peak heights) or their width at half maximum (FWHM). The intensities are in fact conditioned by the percentage of crystallinity of the material, while the width is affected by the size of the crystallites. Using the areas, the two above mentioned effects can be minimized. The peak considered was the peak at 28.5° (corresponding to the plane (111)), the most intense for the crystalline silicon.

Before and after long-term oxidation, the specimens were weighed using an analytical balance (Bc, Orma, Milan, Italy) with an accuracy of 0.1 mg. The final mass change rates of the specimens were averaged on six samples for 4h, 24h and on three samples for 8h, 48h.

The flexural strength of the as produced and oxidized bars was determined via three-point bending with a span of 20 mm and a crosshead speed of 0.2 mm/min (Sintech 10/D, MTS, Eden Prairie, Minnesota USA). For each composition and oxidation time, at least three specimens were tested.

3.3 Results and discussion

3.3.1 As produced composites

Figure 3.1 shows the morphology of the samples produced in this work. They are fully dense composites bound by an unreacted silicon matrix (gray phase). Well dispersed ZrB_2 powders (large white particles) are clearly visible in the microstructures as well as the α-SiC (larger black particles) and β-SiC smaller black particles. This newly produced phase is the result of the reaction between the pyrolyitic carbon (from the phenolic resin) with silicon. Their fine grained feature depends on the poor mechanical integrity of pyrolytic carbon which was further shredded by the highly exothermic reaction with liquid silicon [25]. As expected, in column 100-0 of figure 3.1, α-SiC powder is not visible, the visible large black areas correspond to voids left by ZrB_2 powders popping up during sample polishing.

An Energy-dispersive X-Ray spectroscopy (EDS or EDX) analysis on these three phases confirmed that the gray zones are made of Si, the black ones of SiC and the white areas of ZrB_2.

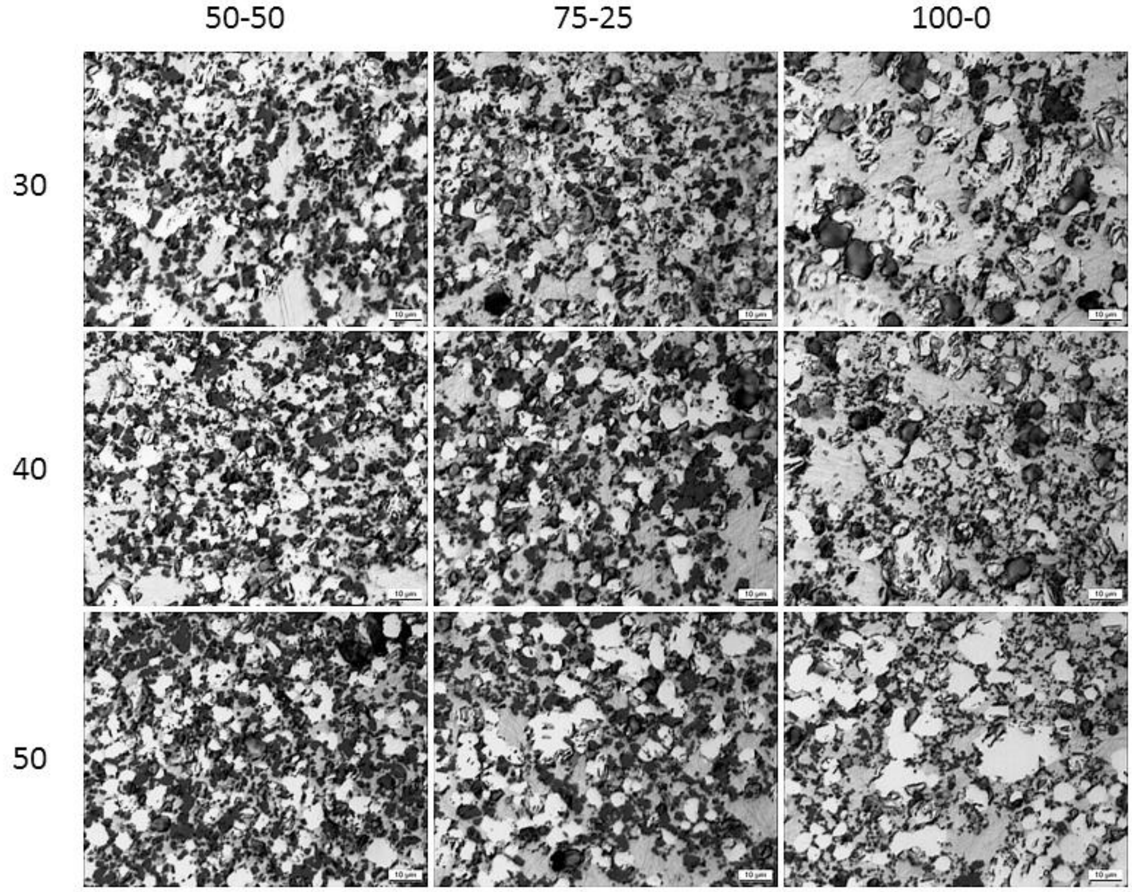

Figure 3.1: Micrographs of the samples with different content of ceramic powder (top labels) and phenolic resin (left labels) after liquid silicon reactive infiltration.

Table 3.II summarizes the open porosity calculations inferred from the different density measurements. The He density measurements show good agreement with H_2O ones. The open porosity, evaluated by the difference between H_2O or He density and geometric density, shows very low values confirming the effectiveness of the reactive silicon infiltration, with the exception of the samples 75-25-50 and primarily the 50-50-50, demonstrating that in those cases full infiltration was not accomplished. This is probably due to the higher amount of phenolic resin and consequent worse wetting behavior of the silicon on pyrolytic carbon [26, 27].

The patterns in figure 3.2 show the crystalline phases detected by the instrument in the samples with 40% of phenolic resin after the SRI (the samples chosen for a more thorough characterization). All the three samples display the same three crystal phases, namely: silicon, silicon carbide (both polymorphs: α-SiC and β-SiC) and zirconium diboride. The shape of the peaks indicates a high degree of crystallinity and the absence of amorphous phases. It is clear from the XRD patterns that during molten infiltration, silicon did not react with ZrB_2 and formed β-SiC with the polymer derived carbon.

Samples	**Density [g/cm^3]**		
	He picnometry	**H_2O picnometry**	**Geometric**
SiC sintered	3.2	3.0	2.9
ZrB_2 sintered	6.1	5.4	5.1
100-0-50	-	4.0	3.9
100-0-40	4.1	4.1	4.0
100-0-30	-	4.2	4.1
75-25-50	-	3.7	3.3
75-25-40	3.8	3.8	3.7
75-25-30	-	3.9	3.8
50-50-50	-	3.5	2.8
50-50-40	3.5	3.5	3.3
50-50-30	-	3.6	3.5

Table 3.II: Density of the references and samples.

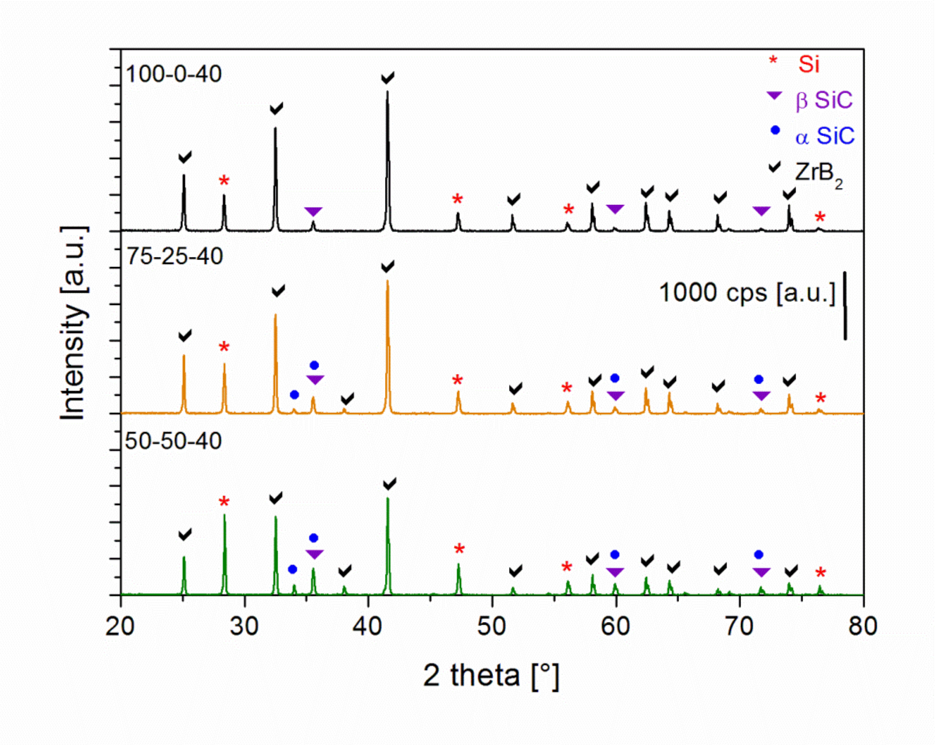

Figure 3.2: XRD Patterns of 100-0-40, 75-25-40 and 50-50-40 sample, respectively.

Table 3.III shows the data used to construct the calibration curve (Fig. 3.3) by fitting the experimental points with a Lorentzian function. This was then used to retrieve the silicon wt.% by including the corresponding peak area in the graph.

Standard	**Peak Area of Si (2θ ~ 28.5°)**	**Wt.% of Si (Standards)**
1	407.02	25
2	169.49	15
3	98.30	10
4	28.32	5
5	27.13	3
Sample	**Peak Area of Si (2θ ~ 28.5°)**	**Wt.% of Si calculated from peak areas of Si (2θ ~ 28.5°)**
50-50-40	164.06	14.6
75-25-40	116.56	11.8
100-0-40	93.53	10.2

Table 3.III: Values of the integrated peak areas (from XRD) and weight percentages of free silicon. In the case of the standards they were imposed, in the case of the samples they were obtained intersecting the calibration curve with the measured value of the peak area.

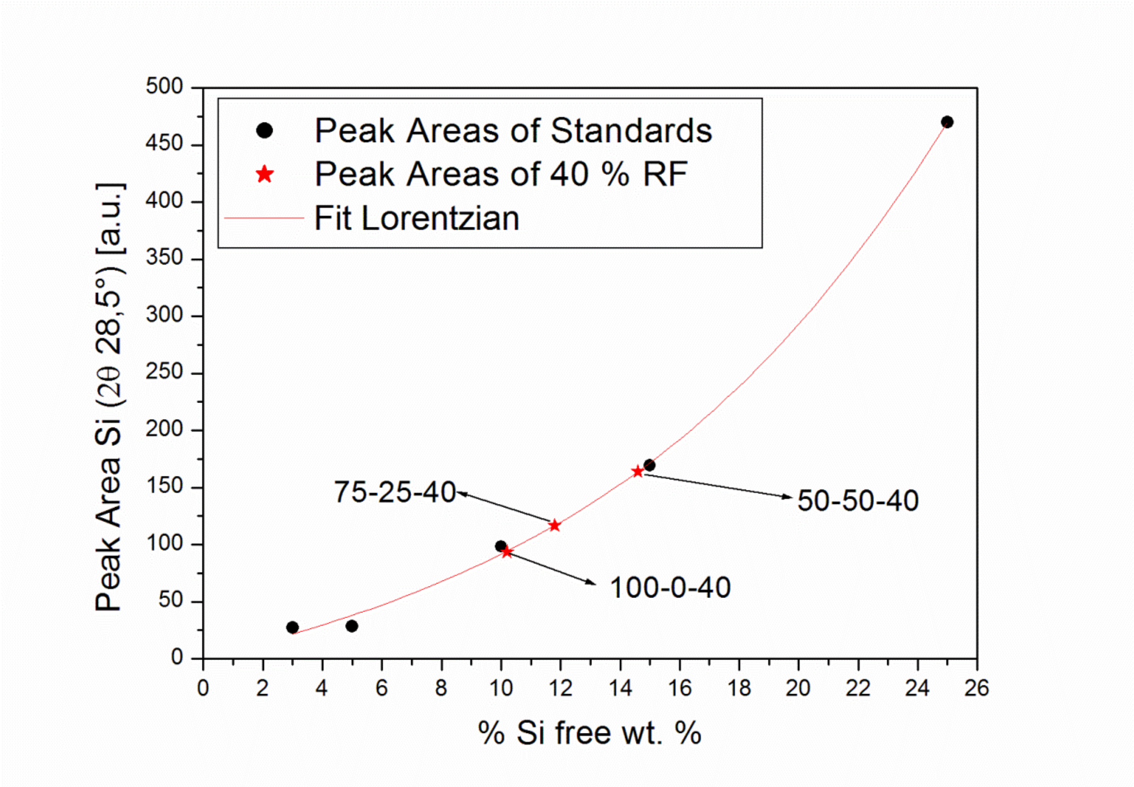

Figure 3.3: Calibration curve on the experimental points of the standards with the peak area of Si for the samples. These weight percentages were subsequently converted to volume percentages in table 3.IV using the following densities: 2.3 g/cm^3, 3.18 g/cm^3 and 6.2 g/cm^3 for Si, SiC and ZrB_2, respectively.

At the bottom of table 3.III the percentages of free silicon in the samples are given. It should be noted that the sample with the greatest amount of unreacted silicon is the 50-50-40, approximately 15% by weight. Finally, table 3.IV shows the distribution of the three phases (vol.%) in the samples from the batch with 40% of phenolic resin. The percentages of Si and SiC added and ZrB_2 have been deduced from the image analysis. This was done by greatly increasing the contrast between the phases, on different sections and obtaining negative images on which the percentages were computed. Table 3.IV shows large differences between the calculated and the measured phase composition. These differences can be ascribed to the different shrinking of the samples during thermal treatments, i.e. pyrolysis and high temperature treatment (Tab. 3.IV). During pyrolysis, the binding polymer experienced a mass loss which was accompanied by a volume reduction (Tab. 3.IV).

Taking for granted the complete inertness of the ceramic powders, one can assume that the diverse Si contents can also be ascribed to the different carbon yield of the binder caused by its different distribution within the powders, i.e. coarse (ZrB_2) or fine (SiC).

Sample	**After LSI**			**After pyrolysis**	
	Si [vol.%]	**SiC [vol.%]**	**ZrB_2 [vol.%]**	**Linear shrinking [%]**	**Weight loss [wt.%]**
100-0-40	13.3	53.0	33.7	1.17	3.01
75-25-40	15.4	58.7	25.9	1.94	2.93
50-50-40	18.8	60.0	21.2	2.14	3.39

Table 3.IV: Percentage volume distribution of the phases in the samples with 40% of phenolic resin after SRI obtained from calibration with X-ray and image analysis. Linear shrinking and weight loss after pyrolysis.

3.3.2 Oxidation behavior

Most of the current understanding on the oxidation of SiC, ZrB_2 and ZrB_2-SiC composites is based on thermo-gravimetric analysis, oxygen consumption studies and *ex situ* evaluation of microstructural changes. While thermo-gravimetric methods provide useful information based on weight changes during oxidation, they record the simultaneous occurrence of multiple events, including weight gain due to formation of oxide phases, such as ZrO_2, B_2O_3 and SiO_2, weight loss due to vaporization of CO, B_2O_3 and perhaps SiO. As a result, the TGA data needs to be deconvoluted and requires careful interpretation [7]. The TGA in air curves of figure 3.4A shows three different oxidation behaviors.

The SiC and Si-SiC thermograms in figure 3.4A confirm that both oxidation kinetics of SiC and Si in these composites are rather low [28], in fact small changes in weight were monitored.

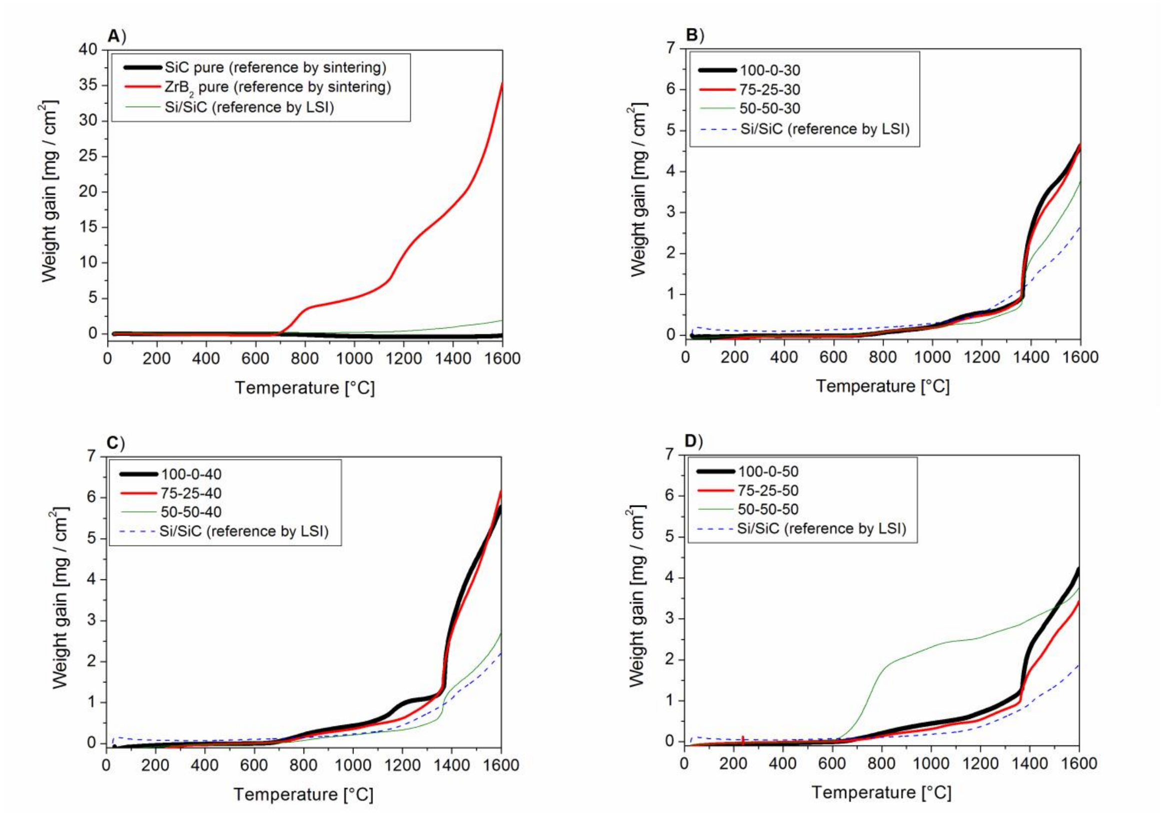

Figure 3.4: A) TGA in air of reference materials; B) TGA in air of the samples with 30 vol.% of phenolic resin (PF); C) TGA in air of the samples with 40 vol.% of PF; D) TGA in air of the samples with 50 vol.% of PF.

According to the literature [29, 30], the temperature range and the composition of the oxidizing atmosphere adopted in this work should cause passive oxidation of SiC and Si according to the reactions:

$$2\ SiC\ (cr) + 3\ O_2\ (g) \rightarrow 2\ SiO_2\ (s) + 2\ CO\ (g) \qquad (3.1)$$

$$Si\ (cr) + O_2\ (g) \rightarrow SiO_2\ (s) \qquad (3.2)$$

Only the atmosphere containing 0.25 vol.% of oxygen in Ar used for one TGA test represents a limit conditions since it could cause active oxidation of Si but passive oxidation of SiC [30].

Both these reactions result in a significant weight gain. On the other hand the relevant thermograms in figure 3.4A show that the mass gain for SiC is lower than 0.5% and that of Si/SiC is only a bit higher, which is consistent with the higher mass gain occurring during silicon oxidation (reaction 3.2). After the formation of a thin silica scale on the surface of these materials the oxidation progresses very slowly because of the low solid state diffusion of oxygen through pure silica (10^{-21} m^2/s). The oxygen diffusing through the passive layer can still react when reaching the interface between the passive layer and the substrate. In principle at this interface the oxygen activity could become low enough to cause active oxidation with formation of gaseous reaction products like SiO and CO. Nevertheless, to the authors knowledge, the literature does not report any example of active oxidation of SiC under the conditions adopted in the present work. The lack of porosity below the passive layer and the growing trend of TGA curves confirm that passive oxidation occurred. The considerable gain in weight of the pure ZrB_2, which already begins at around 700°C, is due to the starting reaction of oxidation (reaction 3.3); it can be explained not only by the great porosity of the sample (around 17%) but also by the microstructure of the oxide layer.

$$2\ ZrB_2\ (cr) + 5\ O_2\ (g) \rightarrow 2\ ZrO_2\ (cr) + 2\ B_2O_3\ (l) \quad (3.3)$$

Below 1100°C pure ZrB_2 shows parabolic oxidation kinetics due to the presence of a dense glassy oxide layer (B_2O_3) that controls the oxygen diffusion because ZrO_2 is a porous skeleton that does not form a protective scale. In addition the diffusion coefficient of oxygen through B_2O_3 is significantly lower than that of ZrO_2 (10^{-12} m^2/s for B_2O_3 and 10^{-10} m^2/s for ZrO_2 at 1500°C) [11]. These components of the oxide layer grant some protection against further oxidation even if they are obviously less effective than silica. From 1100°C to 1400°C paralinear kinetics can be observed resulting from the weight gain due to the formation of B_2O_3 and ZrO_2 and the weight loss due to the evaporation of B_2O_3 (equilibrium 3.4).

$$B_2O_3\ (l) \leftrightarrows B_2O_3\ (g) \quad (3.4)$$

Above 1400°C the volatilization of B_2O_3 is higher than the production of B_2O_3 in a regime of rapid linear kinetics with weight gain, in this case it can be concluded that the weight increase due to the ZrO_2 formed is greater than the weight reduction related to ZrB_2 consumption and to the evaporation of B_2O_3.

In figures 3.4 B, C, D the thermograms of the Si-SiC-ZrB_2 composites are grouped according to the different content of phenolic resin. The oxidative behavior of the different samples turned out to be quite similar with final weight gains that range from at 1.5% to 2.5%. Each of the previous chemical reactions occurred, but the temperature at which the curves show sharp increase in weight gain is 1400°C. This transition was clearly visible in the Si-SiC composite, but it was even more evident in all the Si-SiC-ZrB_2 samples. ZrB_2 thus dramatically influences sample oxidation behavior at this temperature.

This temperature corresponds to the melting temperature of Si and may trigger reaction 3.2. This behavior is in accordance with Ramberg et al.’s [28] previous findings on Si-SiC materials. In that work [28] it was demonstrated that at temperatures above 1400°C the parabolic rate constant (k_P) for siliconized SiC oxidation increases owing to the transition from molecular-interstitial to network-dominant oxygen transport through amorphous SiO_2 scale.

In any case when SiC and ZrB_2 contemporaneously suffer oxidation the microstructure of the oxide scale becomes more and more complex as well as the oxidation mechanism [9, 10, 31, 32]. A glassy borosilica forms on the surface, surrounding crystals of primary zirconia. Borosilica at rather low temperature grants protection from oxidation since the oxygen diffusion coefficient through this glass ($1,7*10^{-14}$ m^2/s for a B_2O_3-21 mol % SiO_2) is lower than those for diffusion in boria and zirconia. Borosilica glass dissolves zirconia and forms channels that connect the interface between the oxide layer and the not oxidized substrate to the surface, oxygen permeation through borosilicate glass channels is believed to occur and also convection currents and liquid flow can be significant during oxidation. Therefore this BSZ glassy phase can act as a carrier of gaseous species that can diffuse in it (molecular O_2, CO, CO_2 and SiO); for this reason it has been proposed that glassy phase can provide the oxygen for the oxidation of the ZrB_2-SiC material bulk [31, 32]. In addition the microstructure of the oxide scale changes with the temperature increase because of the progressive volatilization of boria. The evaporation of boria increases the viscosity of the glassy phase and decreases the solubility of zirconia, then secondary zirconia precipitates on the external part of the scale. Conclusively the oxide scale must be considered as a multi-phase layer showing composition, physical properties (like viscosity) and relative amount of phases changing with the temperature. The oxidation rate is controlled by the oxygen diffusion that can happen according to several mechanisms, and the dominant mechanism likely changes with the temperature variation. This might explain the steeper TGA curves around 1400°C. However, it has to be kept in mind that TGA recorded simultaneous oxidation events.

The only sample that showed an anomalous weight gain was the one labelled 50-50-50, which started at about 600°C. This behavior was in agreement with its higher porosity due to an incomplete SRI. It is, however, worth noting that at 1600°C its cumulative weight change was similar to that of the others.

The increase of both free silicon and SiC content in ZrB_2-SiC-Si specimens seems to improve oxidation resistance, allowing the formation of more silica, as showed by the comparison of Si wt.% (Tab. 3.III) and TGA curves in figure 3.4C.

TGA tests with different mixtures of oxygen in argon showed an oxidizing effect on the composites which was similar to that of dry air, regardless of the ratio of the two gases.

3.3.3 Oxidation behavior after short-term oxidation at 1600°C

Due to the similar oxidative behavior of the samples during the TGA analysis, only the sample 50-50-40 was chosen for a more in-depth characterization after the short-term oxidation. Figure 3.5 shows FESEM photos taken on the edge of the section of the sample after an oxidation time of 30 minutes at 1600°C. Localized EDS analysis revealed a structure made of three layers : (a) a borosilicate layer rich in silica, (b) an intermediate layer containing a BSZ glassy phase and ZrO_2 particles, (c) the bulk un-oxidized material [13]. From a morphological standpoint it can be seen how the silica scale thickness is $100\div150$ μm, while the thickness of the layer below is around $40\div80$ μm (the boundaries between this area and the non-oxidized part and the outer layer are marked with a dashed black line). We could observe, particularly in this sample, that the layer of silica is very porous and with non uniform thickness, presumably because of CO bubble formation [31]. From XRD patterns taken on the surface, the formation of crystalline silica was observed already after 30 minutes, although the shape of the peaks suggests that amorphous silica is also present. Comparing these values with those found in the previous chapter, it can be observed how the main difference is in the higher thickness of the silica layer, while the second layer is comparable with the outer layer found in the chapter 2. As observed in the previous chapter, it was possible to discern between ZrB_2 and ZrO_2 from a morphological point of view: ZrB_2 particles have smooth contours while ZrO_2 particles in the oxidized material have irregular and broken contours. This is also confirmed by Energy-Dispersive X-Ray Spectroscopy (EDS or EDX) analysis on these two different zones.

Fahrenholtz et al. [33], following a model analysis of the volatility diagram for the ZrB_2-SiC system, attributed the formation of a SiC depleted region to a p_{O2} gradient that develops underneath the surface during oxidation in air and results in low oxygen potential at the interface between the oxide scale and the substrate. The SiC depletion relies on active oxidation of SiC (reaction 3.5),

$$SiC\ (cr) + O_2\ (g) \rightarrow SiO\ (g) + CO\ (g) \qquad (3.5)$$

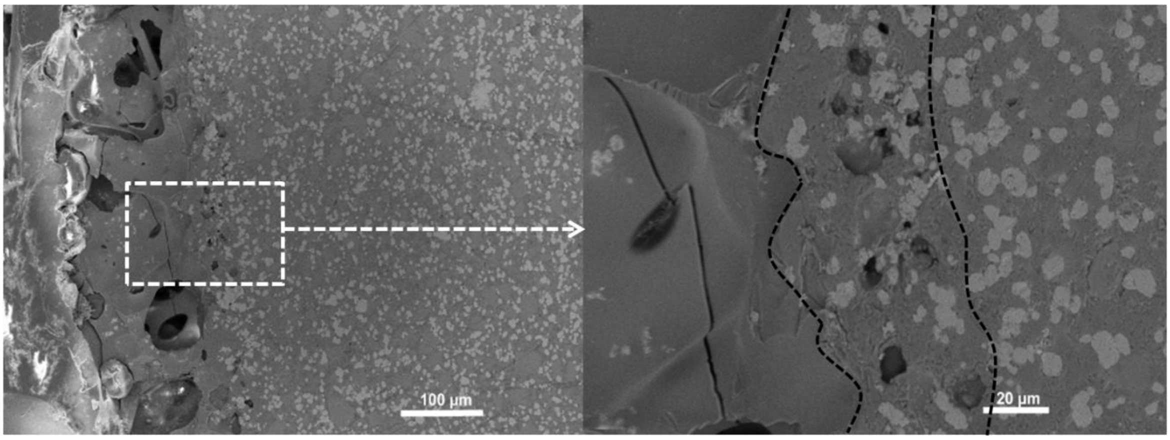

Figure 3.5: FESEM images of 50-50-40, oxidized for 30 minutes at 1600°C (collected with back scattered electrons at lower magnification (500X, left) and zoomed (2000X, right)), on the section of the oxidized layer.

On the other hand a recent study on the oxidation of ZrB_2-SiC compounds with high SiC contents, specifically over the 50 vol.% [11], reports that the formation of a SiC-depleted layer above the ZrB_2-SiC bulk composite was not observed. This result is well consistent with the lack of SiC-depletion layer observed in the present work, which can be related most likely to the low mobility of oxygen in the outer SiO_2 layer. However, a combination of compositional and microstructural factors are likely to control the final microstructure that develops in the oxide scale, i.e. SiC depletion formation or not.

The TGA thermograms on the 50-50-40 sample oxidized for 5 minutes, 30 minutes and 2 hours at 1600°C are shown in figure 3.6. The graphs show that passivation is very effective, in fact, after only 5 minutes of oxidation, the weight gain is drastically reduced compared to the non-oxidized sample. The thermograms do not vary significantly when the oxidation times are increased. Comparing this oxidative behavior with the reference materials, it can be observed how it is similar to that of the SiC (which passivates immediately), while ZrB_2 continues to oxidize significantly even after 2 hours of oxidation. A further confirmation of this passivation characteristic, can be seen by matching the two SDTA (simultaneous difference thermal analysis) curves related to the un-oxidized sample and after 2 hours of oxidation, respectively (Fig. 3.7). The melting of the free silicon can be clearly noticed in the un-oxidized sample in which the endothermic peak at about 1350°C is very pronounced, as well as the final exothermic peak, which is due to the oxidation of SiC (reactions 3.1, 3.2 and 3.5) with the release of gas bubbles at scale/boride interface.

After being subjected to 2 hours of oxidation, the peak relating to the silicon melting is less pronounced (showing that less unreacted silicon is present) and the exothermic oxidation peak has disappeared.

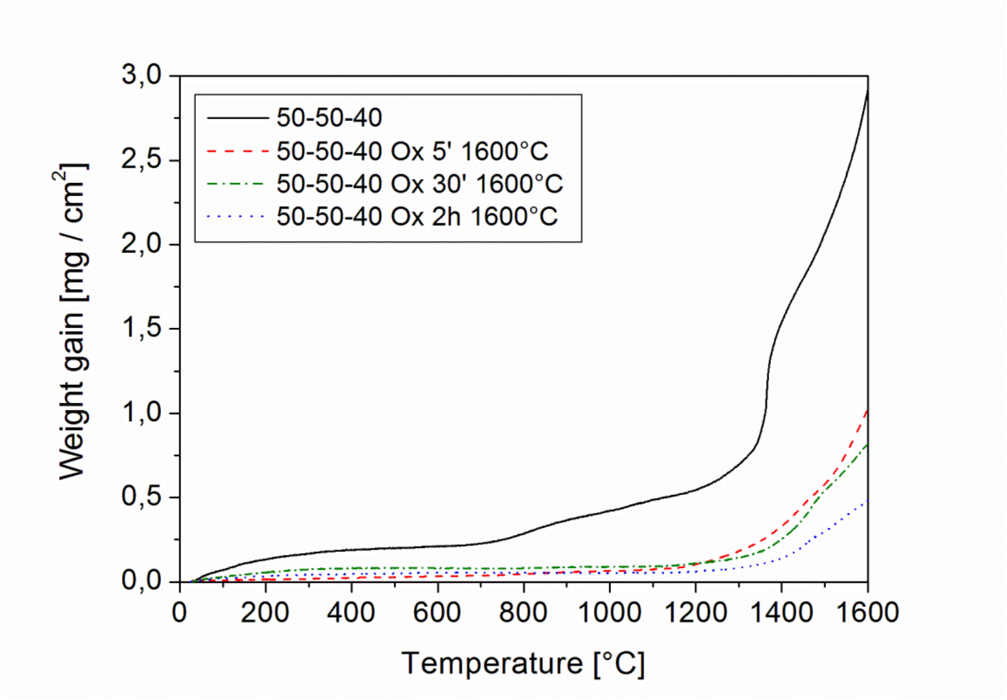

Figure 3.6: TGA in air of the sample 50-50-40 after different times of oxidation at 1600°C as produced, after 5 minutes, after 30 minutes and after 2 hours.

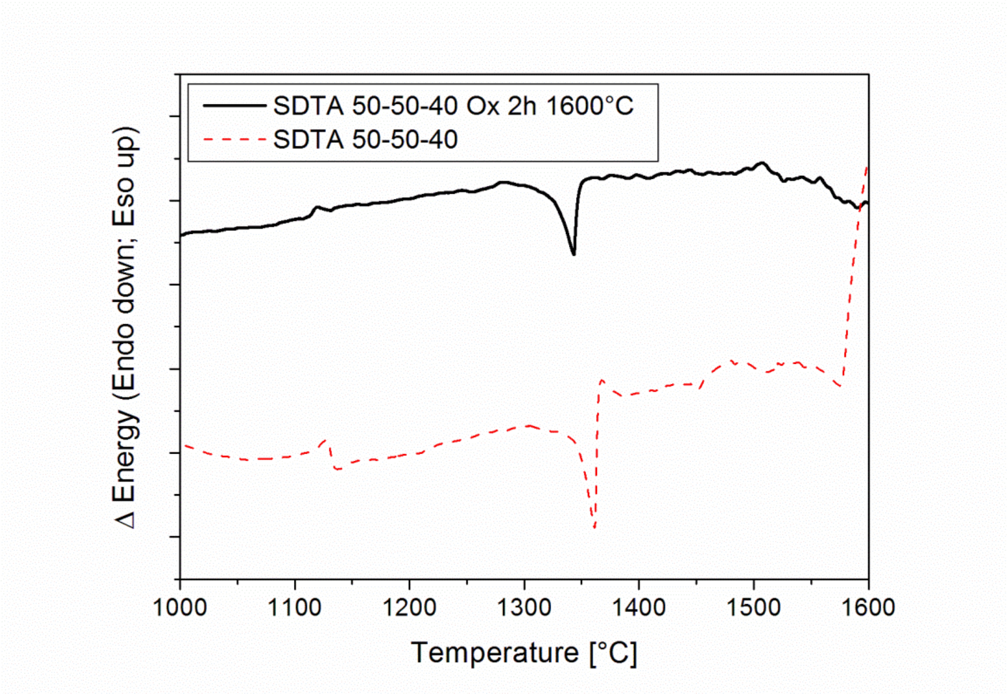

Figure 3.7: SDTA of the as-produced sample 50-50-40 during the first TGA in air and after 2h of oxidation at 1600°C.

3.3.4 Oxidation behavior after long-term oxidation at 1500°C

In this section, the nomenclature of the samples studied was changed and has been referred to them using the volume percentage fraction of zirconium diboride calculated after SRI (see Tabs. 3.IV and 3.V).

New sample labels	**ZrB_2 [vol.%]**	**Previous sample labels**
ZrB34	33.7	100-0-40
ZrB26	25.9	75-25-40
ZrB21	21.2	50-50-40
ZrB0	0.0	0-100-40

Table 3.V: New sample names for the long-term study.

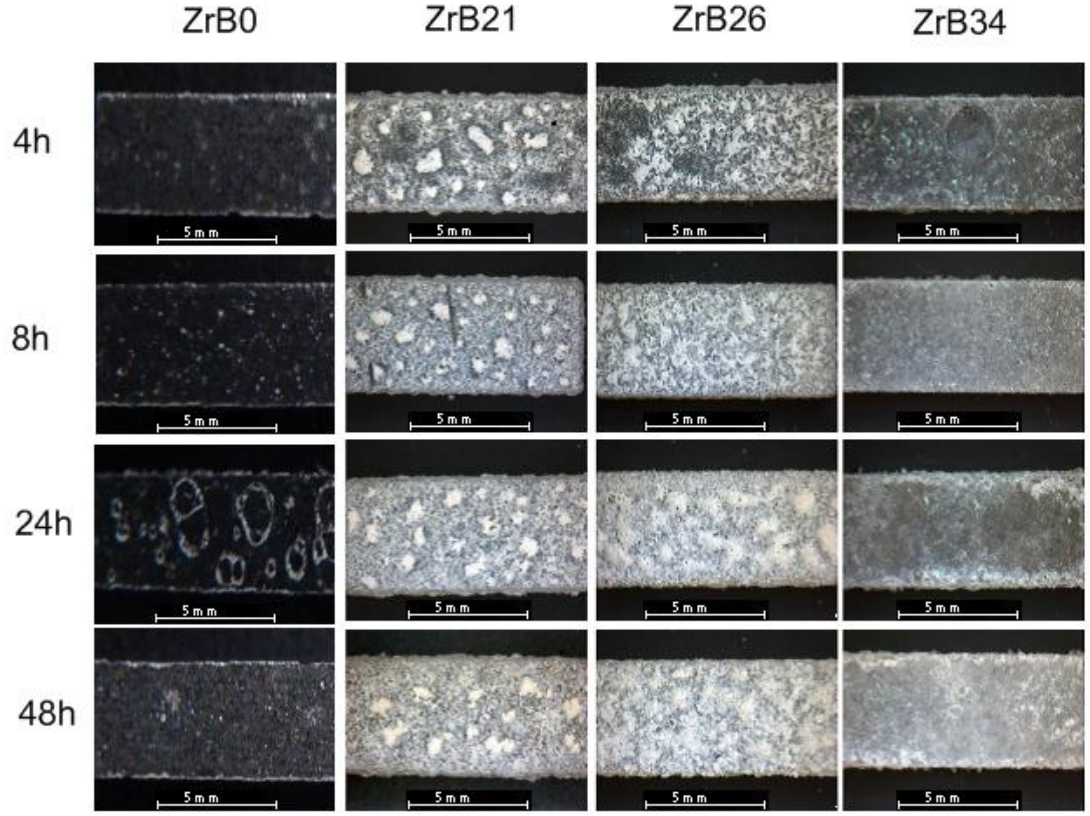

Figure 3.8: Overview of the samples' surface after oxidation treatments. The top labels indicate the sample compositions, the left labels refer to the dwelling oxidation time.

Figure 3.8 shows the surface of the samples oxidized in this study for different times. Even at low magnifications, the different oxidation behavior of the four samples is evident. On the ZrB21 surface, just after 4 oxidation hours, large ZrO_2 islands appear. The presence of zirconia dendrites adjacent to the ZrO_2 islands is an evidence that the secondary zirconia is precipitating from a saturated borosilicate (BSZ) liquid solution

[18]. Indeed boria and, to a lesser extent, silica can evaporate from the BSZ liquid on the external surface, changing the composition of the remaining liquid. Boron oxide is much more volatile, with a vapor pressure of 233 Pa at 1500°C [33]. The vapor pressure of silica is only $3*10^{-4}$ Pa at 1500°C [34]. On the surface, essentially all of the boria will evaporate. Depending on the temperature and atmosphere, some of the silica might also evaporate, but not zirconia. As boria evaporates, the remaining BSZ liquid becomes richer in silica, and zirconia must precipitate from the BSZ liquid. Thus the formation of secondary zirconia precipitates, located near the site of boria evaporation, is expected. The secondary zirconia will be precipitated from a liquid, and might have a different morphology from the primary zirconia, suggesting that it might be possible to distinguish secondary zirconia within the microstructure. The zirconia precipitates will either remain at the location where they formed, or be carried as a dispersed particle with the flowing BSZ liquid, increasing, most likely, its viscosity. It should be stressed, however, that it is also possible that some ZrO_2 grains form upon cooling, as the solubility of ZrO_2 in the borosilicate glass will decrease rapidly with temperature.

XRD patterns (Fig. 3.9) show several oxides present on the exposed surface, namely: zirconia (both monoclinic and tetragonal), silica (cristobalite, tridymite, quartz), zirconium silicate ($ZrSiO_4$) and three zirconium oxide (Zr_3O). These oxides are predicted by the state diagrams (Figs. 3.10, 3.11, 3.12) and were present already after 4 hours of oxidation. B_2O_3 was not detected due to its volatilization that starts above 1100°C. The main chemical reactions of oxidation that occur up to 1500°C in all Si-SiC-ZrB_2 systems (in addition to those already mentioned, see reactions from 3.1 to 3.4) are**:**

$$ZrO_2\ (cr) + SiO_2\ (s) \rightarrow ZrSiO_4\ (s) \qquad (3.6)$$

$$3\ ZrB_2\ (cr) + 5\ O_2\ (g) \rightarrow Zr_3O\ (cr) + 3B_2O_3\ (l) \qquad (3.7)$$

After 8h, for the ZrB21 sample, the amount of silica has increased and the amorphous phase has disappeared, furthermore the un-oxidized bulk material below the scale is undetectable by XRD. This indicates that SiC, Si and ZrB_2 are thoroughly oxidized during the exposure. The formation of crystalline SiO_2 is not well-understood but related to Si concentration in amorphous silica. The precipitation of crystalline SiO_2 from amorphous silica when Si concentration reached saturation is to be expected [35]. After ZrB_2 and SiC were oxidized, the ZrO_2 and amorphous silica coexisted in the silica-rich glass scale layer on the surface of samples. This results in a further reaction between ZrO_2 and amorphous silica, as shown in reaction (3.6). An early study [36] in ZrO_2 and amorphous silica showed that interstitial silicon diffuses and dissolves into crystalline ZrO_2 until the solution limit is reached when ZrO_2 and amorphous silica coexist, thereafter causing precipitation of $ZrSiO_4$. The formation of this phase, called zircon [21], has been reported by several authors [12, 21, 23, 24, 35, 37-40].

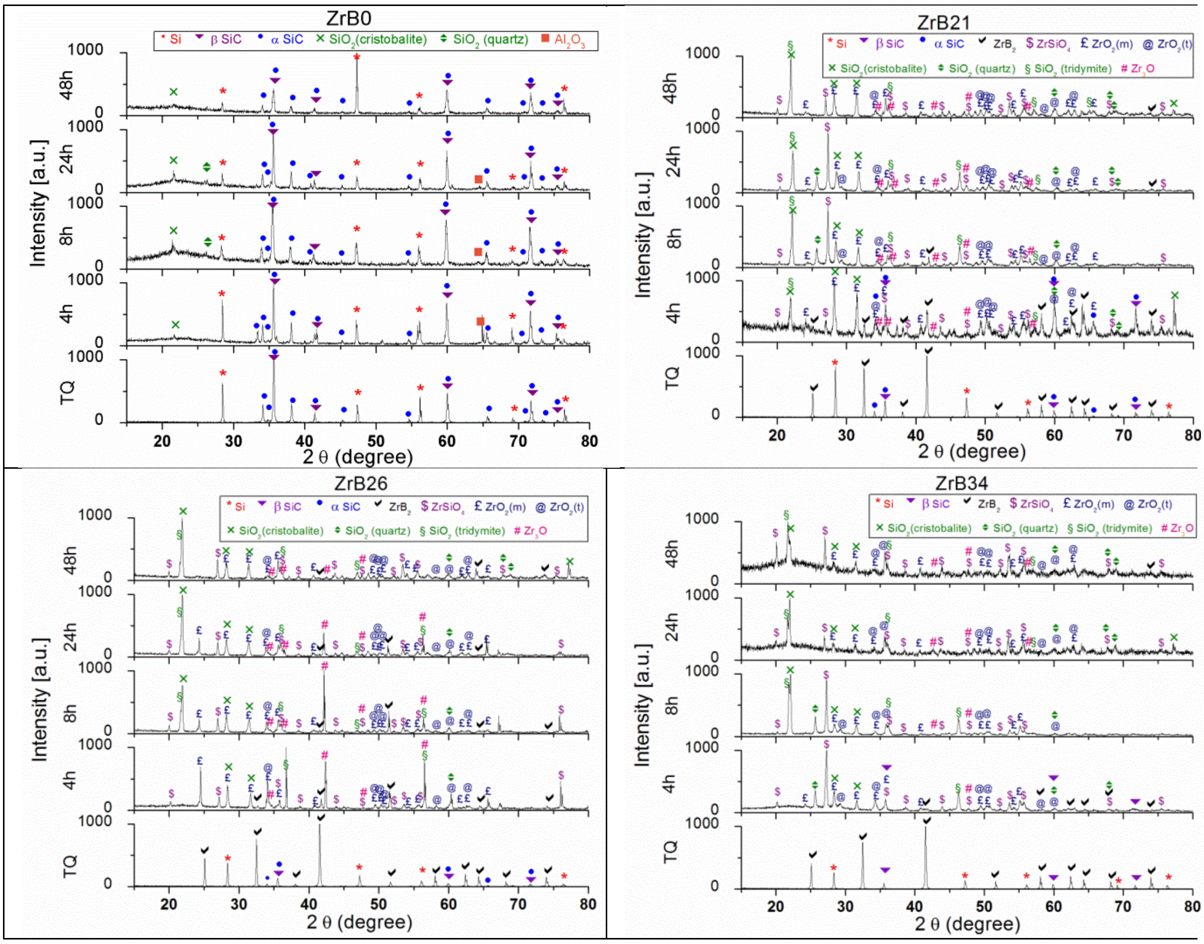

Figure 3.9: XRD sample patterns at 0h, 4h, 8h, 24h and 48h of oxidation at 1500°C.

With regard to ZrB34 the external oxide surface does not present the zirconia islands, but a smooth surface with bubbles and craters. The amorphous glassy phase is confirmed by the XRD, with a considerable increase starting from 24 hours of oxidation. Bubbles are caused by gasses development of the following species: CO and B_2O_3. SiO is not expected to form because it is based on the active oxidation of SiC (reaction 3.5). A passive to active transition of SiC oxidation occurs between 1873 K and 1973 K (1600°C and 1700°C) in air under atmospheric pressure [41, 42] so that, above these temperatures, any protection afforded by a glassy oxide layer is largely lost.

The presence of different polymorphic phases of silica and zirconia can be explained with equilibrium transformations that happen during cooling (reactions 3.8 and 3.9).

$$ZrO_2 \text{ (tetragonal)} \leftrightarrows ZrO_2 \text{ (monoclinic)} \qquad (3.8)$$

$$SiO_2 \text{ (cristobalite)} \leftrightarrows SiO_2 \text{ (tridymite)} \leftrightarrows SiO_2 \text{ (quartz)} \qquad (3.9)$$

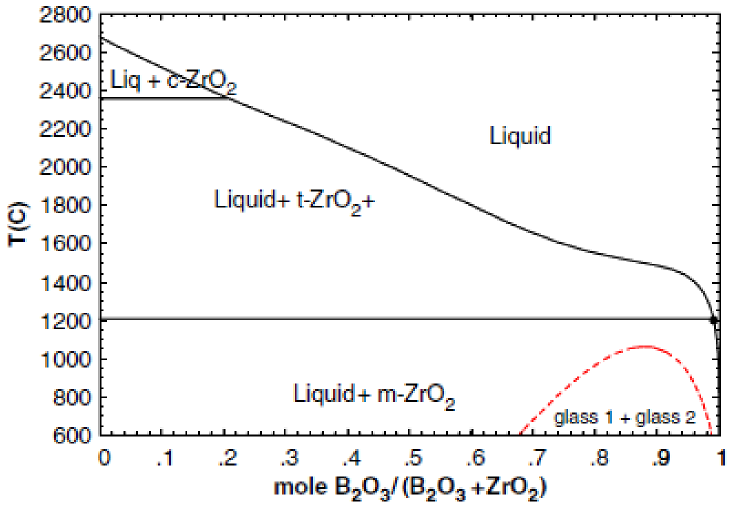

Figure 3.10: Calculated binary phase diagram for the system ZrO_2-B_2O_3, showing the solubility of zirconia in boron oxide liquid as a function of temperature [43].

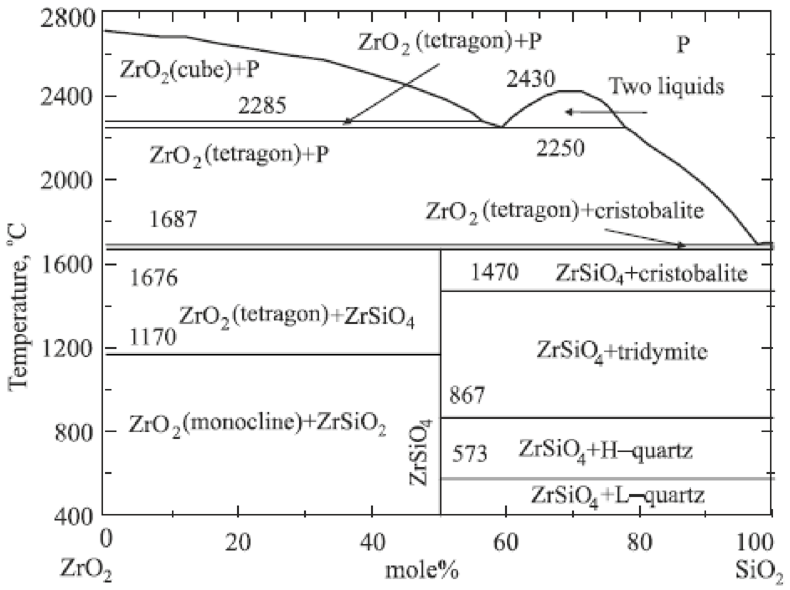

Figure 3.11: The ZrO_2-SiO_2 phase diagram [44].

The fields of stability of the different polymorphs are shown in their respective state diagrams (Figs. 3.10, 3.11, 3.12). The presence of phases of high temperature at RT is explained by the fact that these are metastable phases. In fact, the state diagrams refer to equilibrium situations; our case, on the other hand, due to the presence of impurities, is a metastable situation. Each one of these phases is characterized by its own structure and by a specific density. Three phases are known for ZrO_2: monoclinic < 1170°C, tetragonal 1170÷2370°C, and cubic > 2370°C, generally showing higher symmetry at higher temperatures. SiO_2, more than almost any material, exists in at least 14 crystalline forms [45], while the most known and stable at room temperature is quartz.

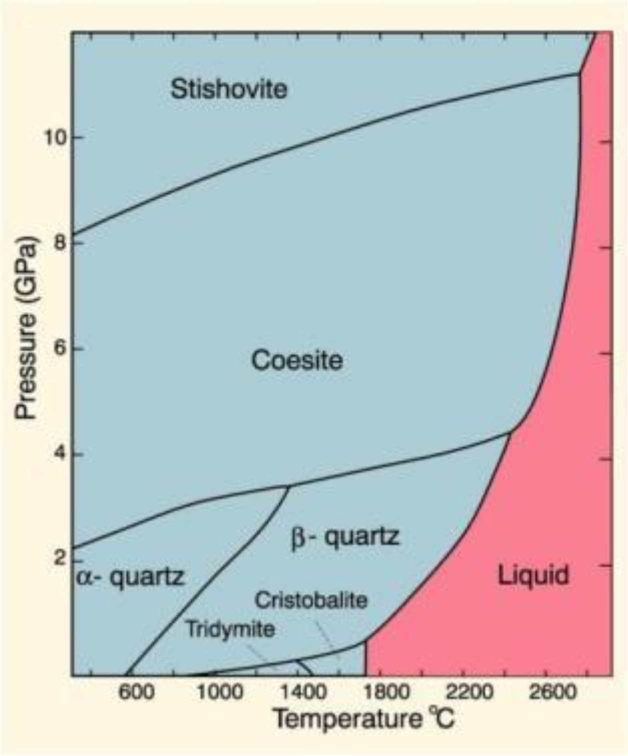

Figure 3.12: State diagram of silica.

The reference ZrB0 material (Fig. 3.9) showed a very different oxidation behavior. Even after 48 hours of thermal treatment the peaks related to the un-oxidized bulk are well defined and the only oxide crystalline phase is silica. SiO_2, initially present in both amorphous and crystalline phase, as oxidation continues, tends to become totally glassy. This behavior is also evident from the photos of the surface oxidized (first column in Fig. 3.8). Only after 24 hours of oxidation several craters left by the explosion of bubbles due to evaporation of CO can be seen, but after 48 hours these craters have visually disappeared and the surface is completely smooth and shiny. X-ray evidence is in good agreement with the weight gain measurements (Fig. 3.13). Figure 3.14, shows how the oxide layer for each composite increases with the increase of the dwelling time. The only exception is represented by the sample ZrB21 oxidized for 48h. This is due to the excessive thickness and weight of the scale that partially collapsed between 24 and 48h also owing to its porosity. The behaviors of ZrB26 and of ZrB34 are very similar. The thickness of each layer was measured by averaging several values at various locations. A large standard deviation in the oxide thicknesses was found due to the irregularity of the scales. After 24 hours of oxidation the thickness of the sample ZrB21 is about double compared to the ZrB26 and ZrB34 samples. It is worth noting that these high values can be achieved because the air in the furnace is stagnant. The different atmosphere and time conditions are also the reason why the sample ZrB21 showed a contrasting behavior compared to the TGA reported before (see Fig. 3.4). The overall trend of the graph in figure 3.14 is in good agreement with the values of specific weight gain shown in figure 3.13.

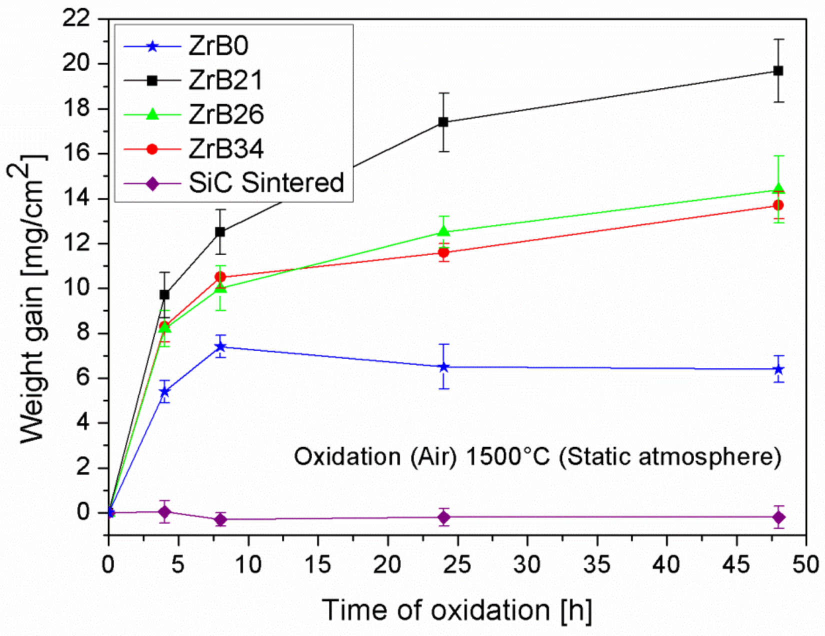

Figure 3.13: Normalized weight gain of the samples and reference materials for different oxidation times.

The oxidation rate of these Si-SiC-ZrB_2 materials, evaluated in terms of weight gain, is lower in comparison with ZrB_2-SiC systems [12, 19, 22, 23, 38], but higher than the values measured on sintered SiC. From figure 3.13 it is clear that even after 48 hours the process of oxidation is not terminated, in fact all the three Si-SiC-ZrB_2 samples continue to gain weight. A stable passivation oxide layer is achieved only for samples ZrB0 and sintered SiC. Moreover, the trend of the measured thicknesses of oxide on the sample ZrB0 appear much less high than the respective gains in weight, because in this sample, as can be seen from the elemental maps (Figs. 3.15, 3.16), the oxide layers are more compact, homogeneous and almost devoid of porosity. In the reference material, indeed, the thickness of the scale, even after 48 hours of treatment, does not exceed 30 microns. After 8 hours, however, a parabolic oxidation behavior is observed for each curve. This suggests that after the external glassy scale formed at the initial stage of oxidation, diffusion, more specifically the outward diffusion of constituent elements from the bulk material to the oxidized region and the inward diffusion of oxygen through the scale layer, is the rate controlling mechanism for oxidation, as observed for both ZrB_2-$MoSi_2$ and ZrB_2-SiC composites [9, 33, 46].

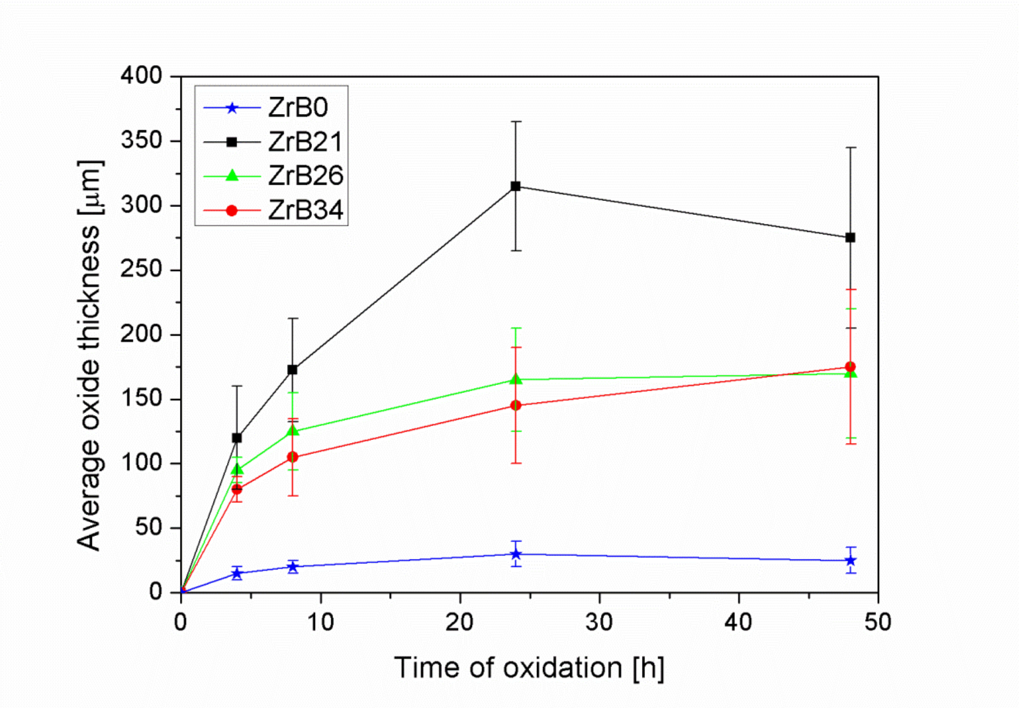

Figure 3.14: Average thickness of the oxide layer for different oxidation times.

Figures 3.15 and 3.16 report the FESEM images taken on the edge section for each specimen at different dwelling oxidation times. Every micrograph is matched with the corresponding elemental map of oxygen (green), silicon (red) and zirconium (white). Boron is difficult to characterize due to the low sensitivity of EDS to light elements. A first characteristic, common to all samples, is the change in feature of the oxide layer with increasing oxidation time. At the first stages, 4 and 8 hours, the scales appear compact and still rather well-fitting to the underneath bulk. After 24 and 48 hours, the scales are very porous and irregular; still well adherent to the un-oxidized substrate. The thickness of the BSZ layer and the underlying ZrO_2-containing layer are not uniform over the specimens surface at all temperatures. This may be due also to wetting characteristics or other local variations such as composition, surface topology or surface cracks that might enhance the local oxidation rate. Moreover, frequently the ZrO_2-containing layer is thicker in the areas where the silica-rich layer is thinner, indicating less effective oxidation protection in those regions. The boundary between the oxidized zone and the un-oxidized bulk can also be easily identified visually: the zirconia particles have jagged and irregular edges, while the particles of ZrB_2 are more regular and smooth.

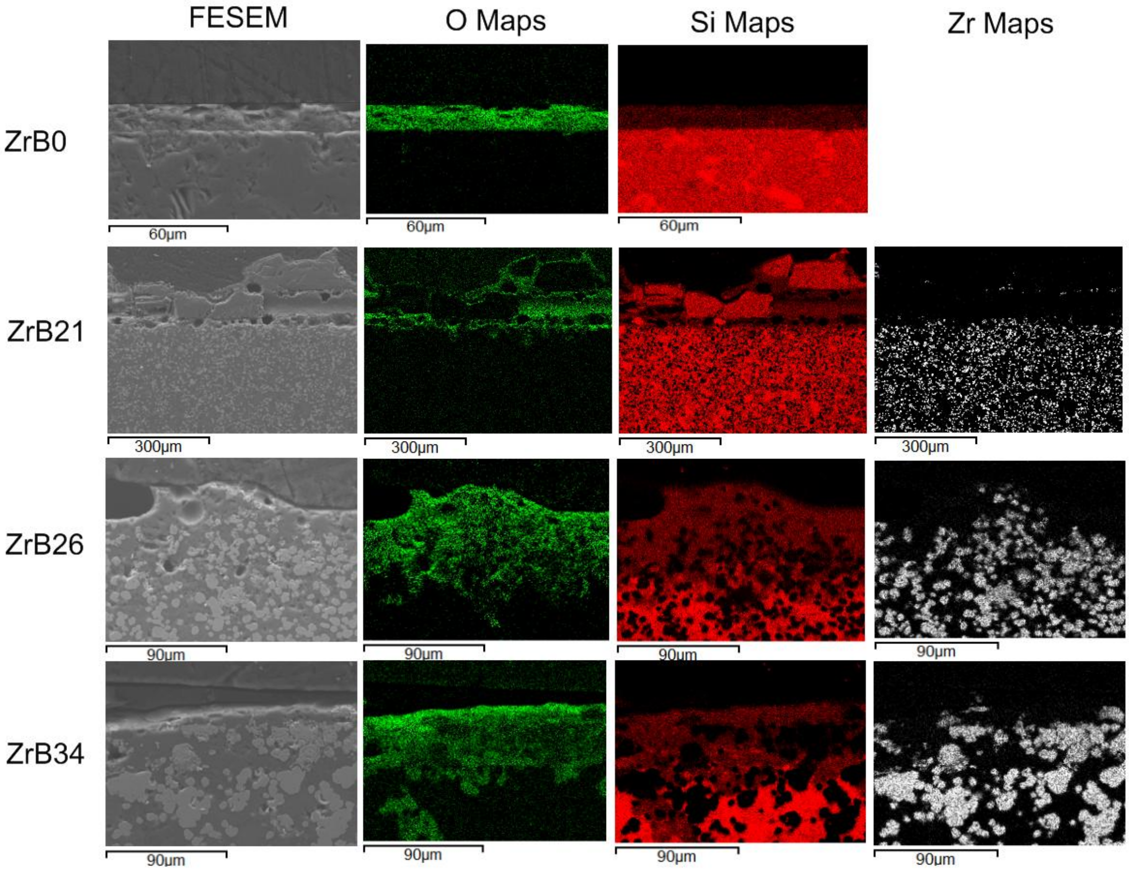

Figure 3.15: FESEM images and elemental maps of sample scales after 4h at 1500°C in air.

The high porosity can be explained not only with the volatilization of some phases. Volume changing can also produce porosity and cracks. Some cracks are observed around the nodules of zirconia (Fig. 3.8). This cracking behavior is associated either with different thermal expansion between ZrO_2 and SiO_2 or with the volumetric change accompanying transformations (3.8) and (3.9). The scales are mainly made of silica and particles of zirconia as deduced from the elemental maps. The silica phase is wrapped around the ZrO_2 particles. For the samples ZrB21 and ZrB26 the oxidation mechanism firstly proposed by Karlsdottir and Halloran seems to work [20]. They suggested a convection mechanism in which the driving force for borate flow is the very large volume increase upon oxidation of ZrB_2. The molar volume of the condensed oxides is different to the molar volume of the substrate. In the literature for oxidation of metals, the oxide/metal volume ratio is known as the Pillings–Bedworth Ratio (PBR). When the SiC is oxidized to silicon dioxide, the molar volume of SiC (12.47 cm^3/mole) is much smaller than the molar volume of SiO_2 (27.43 cm^3/mole). The carbon oxidizes to CO gas. The ratio of the molar volume of silica to the molar volume of SiC is the PBR of SiO_2, which is 2.2. For ZrB_2, we can define partial PBRs for B and for Zr, and a total PBR, using the molar volumes of ZrB_2 (18.54 cm^3/mole), B_2O_3 (55.2 cm^3/ mole) and ZrO_2 (20.92 cm^3/mole) [47]. The B partial PBR_B is 2.98, forming a liquid that can flow. The zirconium partial PBR_Z is 1.13, with the zirconium oxide being a rigid solid. Due to the large increase in volume, it follows that the liquid oxide must be squeezed out onto the surface. It is likely that the volume increase upon oxidation is the driving force for liquid flow. A schematic sketch of the proposed mechanism is shown in Fig. 3.17 [2]. The main differences between this model and our samples are represented by the lack of boron fingering on the surface and by the absence of the porous ZrO_2 layer under the external layer. The absence of boron oxide on the surface is justifiable given the long oxidation times at 1500°C which cause the complete evaporation. The second aspect, the absence of the columnar structure of zirconia, is confirmed in other works, in which it is demonstrated that it is formed only with percentages of ZrB_2 above 50% [7, 9, 11, 48] as in the study of Karlsdottir and Halloran [20, 21]. From the elemental maps of ZrB34, this sample seems not to follow the convection cells model, indeed no zirconia particles can be detected in the scale. This behavior is in good agreement with what can be visually observed on the surface (Fig. 3.8). XRD patterns (Fig. 3.9) show how zirconia and zircon are present on the external oxide layer of this sample, but the intensity of the related peaks is lower. The lower intensity of the peaks relating to the zirconia, may accordingly be explained by the presence of many small crystallites not appreciable at low magnifications. It is therefore possible to hypothesize that this mechanism also takes place in this type of sample, but to a lesser extent.

In all micrographs the SiC depletion layer in agreement with what was previously pointed out by Williams et al. [11] is not observed. In this study it was found that, for isothermal exposure, the SiC-depleted layer can be reduced by increasing the volume fraction of SiC, and is undetectable in composites with at least vol.% SiC > 50 vol.%.

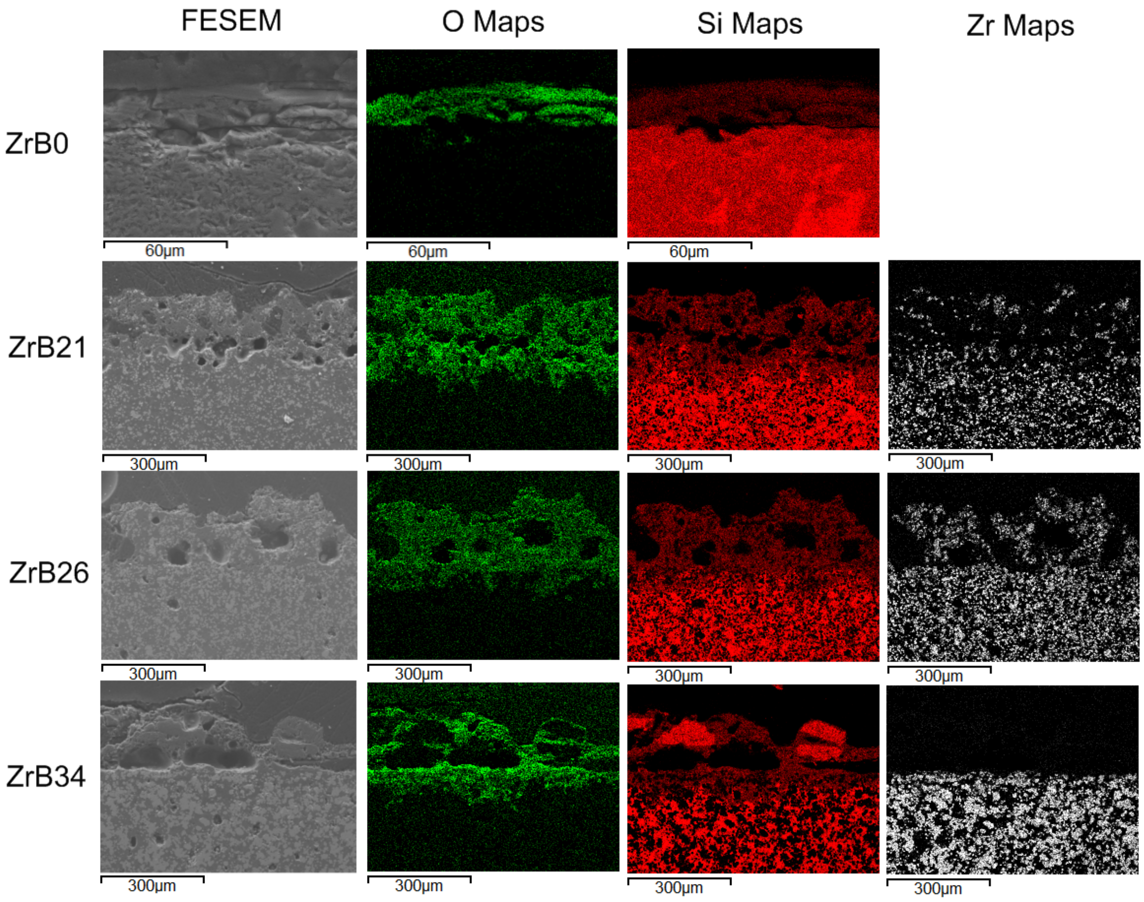

Figure 3.16: FESEM images and elemental maps of sample scales after 48h at 1500°C in air.

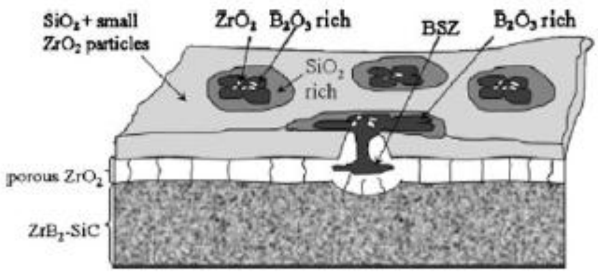

Figure 3.17: Schematic of convection cell features on the surface of oxidized ZrB_2-SiC UHTCs. BSZ is a liquid oxide solution containing boria, silica and zirconia [21].

The strength of non-oxide ceramics is affected by many factors [49, 50]. In our study, to better drive high-temperature engineering applications of non-oxide ceramics, an understanding of the effects of oxidation on the room-temperature flexural strength of the material is essential. Considerable studies have reported strength retention for SiC and Si_3N_4 ceramics after oxidation [51, 52], but only limited experimental work involves strength retention of ZrB_2-based ceramics after oxidation [53, 54]. Oxidation influenced the strength of Si-SiC-ZrB_2 ceramics (Fig. 3.18). As oxidation times progressed, the retained flexural strength of the samples with ZrB_2 had similar trends that gradually decreased. Nevertheless, the strengths after 48 hours of oxidation were between seventy and ninety percent compared to the un-oxidized samples. The same trend can be observed in the sample ZrB0, albeit with slightly lower values, but consistent with literature data [55, 56] due to the higher content of free silicon. Eventually, the flexural strength of the ZrB_2-based ceramics was significantly increased by adding second phase particles. It must be underlined, however, how the dispersion in this kind of measurements is very high. By way of sample, the fractured surfaces of sample ZrB26 failed at room temperature, after 48 hours of oxidation at 1500°C, are shown in Fig. 3.19. The fracture mode, owing to the lack of cleavage facets, smooth and planar, and to the presence of holes due to the pullout of particles, is intergranular failure in the inner area of the sample (Fig. 3.19, left); the fracture surface of the oxide, however, appears smooth and flat (Fig. 3.19, right). Other works have reported an increase in strength after oxidation for silicon based ceramics such as SiC and Si_3N_4 [51, 52] but for lower temperatures and lower times of oxidation. This increase has been attributed to the formation of a thin, dense oxide layer that could heal the surface flaws resulting from sample processing and machining. Surface flaw healing was effective only when the oxide layer was dense, very thin and well adherent to the bulk. When the oxide layer became thicker and porous, the flaw healing effect was counterbalanced by the generation of new defects, either within the oxide scale or at the interface between the oxide scale and bulk materials. Guo [50] noted how the first behavior is typical of the nano-sized SiC-ZrB_2 composites, while the second one is characteristic of micron-sized SiC-ZrB_2 composites, as in our case.

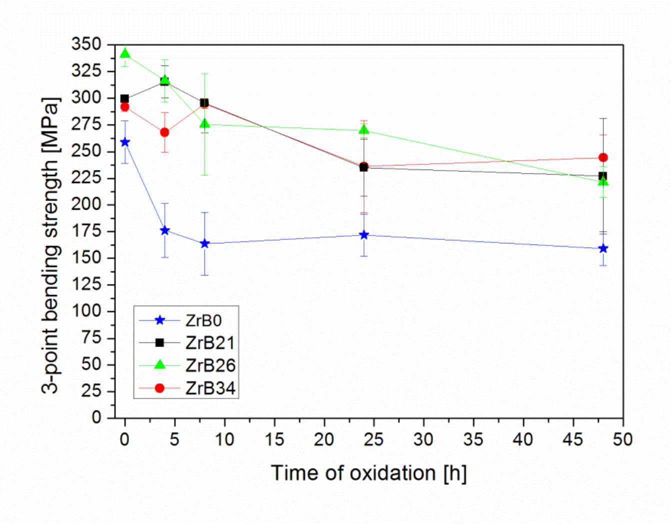

Figure 3.18: Flexural strength of the samples at different oxidation times.

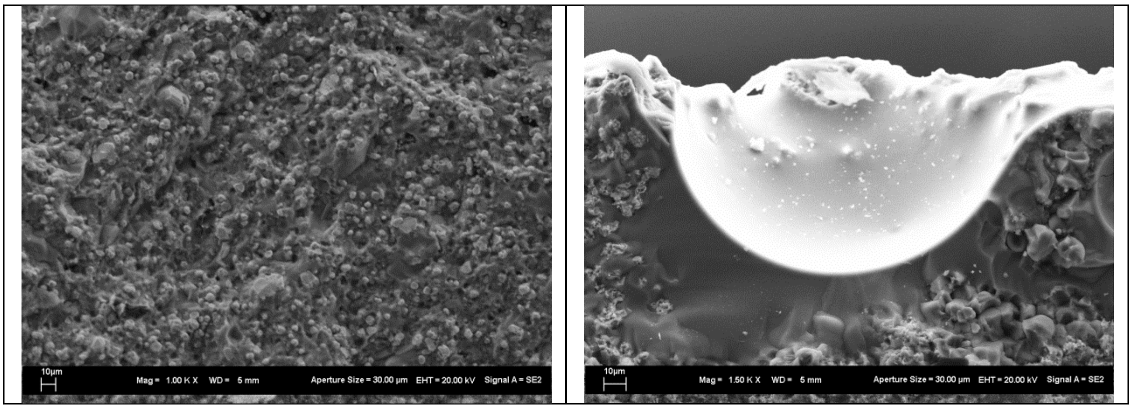

Figure 3.19: Fractured surface of sample ZrB26 after 48h of oxidation at 1500°C in air; left: inner zone; right: oxide scale (outer zone).

3.4 Conclusions

This study demonstrates that it is possible to obtain fully dense Si-SiC-ZrB_2 composite bulks produced via silicon reactive infiltration. A detailed explanation of all the stages of oxidation with the different reactions and phase transformations that occur at varying temperatures has been given in this work with the aim of interpreting the final microstructure in the oxidized samples. The oxidation behavior observed proved to be very similar to that of the silicon carbide obtained via SRI. In agreement with the previous chapter and other recent publications [11], a SiC-depleted layer was not observed.

Si-SiC-ZrB_2 system after short-term oxidation presented a three layer structure:

a) Silica;
b) BSZ with ZrO_2 particles;
c) un-oxidized bulk material.

Another important point to stress is how the TGA measurements showed clearly that this scale effectively passivates these materials already after a few minutes of oxidation.

The content of phenolic resin seems not to affect the oxidation behavior of the composites. With regard to long-term oxidation already after 4 oxidation hours all the samples with ZrB_2 showed passivating oxidation layer, notwithstanding, as is evident from the specific weight gain, even after 48 hours the oxidation process was not finished. Several oxides were detected on the surface: zirconia (monoclinic and tetragonal), silica (cristobalite, tridymite, quartz), zircon ($ZrSiO_4$) and three zirconium oxide (Zr_3O). Boria was not detected. The starting combination of powders without α-SiC, among those that contain

ZrB_2, seemed to offer the best long-term oxidation behavior. By the authors' judgement, this study lends support to the oxidation model proposed by Karlsdottir and Halloran [20, 21]: the so called “convection cells mechanism” in which the volume increase upon oxidation is the driving force for BSZ liquid to squeeze out onto the surface. Regarding mechanical tests, oxidation influenced the strength of Si-SiC-ZrB_2 ceramics. All the samples provide the same tendency of keeping from 70% to 90% of the original flexural strength.

3.5 References

[1] N. S. Jacobson, *Corrosion of Silicon-Based Ceramics in Combustion Environments*, J. Am. Ceram. Soc., 76 [1] 13-28 (1993).

[2] E. Eakins, D. D. Jayaseelan and W. E. Lee, *Toward Oxidation-Resistant ZrB_2-SiC Ultra High Temperature Ceramics*, Metall. and Mater. Trans. A, 42 [4] 878-87 (2011).

[3] J. K. Sonber and A. K. Suri, *Synthesis and Consolidation of Zirconium Diboride: Review*, Adv. Appl. Ceram., 110 [6] 321-34 (2011).

[4] L. Stobierski and A. Gubernat, *Sintering of Silicon Carbide: I. Effect of Carbon; II. Effect of Boron*, Ceram. Int., 29 [3-4] 287-92 355-61 (2003).

[5] J. A. Costello, R. E. Tressler and I. S. T. Tsong, *Boron Redistribution in Sintered α-SiC during Thermal-Oxidation*, J. Am. Ceram. Soc., 64 [6] 332-5 (1981).

[6] W. B. Hillig, R. L. Mehan, C. R. Morelock, V. J. Decarlo and W. Laskow, *Silicon-Silicon Carbide Composites*, Am. Ceram. Soc. Bull., 54 [12] 1054-6 (1975).

[7] W. G. Fahrenholtz and G. E. Hilmas, *Oxidation of Ultra-High Temperature Transition Metal Diboride Ceramics*, Int. Mater. Rev., 57 [1] 61-72 (2012).

[8] E. V. Clougher, R. L. Pober and L. Kaufman, *Synthesis of Oxidation Resistant Metal Diboride Composites*, T Metall. Soc. Aime., 242 [6]1077-82 (1968).

[9] A. Rezaie, W. G. Fahrenholtz and G. E. Hilmas, *Evolution of Structure during the Oxidation of Zirconium Diboride-Silicon Carbide in Air Up to 1500°C*, J. Eur. Ceram. Soc., 27 [6] 2495-501 (2007).

[10] E. J. Opila and M. C. Halbig, *Oxidation of ZrB_2-SiC*, Ceram. Eng. Sci. Proc., 22 [3] 221-8 (2001).

[11] P. A. Williams, R. Sakidja, J. H. Perepezko and P. Ritt, *Oxidation of ZrB_2-SiC Ultra-High Temperature Composites Over a Wide Range of SiC Content*, J. Eur. Ceram. Soc., 32 [14] 3875-83 (2012).

[12] I. B. Ban'kovskaya and V. A. Zhabrev, *Kinetic Analysis of the Heat Resistance of ZrB_2-SiC Composites*, Glass Phys. and Chem., 31 [4] 482-8 (2005).

[13] A. Ortona, P. Fino, C. D'Angelo, S. Biamino, G. D'Amico, D. Gaia and S. Gianella, *Si-SiC-ZrB_2 Ceramics by Silicon Reactive Infiltration*, Ceram. Int., 38 [4] 3243-50 (2012).

[14] Y. D. Blum, J. Marschall, D. Hui and S. Young, *Thick Protective UHTC Coatings for SiC-Based Structures: Process Establishment*, J. Am. Ceram. Soc., 91 [5] 1453-60 (2008).

[15] H. J. Zhou, L. Gao, Z. Wang and S. M. Dong, *ZrB_2-SiC Oxidation Protective Coating on C/C Composites Prepared by Vapor Silicon Infiltration Process*, J. Am. Ceram. Soc., 93 [4] 915-9 (2010).

[16] S. Biamino, V. Liedtke, C. Badini, G. Euchberger, I. H. Olivares, M. Pavese and P. Fino, *Multilayer SiC for Thermal Protection System of Space Vehicles: Manufacturing and Testing Under Simulated Re-Entry Conditions*, J Eur Ceram Soc., 28 [14] 2791-800 (2008).

[17] C. M. V. Bolivar, A. Antonini, S. Biamino, M. Pavese, P. Fino and C. Badini, *Oxidation resistance of Multilayer SiC for Space Vehicle Thermal Protection Systems*, Adv. Eng. Mater., 12 [7] 617-22 (2010).

[18] S. N. Karlsdottir and J. W. Halloran, *Oxidation of ZrB_2-SiC: Influence of SiC Content on Solid and Liquid Oxide Phase Formation*, J. Am. Ceram. Soc., 92 [2] 481-6 (2009).

[19] M. M. Opeka, I. G. Talmy, E. J. Wuchina, J. A. Zaykoski and S. J. Causey, *Mechanical, Thermal and Oxidation Properties of Refractory Hafnium and Zirconium Compounds*, J. Eur. Ceram. Soc., 19 [13-14] 2405-14 (1999).

[20] S. N. Karlsdottir and J. W. Halloran, *Convection Patterns in Liquid Oxide Films on ZrB_2-SiC Composites Oxidized at a High Temperature*, J. Am. Ceram. Soc., 90 [9] 2863-7 (2007).

[21] S. N. Karlsdottir and J. W. Halloran, *Zirconia Transport by Liquid Convection during Oxidation of Zirconium Diboride-Silicon Carbide*, J. Am. Ceram. Soc., 91 [1] 272-7 (2008).

[22] W.M. Guo and G.-J. Zhang, *Oxidation Resistance and Strength Retention of ZrB_2-SiC Ceramics*, J. Eur. Ceram. Soc., 30 [11] 2387-95 (2010).

[23] I. B. Ban'kovskaya and D. V. Kolovertnov, *Effect of the Thermal Treatment Mode on the Composition and Structure of ZrB_2-SiC System Composites*, Glass Phys. and Chem., 39 [5] 579-88 (2013).

[24] F. Tao, L. He-Jun, S. Xiao-Hong, Y. Xi and W. Shao-Long, *Oxidation and Ablation Resistance of ZrB_2-SiC-Si/B-Modified SiC Coating for Carbon/Carbon Composites*, Corros. Sci., 67 292-7 (2013).

[25] M.W. Chase Jr., *NIST-JANAF Thermochemical Tables*, 4th edition, J. Phys. Chem. Ref. Data, 1-1951 (Monograph 9) (1998).

[26] J. G. Li and H. Hausner, *Reactive Wetting in the Liquid-Silicon/Solid-Carbon System*, J. Am. Ceram. Soc., 79 [4] 873-80 (1996).

[27] O. Dezellus, S. Jacques, F. Hodaj and N. Eustathopoulos, *Wetting and Infiltration of Carbon by Liquid Silicon*, J. Mater. Sci., 40 [9-10] 2307-11 (2005).

[28] C. E. Ramberg and W. L. Worrell, *Oxygen Transport in Silica at High Temperatures: Implications of Oxidation Kinetics*, J. Am. Ceram. Soc., 84 [11] 2607-16 (2001).

[29] C. Wagner, *Passivity during the Oxidation of Silicon at Elevated Temperatures,* J. Appl. Phys., 29 [9] 1295-97 (1958).

[30] E. A. Gulbrasen and S. A. Jansson, *The High-Temperature Oxidation, Reduction and Volatilization Reactions of Silicon and Silicon Carbide*, Oxid. Met., 4 [3] 181-201 (1972).

[31] S. Gangireddy, S. N. Karlsdottir, S. J. Norton, J. C. Tucker and J. W. Halloran, *In Situ Microscopy Observation of Liquid Flow, Zirconia Growth, and CO Bubble Formation during High Temperature Oxidation of Zirconium Diboride-Silicon Carbide*, J. Eur. Ceram. Soc., 30 [11] 2365-74 (2010).

[32] T. A. Parthasarathy, R. A. Rapp, M. Opeka and M. K. Cinibulk, *Modeling Oxidation Kinetics of SiC-Containing Refractory Diborides*, J. Am. Ceram. Soc., 95 [1] 338-49 (2012).

[33] W. G. Fahrenholtz, *Thermodynamic Analysis of ZrB_2-SiC Oxidation: Formation of a SiC-Depleted Region*, J. Am. Ceram. Soc., 90 [1] 143-8 (2007).

[34] W. G. Fahrenholtz, *The ZrB_2 Volatility Diagram*, J. Am. Ceram. Soc., 88 [12] 3509-12 (2005).

[35] S.-Q. Guo, T. Mizuguchi, M. Ikegami and Y. Kagawa, *Oxidation Behavior of ZrB_2-$MoSi_2$-SiC Composites in Air at 1500°C*, Ceram. Int., 37 [2] 585-91 (2011).

[36] C. Veytizou, J. F. Quinson, O. Valfort and G. Thomas, *Zircon Formation From Amorphous Silica and Tetragonal Zirconia: Kinetic Study and Modeling*, Solid State Ionics, 139 [3-4] 315-23 (2001).

[37] C. R. Wang, J.-M. Yang and W. Hoffman, *Thermal Stability of Refractory Carbide/Boride Composites*, Mat. Chem. and Phys., 74 [3] 272-81 (2002).

[38] M. Mallik, K. K. Ray and R. Mitra, *Oxidation Behavior of Hot Pressed ZrB_2-SiC and HfB_2-SiC Composites*, J. Eur. Ceram. Soc., 31 [1-2] 199-215 (2011).

[39] V. O. Lavrenko, A. D. Panasyuk, O. M. Grigorev, O. V. Koroteev and V. A. Kotenko, *High Temperature Oxidation of ZrB_2-SiC and ZrB_2-SiC-$ZrSi_2$ Ceramics Up to 1700°C in Air*, Powder Metall. and Met. Ceram., 51 [3-4] 217-21 (2012).

[40] Y. Wang, L. Luo, J. Sun and L. An, *ZrB_2-SiC(Al) Ceramics with High Resistance to Oxidation at 1500°C*, Corrosion Science, 74 154-8 (2013).

[41] J. Wang, L. Zhang, Q. Zeng, G. L. Vignoles and A. Guette, *Theoretical Investigation for the Active-to-Passive Transition in the Oxidation of Silicon Carbide,* J. Am. Ceram. Soc., 91 [5] 1665-73 (2008).

[42] M. J. Balat, *Determination of the Active-to-Passive Transition in the Oxidation of Silicon Carbide in Standard and Microwave-Excited Air*, J. Eur. Ceram. Soc., 16 [1] 55-62 (1996).

[43] W. C. Beard, *Research on Phase Equilibria between Boron Oxides and Refractory Oxides, Including Silicon and Aluminum Oxides*, Quarterly Progress Report [9], (1961), Technical Report, Ohio State University Research Foundation, Columbus, OH, (1962).

[44] A. S. Berezhnoi, *Multicomponent Oxide Systems*, Naukova Dumka, 216 (1970).

[45] A. F. Holleman and E. Wiberg, *Inorganic Chemistry*, San Diego: Academic Press, ISBN 0-12-352651-5 (2001).

[46] D. Sciti, M. Brach and A. Bellosi, *Oxidation Behavior of a Pressureless Sintered ZrB_2-$MoSi_2$ Ceramic Composite*, J. Mater. Res., 20 [4] 922-30 (2005).

[47] S. Fujino, C. Hwang and K. Morinaga, *Density, Surface Tension, and Viscosity of PbO-B_2O_3-SiO_2 Glass Melts*, J. Am. Ceram. Soc., 87 [1] 10-6 (2004).

[48] S. R. Levine, E. J. Opila, M. C. Halbig, J. D. Kiser, M. Singh and J. A. Salem, *Evaluation of Ultra-High Temperature Ceramics for Aeropropulsion Use*, J. Am. Ceram. Soc., 22 [14-15] 2757-67 (2002).

[49] S. C. Zhang, G. E. Hilmas and W. G. Fahrenholtz, *Mechanical Properties of Sintered ZrB_2-SiC Ceramics*, J. Eur. Ceram. Soc., 31 [5] 893-901 (2011).

[50] S.-Q. Guo, *Densification of ZrB_2-Based Composites and their Mechanical and Physical Properties: A Review*, J. Eur. Ceram. Soc., 29 [6] 905-1011 (2009).

[51] H.-W. Kim, H.-E. Kim, H. Song and J. Ha, *Effect of Oxidation on the Room Temperature Flexural Strength of Reaction-Bonded Silicon Carbides*, J. Am. Ceram. Soc., 82 [6] 1601-4 (1999).

[52] H. Park, H.-W. Kim and H.-E. Kim, *Oxidation and Strength Retention of Monolithic Si_3N_4 and Nanocomposite Si_3N_4-SiC with Yb_2O_3 as a Sintering Aid*, J. Am. Ceram. Soc., 81 [8] 2130-4 (1998).

[53] D. Sciti, M. Brach and A. Bellosi, *Long-Term Oxidation Behavior and Mechanical Strength Degradation of a Pressurelessly Sintered ZrB_2-$MoSi_2$ Ceramic,* Scripta Mater., 53 [11] 1297-302 (2005).

[54] S.-Q. Guo, J.-M. Yang, H. Tanaka and Y. Kagawa, *Effect of Thermal Exposure on Strength of ZrB_2-Based Composites with Nano-Sized SiC Particles*, Compos. Sci. Technol., 68 [14] 3033-40 (2008).

[55] Q. W. Huang and L. H. Zhu, *High-Temperature Strength and Toughness Behaviours for Reaction-Bonded SiC Ceramics Below 1400°C,* Mater. Lett., 59 [14-15] 1732-5 (2005).

[56] http://www.schunk-sik.com/en/schunk01.c.9111.de/all_productarticle.